Numerical Solution of Multiscale Electromagnetic Systems

by

Luis Eduardo Tobón Llano

Department of Electrical and Computer Engineering
Duke University

Date: _____

Approved:

_____
Qing Huo Liu, Supervisor

_____
John Trangenstein

_____
William Joines

_____
Gary A. Ybarra

_____
Jian-Guo Liu

Dissertation submitted in partial fulfillment of the requirements for the degree of Doctor of Philosophy in the Department of Electrical and Computer Engineering in the Graduate School of Duke University
2013

Abstract

Numerical Solution of Multiscale Electromagnetic Systems

by

Luis Eduardo Tobón Llano

Department of Electrical and Computer Engineering
Duke University

Date: _____

Approved:

_____
Qing Huo Liu, Supervisor

_____
John Trangenstein

_____
William Joines

_____
Gary A. Ybarra

_____
Jian-Guo Liu

An abstract of a dissertation submitted in partial fulfillment of the requirements for the degree of Doctor of Philosophy in the Department of Electrical and Computer Engineering
in the Graduate School of Duke University
2013

Abstract

The Discontinuous Galerkin time domain (DGTD) method is promising in modeling of realistic multiscale electromagnetic systems. This method defines the basic concept for implementing the communication between multiple domains with different scales. Constructing a DGTD system consists of several careful choices: (a) governing equations; (b) element shape and corresponding basis functions for the spatial discretization of each subdomain; (c) numerical fluxes onto interfaces to bond all subdomains together; and (d) time stepping scheme based on properties of a discretized system. This work presents the advances in each one of these steps.

About the governing equations, a unified framework based on the theory of differential forms and the finite element method is used to analyze the discretization of the Maxwell's equations. Based on this study, field intensities ($\mathbf{E}$ and $\mathbf{H}$) are associated to curl-conforming basis functions (1-forms in differential forms); flux densities ($\mathbf{D}$ and $\mathbf{B}$) are associated to divergence-conforming basis functions (2-forms); and the constitutive relations are defined by Hodge operators, an operator that transforms 1-forms into 2-forms, or vice versa.

A different approach of analyzing the discretization of Maxwell's equations is the study of numerical dispersion. Semidiscrete analysis is the traditional method, but for high order elements modal analysis is prefered. From these analyses, we conclude that a correct discretization of fields belonging to different p-form (e.g., $\mathbf{E}$ and $\mathbf{B}$) uses basis functions with same order of interpolation; however, different order

of interpolation must be used if two fields belong to the same p-form (e.g., **E** and **H**). An alternative method to evaluate numerical dispersion based on evaluation of dispersive Hodge operators is also presented. Both dispersion analyses are equivalent and reveal same fundamental results. Eigenvalues, eigenvector and transient results are studied to verify accuracy and computational costs of different schemes.

Two different approaches are used for implementing the DG Method. The first is based on **E** and **H** fields, and use curl-conforming basis functions for both fields with different order of interpolation. In this case, the Riemman solver shows the best performance to treat interfaces between subdomains. A new spectral prismatic element, useful for modeling of layer structures, is implemented for this approach. With this element, in addition to tetrahedral and hexahedral elements, the DGTD method has a full set of element shapes and basis functions. Furthermore, for the EH-DGTD method, a new efficient and very accurate time integration method for sequential subdomains is implemented.

The second approach for solving multidomain cases is based on **E** and **B** fields, which use curl- and divergence-conforming basis functions, respectively, with same order of interpolation. In this way, higher accuracy and lower memory consumption are obtained with respect to the first approach based on **E** and **H** fields. The centered flux is used to treat interfaces with non-conforming meshes, and both explicit Runge-Kutta method and implicit Crank-Nicholson method are implemented for time integration.

Numerical examples and realistic cases are presented to verify that the proposed methods are non-spurious and efficient DGTD schemes.

This dissertation is dedicated to Paula, Maria José and Jerónimo who are my soul and life.

Contents

List of Tables

List of Figures

Acknowledgements

I would like to express my deep gratitude to Professor Qing Huo Liu, for his patient guidance, enthusiastic encouragement and useful critiques of this research work. I would also like to thank Dr. Jiefu Chen, for his advice and kindness during the first three years of my studies. I am very grateful to Professors William T. Joines, John A. Trangenstein, Jian-Guo Liu, and Gary Ybarra for being my committee members and giving me constructive suggestions.

My special thanks are extended to the staff of Wave Computation Technology, inc., Dr. Jun Ho Lee, Dr. Yuan Mengqing, Dr. Bo Zhao and Ms. Tong Li, great summer of 2012; my thanks also to Dr. Mei Chai and Dr. Jason Mix, from Intel Co., and Dr. Mohsen Ahmadian and Professor Pabitra Sen, from the Advanced Energy Consortium.

I wish to acknowledge the help provided by LASPAU and Fulbright-Colombia, specially to Ms. Lisa Tapiero, and Ms. Sylvia Castrillon, my advisors in these institutions. I would also like to acknowledge the support given by COLCIENCIAS during the first three years of my studies.

I am particular grateful to a lot of people in la Pontificia Universidad Javeriana - Cali: Priest Jorge Peláez S.J., Dr. Julian Garcés, Professors Jorge Estela, Mauricio Jaramillo, Camilo Rueda, Gloria Alvarez, Fabio Almanzar, Ana Prados, and many more, who provide all the support to accomplish this project.

I would like to offer my special thanks to all my friends in Professor Liu's group,

specially to Qiang Ren, Tengmeng Tan, Na Liu, Ma Luo, Yu Jia, Jun Niu, Qingtao Sun, Lin Wang, Yu Zhiru, Dr. Zhang Wenji, Junwen Dai, Yuchuan Jian, Cong Wu, and many more.

Special thanks should be given to my friends in Durham, the best family a PhD student can have: Pablo, Wendy, Eduardo, Felipe, Joes, Luz, Nata, Francisco, Gabo, Alejo, Mariano, Diego, Sam, Emily, Sylvain, Melina, Sandra, Ricardo, Marco, Andrea V., Ryan, German, Andrea C., Carla, Miguel, Carlos; Pa'las Que Sea for ever.

And now, last but not least, the most special thanks for my family. First, thanks to my parents and grandparents; they provided me with a strong, deep and free soul, thank you. And finally, Paula, Maria José and Jerónimo; you are my everything, the beginning and the end of my life; you are my motivation and my goal. Thanks for being.

1

Introduction

Are we facing the end of the Moore's law? This question has been asked since the inception of the prediction given by Gordon Moore in 1965, but every year the semiconductor industry found ways to keep going. Today, the main problem is related with the least known, and least enthusiastic, Moore's second law. According with this law, the cost of production double every four years, thus if it is hard to keep the exponential rate of transistor density, it is even harder if the cost of production is growing in a similar pace (Sperling, 2013). Semiconductor manufacturers need a new paradigm in electronic production, and the most promising option is going into the third dimension (Stevenson, 2013).

The microelectronic industry is facing important challenges in the reliability of 3-dimensional integrate circuits (Bernstein et al., 2007; Tu, 2011; Sung et al., 2011; Ramm et al., 2010). In 3D-IC technology, chips and package are merging closer in a single compact multiscale structure. Figure 1.1 shows a cross section of a two-level package based on solder joints, with typical dimensions showing the multiscale nature of the problem, from several milimiters in the motherboard to a few nanometers in the chip. In this context, Joule heating and vertical interconnect are the two main

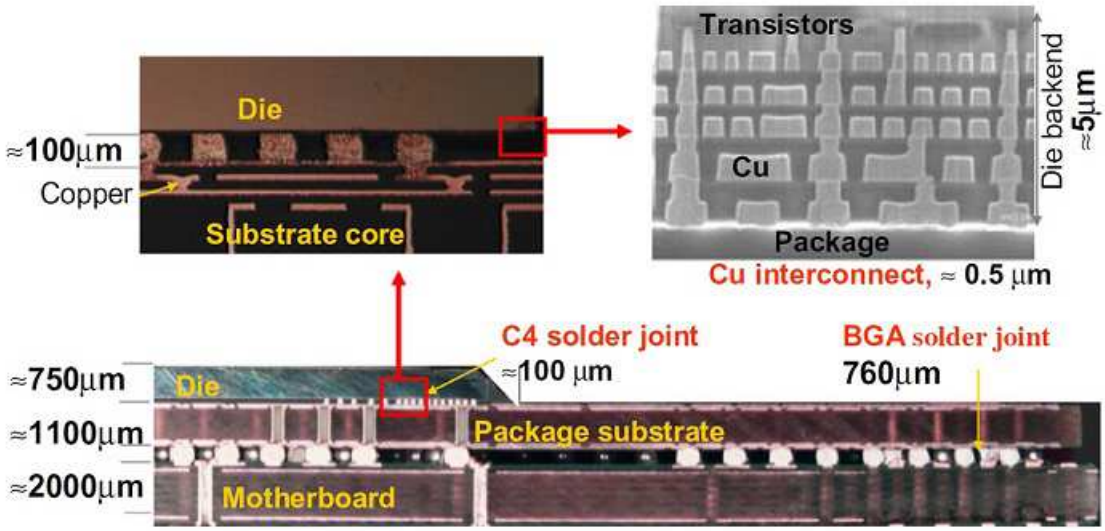

FIGURE 1.1: Typical dimensions in a multiscale package-to-chip structure (Courtesy of Prof. Tu, UCLA).

problems to be solved (Tu, 2011). About the later, the potential issues on correct propagation of electromagnetic waves through the interconnect network should be analyzed in detail. In order to help in this task, efficient, and accurate multiscale simulators must be developed.

In general, simulation of short electromagnetic pulse propagation through complex environments provides highly valuable wideband information in the time domain (Wedge et al., 2005; Ghosh et al., 2006; Cohen and Gaunaurd, 2002). Signal integrity, power integrity, electromagnetic compatibility, electromagnetic interference and time domain reflectometry are evaluation methods based on transient analysis of broadband pulses. Furthermore, Fourier transform of a single transient simulation provides frequency domain results over a wide frequency band. Evidently, these wideband analyses require highly accurate numerical methods in a broad range of frequencies to capture the correct behavior of the physical system (Cohen and Gaunaurd, 2002; Ainsworth and Wajid, 2009; Ainsworth, 2004b,a; Stanescu et al., 2000; Tobon et al., 2011; Melvin et al., 2012).

The conventional Finite-Difference in Time-Domain (FDTD) method and Finite-Element in Time-Domain (FETD) method have serious difficulties to solve multiscale EM systems. FDTD is a well-known, efficient and simple-to-implement method that uses an orthogonal grid to discretize the structure (Taflove and Brodwin, 1975). Thus, high density discretization is required to capture electrically fine structures with the waste of unknowns in coarse parts. Another issue of FDTD method is its conditional stability for solving the time integration, i.e. electrically small structures will lead to very small (usually non-practical) time step. The FETD method (Jin, 2002) is more flexible in geometry modeling, but requires solving, either directly or iteratively, matrix equations (usually huge in multiscale systems) in each time step. In summary, a good numerical method for solving large and multiscale EM problems must be flexible in modeling, accurate, and efficient.

The discontinuous Galerkin in the time domain (DGTD) method is useful in transient simulations of multiscale electromagnetic systems (Hesthaven and Warburton, 2007; Lee et al., 2009; Chen et al., 2011). Its special capability in geometric modeling, by dividing the whole computational domain into several subdomains, transforms a large system into several moderate-sized matrix equations. Another advantage of this method is that each subdomain can be discretized, in space and time, independently. The numerical fluxes, which communicate fields between domains, are defined by tangential components of $\mathbf{E}$ and $\mathbf{H}$ on the interfaces (Mohammadian et al., 1991). For this reason, the conventional DGTD is traditionally based on these two variables; however, there is not restriction to use any other set of fields. About this important subject is the present work.

The first chapter of this dissertation describes a unified framework, based on the theory of differential forms and the finite element method, used to analyze basis functions employed to discretize the Maxwell's equations. This analysis is supported on numerical dispersion analysis, eigenvalues and eigenvectors evaluation, and transient

solutions, which are described in the second chapter.

In the third chapter, two DGTD methods based on both **E** and **H** fields, and **E** and **B** fields are studied. For the former, curl-conforming basis functions with different order of interpolations are selected to eliminate spurious solutions. In the later, divergence- and curl-conforming basis functions with same order of interpolation are used to discretize the fields, keeping similar accuracy and number of unknowns in both families of basis functions; thus, a very efficient, accurate and free-of-spurious numerical method is available. Finally, in the fourth chapter realistic cases show the power of the proposed method.

1.1 Main contributions of this dissertation

There are six main contributions related with different level of abstraction of the DGTD method. From a mathematical framework for studing the discretization of Maxwell's, to the implementation of algorithms for time integration. The main contributions can be enumerated as follows:

1. A unified framework based on the theory of differential forms and the finite element method. It is used to analyze the discretization of the Maxwells equations.

2. Numerical analysis based on modal analysis for one- and two- dimensional spectral elements. Comparison with analytical formulas of numerical dispersion based on semidiscrete analysis.

3. Study of dispersive Hodge Operator. Phase velocity analysis provides same conclusion as previous dispersion analysis.

4. Implementation, analysis and application of Spectral-Prism element for EH

DGTD; including single domain performance analysis, and applications to multiple domain and multi-layered EM cases.

5. Formulation, implementation and application of new LDU algorithm for highly multiscale EM cases decomposed in sequential order.

6. Implementation of first and second order divergence-conforming tetrahedral element for EB DGTD; including single domain performance analysis, and applications to multiple domain and multiscale EM cases.

2

Governing equations and discretized electromagnetics

The classical approach for solving electromagnetic problems is vector calculus. In this classical approach space and time are assumed infinite divisible. Traditional discretization methods, such as finite difference, finite elements and finite volume, are based on this vector calculus formulation (Taflove and Brodwin, 1975; Jin, 2002). These methods involve approximations which hide the independency between topological and metric structures, and produce in some cases non-consistent numerical methods (Teixeira and Chew, 1999). Some effects of inconsistency are late-time instabilities and spurious modes (Bermudez and Pedreira, 1992; Winkler et al., 1984; Tobón et al., 2011; Schuhmann and Weiland, 1998).

Over the last decades, the finite element method (FEM) has been a very popular numerical method because of its flexibility to model efficiently interesting problems in several areas of physics and engineering (Jin, 2002; Monk, 2003; Peterson et al., 1998; Solín et al., 2004). Traditionally, the Galerkin method has been widely used in the finite element method to seek the solution by weighting of electromagnetic

equations. In this method, the precise definition of basis functions is fundamental to correctly discretize electromagnetic systems. Particularly, curl-conforming basis functions properly model discontinuous fields across material discontinuities, eliminate spurious modes, and conserve the charge in time dependent simulations (Peterson et al., 1998; Jin, 2002), when is applied to the second order electromagnetic equation. However, first order Maxwell's equations require a more precise selection of basis functions to represent the electric and magnetic fields in the same discretized system (Chen and Liu, 2009; Tobón et al., 2011).

Recently, an alternative approach to analyze FEM is based on differential forms to represent topological and constitutive relations between fields (Kotiuga, 1989; Tarhasaari et al., 1999; Teixeira and Chew, 1999; Castillo et al., 2004; Hiptmair, 2001). In this geometric approach, field intensities are 1-forms and flux densities are 2-forms. These p-forms can define compact governing equations using differential operators, such as the exterior derivative, the wedge product, and the Hodge star operator. Furthermore, topological and metric aspects are well separated; in particular, metric aspects are present only in the Hodge operator. This operator generalizes the constitutive relations of the medium (Hiptmair, 2001; He and Teixeira, 2006b).

An important problem of the differential forms approach is the representation, on the discrete level, of 1-forms and 2-forms simultaneously in the same mesh (Hiptmair, 2001; Tarhasaari et al., 1999). This issue was partially solved using a pair of dual grids, called primary and secondary meshes. This solution considers Maxwell's equations as two topologically distinct and not linked equations (Hiptmair, 2001). Several works have shown conceptual and numerical advantages of this representation for low order numerical methods (White et al., 2006; He and Teixeira, 2006a, 2007). However, in higher order discrete differential forms the matrices of the exterior derivative are no longer incidence matrices, and it is very hard to develop a secondary mesh (Hiptmair, 2001).

An alternative route is a unified framework based on the theory of differential forms for construction and study of conforming finite element space. Then, curl-conforming H(curl) and divergence-conforming H(div) finite element spaces, their degree of freedoms, and interpolation operators arise naturally from this framework. Thus, the finite element basis functions satisfy the discrete version of the exact De Rham sequence, and Hodge operators are defined from the finite element spaces.

2.1 Governing equations: Maxwell's Equations

2.1.1 Topological laws

The first order Maxwell's equations for electric field and magnetic field due to imposed current densities are considered:

$$\frac{\partial \mathbf{D}}{\partial t} = \nabla \times \mathbf{H} - \mathbf{J}_c - \mathbf{J}_s \tag{2.1}$$

$$-\frac{\partial \mathbf{B}}{\partial t} = \nabla \times \mathbf{E} + \mathbf{M}_c + \mathbf{M}_s \tag{2.2}$$

$$\nabla \cdot \mathbf{D} = \rho_e \tag{2.3}$$

$$\nabla \cdot \mathbf{B} = \rho_m \tag{2.4}$$

where $\mathbf{E}$ and $\mathbf{H}$ are the electric and magnetic field intensities, respectively; $\mathbf{D}$ and $\mathbf{B}$ are the electric and magnetic flux densities, respectively; $\mathbf{J}_c$ and $\mathbf{M}_c$ are the electric and magnetic current densities, respectively; $\mathbf{J}_s$ and $\mathbf{M}_s$ are electric and magnetic imposed sources, respectively; and ρ_e and ρ_m are electric and magnetic charge densities, respectively.

2.1.2 Constitutive laws

Material properties define the relations between field intensities and flux densities as follows:

$$\mathbf{D} = \epsilon \mathbf{E} \tag{2.5}$$

$$\mathbf{B} = \mu \mathbf{H} \tag{2.6}$$

$$\mathbf{J}_c = \sigma_e \mathbf{E} \tag{2.7}$$

$$\mathbf{M}_c = \sigma_m \mathbf{H} \tag{2.8}$$

where ϵ, μ, σ_e, and σ_m are the electrical and magnetic properties of the medium corresponding to permittivity, permeability, electric conductivity, and magnetic conductivity, respectively.

With an abstraction of the time derivatives and assuming a sourceless domain, the Maxwell's equations (2.1) - (2.2) and the constitutive relations (2.5) - (2.6) can be summarized in the next diagram:

$$\begin{array}{ccccccc} & & \mathbf{E} & \overset{\nabla\times}{\rightarrow} & \mathbf{B} & \overset{\nabla\cdot}{\rightarrow} & \rho_m \\ & & \epsilon \downarrow & & \mu \uparrow & & \\ \rho_e & \overset{\nabla\cdot}{\leftarrow} & \mathbf{D} & \overset{\nabla\times}{\leftarrow} & \mathbf{H} & & \end{array} \tag{2.9}$$

In this diagram horizontal arrows represent fields transformation based on differential operators (i.e., gradient, curl, and divergence), and vertical arrows represent field transformations based on material properties (i.e., permittivity and permeability). It is important to note that this diagram describes the physical relations which must be satisfied by the basis functions used to represent electric and magnetic fields.

These functions, which belong to the Hilbert-Sobolev space, will be discussed in the following sections.

2.2 The Finite Element Method

Finite element is defined, using Ciarlet approach (Ciarlet, 1978; Solín et al., 2004), as a triad $\mathcal{K} = (K_\alpha, Q, \Sigma)$, where

- Element: K_α, is a geometrical shape in $\mathbb{R}^d$. The set form by all K_α is called *mesh* $\mathcal{T} = \{K_1, K_2, \ldots, K_M\}$, and the union of all the closures of K_α represents the domain $\Omega = \bigcup_{all\,\alpha} \overline{K_\alpha}$
- Family of basis functions: Q is a polynomial space in K_α.
- Unknowns: $\Sigma = \{v_1, v_2, \ldots, v_{N_P}\}$ is a set of linear forms. The number of elements of Σ is called the degrees of freedom (DoF).

2.2.1 The Hilbert-Sobolev space

The family of functions used in finite elements belongs to the Hilbert-Sobolev space of functions (H^1, $\mathbf{H}(curl)$, $\mathbf{H}(div)$, and L^2)(Solín et al., 2004), in a bounded domain $\Omega \subset \mathbb{R}^d$, d being the spatial dimensionality:

$$H^1(\Omega) = \left\{ u \in L^2(\Omega); \frac{\partial u}{\partial x_i} \in L^2(\Omega), 1 \leq i \leq d \right\} \tag{2.10}$$

$$\mathbf{H}(\Omega; curl) = \left\{ \mathbf{u} \in \left[L^2(\Omega)\right]^d; \nabla \times \mathbf{u} \in \left[L^2(\Omega)\right]^d \right\} \tag{2.11}$$

$$\mathbf{H}(\Omega; div) = \left\{ \mathbf{u} \in \left[L^2(\Omega)\right]^d; \nabla \cdot \mathbf{u} \in L^2(\Omega) \right\} \tag{2.12}$$

$$L^2(\Omega) = \left\{ u : \Omega \to \mathbb{R} | \int_\Omega |u|^2 \, dx < \infty \right\} \tag{2.13}$$

Global conformity requirements are defined for these functions. Assume two neighbor elements $K_1, K_2 \in \mathcal{T}$, with a face in common $f = \overline{K_1} \bigcap \overline{K_2}$, and $\mathbf{n}$ the normal vector to the face f

- $u|_{K_\alpha} \in H^1(K_\alpha)$ imposes the continuity of u between neighbor elements: $u|_{K_1} = u|_{K_2}$on f.
- $\mathbf{u}|_{K_\alpha} \in \mathbf{H}(K_\alpha; curl)$ imposes the continuity of the tangential components: $\mathbf{n} \times \mathbf{u}|_{K_1} = \mathbf{n} \times \mathbf{u}|_{K_2}$on f.
- $\mathbf{u}|_{K_\alpha} \in \mathbf{H}(K_\alpha; div)$ imposes the continuity of the normal components: $\mathbf{n} \cdot \mathbf{u}|_{K_1} = \mathbf{n} \cdot \mathbf{u}|_{K_2}$on f.

The De Rham diagram relates the function spaces used in finite elements by means of differential operators.

$$H^1 \overset{\nabla}{\to} \mathbf{H}(curl) \overset{\nabla \times}{\to} \mathbf{H}(div) \overset{\nabla \cdot}{\to} L^2 \tag{2.14}$$

In this diagram, the range of each operator is the null-space of the next one. Hence, finite elements are understood as a sequence of scalar and vector-value elements satisfying the De Rham diagram on the discrete level (Solín et al., 2004).

2.3 Differential Forms

Consider ω to be a differential form of degree p (p-form) in a three dimensional manifold, C^p, with boundary. Integration $\int_c \omega$ should be understood as a bilinear pairing between ω and an oriented p-dimensional domain c. If ∂c is the boundary of c, then the exterior derivative $d : C^p \to C^{p+1}$ is defined as follows

$$\int_{\partial c} \omega = \int_{c} d\omega$$

This is the "Stokes' theorem on manifolds", which is a coordinate and metric independent generalization of the Stokes' theorem

The collection of all differential forms on a manifold and the exterior derivative form the De Rham complex:

$$C^0 \overset{d}{\rightarrow} C^1 \overset{d}{\rightarrow} C^2 \overset{d}{\rightarrow} C^3$$

Metric aspects are introduced by the Hodge star operator $\star : C^p \rightarrow C^{3-p}$ which is defined locally with a metric tensor. Thus, a Tonti diagram (Tonti, 2002) can be obtain

$$\begin{array}{ccccccc} C^0 & \overset{d}{\rightarrow} & C^1 & \overset{d}{\rightarrow} & C^2 & \overset{d}{\rightarrow} & C^3 \\ \updownarrow \star & & \updownarrow \star & & \updownarrow \star & & \updownarrow \star \\ C^3 & \overset{d}{\leftarrow} & C^2 & \overset{d}{\leftarrow} & C^1 & \overset{d}{\leftarrow} & C^0 \end{array} \tag{2.15}$$

From the physics in diagram (2.9), the family of basis functions in (2.14), and the Tonti diagram (2.15) can be defined in the following sequence:

$$\begin{array}{ccccccc} C^0 & \overset{d}{\longrightarrow} & C^1 & \overset{d}{\longrightarrow} & C^2 & \overset{d}{\longrightarrow} & C^3 \\ H^1 & & \mathbf{H}\,(curl) & & \mathbf{H}\,(div) & & L^2 \\ \Phi_E & \overset{\nabla}{\longrightarrow} & \mathbf{E} & \overset{\nabla\times}{\longrightarrow} & \mathbf{B} & \overset{\nabla\cdot}{\longrightarrow} & \rho_m \\ & & \star_\epsilon \downarrow\uparrow \star_{1/\epsilon} & & \star_{1/\mu} \downarrow\uparrow \star_\mu & & \\ \rho_e & \overset{\nabla\cdot}{\longleftarrow} & \mathbf{D} & \overset{\nabla\times}{\longleftarrow} & \mathbf{H} & \overset{\nabla}{\longleftarrow} & \Phi_M \\ L^2 & & \mathbf{H}\,(div) & & \mathbf{H}\,(curl) & & H^1 \\ C^3 & \overset{d}{\longleftarrow} & C^2 & \overset{d}{\longleftarrow} & C^1 & \overset{d}{\longleftarrow} & C^0 \end{array} \tag{2.16}$$

This diagram shows a complete sequence of scalar potentials (Φ_E and Φ_M), field intensities ($\mathbf{E}$ and $\mathbf{H}$), flux densities ($\mathbf{D}$ and $\mathbf{B}$) and charge densities (ρ_e and ρ_m).

In this diagram, scalar potentials are associated with H^1 and 0-form; field intensities with $\mathbf{H}(curl)$ and 1-form; flux densities with $\mathbf{H}(div)$ and 2-form ; and charge densities with L^2 and 3-forms. In this sequence, discrete p-forms are finite element basis functions used to discretize p-forms fields. Similarly, discrete Hodge operators relate complementary discrete p-form fields, i.e., fields intensities with flux desitites, or $\mathbf{H}(curl)$ with $\mathbf{H}(div)$ basis functions. These operators are function of material properties, basis functions, element shape and wavenumber; therefore, the Hodge operators contain information of numerical dispersion of the discrete system.

2.4 The Galerkin's Method

In this work, $\mathbf{\Phi}^{\alpha}$ $(\alpha = E, H)$, and $\mathbf{\Psi}^{\beta}(\beta = D, B)$ represent curl-conforming and divergence-conforming basis functions, respectively. These family of basis functions are used to approximate electromagnetic fields:

$$\mathbf{E} \approx \sum_{j=1}^{N_E} e_j \mathbf{\Phi}_j^E \tag{2.17}$$

$$\mathbf{H} \approx \sum_{j=1}^{N_H} h_j \mathbf{\Phi}_j^H \tag{2.18}$$

$$\mathbf{D} \approx \sum_{j=1}^{N_D} d_j \mathbf{\Psi}_j^D \tag{2.19}$$

$$\mathbf{B} \approx \sum_{j=1}^{N_B} b_j \mathbf{\Psi}_j^B \tag{2.20}$$

where e_j , h_j, d_j and b_j are the unknowns to be solved. The weak form of the Maxwell's equations (2.1 and 2.2) in free space are:

$$\int_{\Omega} \mathbf{\Theta}_p \cdot \left(\frac{\partial \mathbf{D}}{\partial t} = \nabla \times \mathbf{H} - \mathbf{J} \right) dV = 0 \tag{2.21}$$

$$\int_{\Omega} \mathbf{\Upsilon}_q \cdot \left(\frac{\partial \mathbf{B}}{\partial t} = -\nabla \times \mathbf{E} - \mathbf{M} \right) dV = 0 \tag{2.22}$$

where $\mathbf{\Theta}_p$ and $\mathbf{\Upsilon}_q$ are testing functions selected according with the basis functions used to represent $\mathbf{D}$ and $\mathbf{B}$. Several schemes can be defined depending on the fields to be discretized.

If $\mathbf{E}$ and $\mathbf{H}$ are selected, the system of equations is:

$$\mathbf{M}_{ee} \frac{d\mathbf{e}}{dt} = \mathbf{K}_{eh}\mathbf{h} + \mathbf{C}_{ee}\mathbf{e} + \mathbf{j} \tag{2.23}$$

$$\mathbf{M}_{hh} \frac{d\mathbf{h}}{dt} = \mathbf{K}_{he}\mathbf{e} + \mathbf{C}_{hh}\mathbf{h} + \mathbf{m} \tag{2.24}$$

where $\mathbf{e}$ and $\mathbf{h}$ are unknown vectors, $\mathbf{j}$ and $\mathbf{m}$ are the vectors for discretized excitations, $\mathbf{M}_{ee}$ and $\mathbf{M}_{hh}$ are the mass matrices, $\mathbf{C}_{ee}$ and $\mathbf{C}_{hh}$ are the damping matrices, $\mathbf{K}_{eh}$ and $\mathbf{K}_{he}$ are the stiffness matrices. By defining the integral of two functions as $\langle \mathbf{f}, \mathbf{g} \rangle_{V_e} = \int_{V_e} \mathbf{f}^T \cdot \mathbf{g} dV$, where V_e is an element volume, the elemental form of these matrices are

$$(\mathbf{M}_{ee})^e_{kl} = \langle \mathbf{\Phi}^E_k, \epsilon \mathbf{\Phi}^E_l \rangle_{V_e} \qquad (\mathbf{M}_{hh})^e_{kl} = \langle \mathbf{\Phi}^H_k, \mu \mathbf{\Phi}^H_l \rangle_{V_e} \tag{2.25}$$

$$(\mathbf{C}_{ee})^e_{kl} = \langle \mathbf{\Phi}^E_k, \sigma_e \mathbf{\Phi}^E_l \rangle_{V_e} \quad (\mathbf{C}_{hh})^e_{kl} = \langle \mathbf{\Phi}^H_k, \sigma_m \mathbf{\Phi}^H_l \rangle_{V_e} \tag{2.26}$$

$$(\mathbf{K}_{eh})^e_{kl} = \langle \mathbf{\Phi}^E_k, \nabla \times \mathbf{\Phi}^H_l \rangle_{V_e} \tag{2.27}$$

$$(\mathbf{K}_{he})^e_{kl} = -\langle \mathbf{\Phi}^H_k, \nabla \times \mathbf{\Phi}^E_l \rangle_{V_e} \tag{2.28}$$

$$(\mathbf{j})^e_k = -\langle \mathbf{\Phi}^E_k, \mathbf{J} \rangle_{V_e} \qquad (\mathbf{m})^e_k = -\langle \mathbf{\Phi}^H_k, \mathbf{M} \rangle_{V_e} \tag{2.29}$$

Similarly, if **E** and **B** are selected, the linear system is:

$$\mathbf{M}_{ee}\frac{d\mathbf{e}}{dt} = \mathbf{K}_{eb}\mathbf{b} + \mathbf{C}_{ee}\mathbf{e} + \mathbf{j} \tag{2.30}$$

$$\mathbf{M}_{bb}\frac{d\mathbf{b}}{dt} = \mathbf{K}_{be}\mathbf{e} + \mathbf{C}_{bb}\mathbf{b} + \mathbf{m} \tag{2.31}$$

where $\mathbf{b}$ is unknown vector, $\mathbf{M}_{bb}$ is the mass matrices, and $\mathbf{K}_{eb}$ and $\mathbf{K}_{be}$ are the stiffness matrices. The elemental form of these matrices are

$$(\mathbf{M}_{bb})^e_{kl} = \langle \mathbf{\Psi}^B_k, \mathbf{\Psi}^B_l \rangle_{V_e} \tag{2.32}$$

$$(\mathbf{M}_{dd})^e_{kl} = \langle \mathbf{\Psi}^D_k, \mathbf{\Psi}^D_l \rangle_{V_e} \tag{2.33}$$

$$(\mathbf{C}_{bb})^e_{kl} = \langle \mathbf{\Psi}^B_k, \sigma_m \mu^{-1} \mathbf{\Psi}^B_l \rangle_{V_e} \tag{2.34}$$

$$(\mathbf{K}_{eb})^e_{kl} = \langle \nabla \times \mathbf{\Phi}^E_k, \mu^{-1} \mathbf{\Psi}^B_l \rangle_{V_e} \tag{2.35}$$

$$(\mathbf{K}_{be})^e_{kl} = -\langle \mathbf{\Psi}^B_k, \nabla \times \mathbf{\Phi}^E_l \rangle_{V_e} \tag{2.36}$$

If **E**, **H**, **D** and **B** are choosen, the equations are:

$$\mathbf{M}_{dd}\frac{d\mathbf{d}}{dt} = \mathbf{K}_{dh}\mathbf{h} + \mathbf{C}_{ee}\mathbf{e} + \mathbf{j} \tag{2.37}$$

$$\mathbf{M}_{bb}\frac{d\mathbf{b}}{dt} = \mathbf{K}_{be}\mathbf{e} + \mathbf{C}_{hh}\mathbf{h} + \mathbf{m} \tag{2.38}$$

In this case, the formulations for mass and stiffness matrices are strictly topological, and material properties are defined by Hodge operators as follows

$$\mathbf{d} = \star_{\epsilon}\mathbf{e} = \epsilon_0\mathbf{M}_{dd}^{-1}\mathbf{M}_{de}\mathbf{e} \tag{2.39}$$

$$\mathbf{b} = \star_{\mu}\mathbf{h} = \mu_0\mathbf{M}_{bb}^{-1}\mathbf{M}_{bh}\mathbf{h} \tag{2.40}$$

$$\mathbf{e} = \star_{1/\epsilon}\mathbf{d} = \frac{1}{\epsilon_0}\mathbf{M}_{ee}^{-1}\mathbf{M}_{ed}\mathbf{d} \tag{2.41}$$

$$\mathbf{h} = \star_{1/\mu}\mathbf{b} = \frac{1}{\mu_0}\mathbf{M}_{hh}^{-1}\mathbf{M}_{hb}\mathbf{b} \tag{2.42}$$

It is important to note that $\star_{1/\alpha}$ is not a simple inverse of $\star_{\alpha}$.

2.5 Basis functions

2.5.1 Square spectral element

To discretize the Maxwell's equations with spectral accuracy, the roots of the derivative of the Gauss-Lobatto-Legendre polynomials are the interpolation points of the vector basis functions (Lee et al., 2006; Lee and Liu, 2007; Chen and Liu, 2009). In addition, mixed-order curl conforming vector basis functions are employed to guarantee the tangential continuity across a shared edge between two elements. On a 2D standard square reference element $(\xi, \eta) \in [-1, 1] \times [-1, 1]$, the Mth-order curl-conforming basis functions for electric field intensity are defined as

$$\hat{\mathbf{\Phi}}_{ij}^{\xi}(\xi, \eta) = \phi_i^{(M-1)}(\xi)\,\phi_j^{(M)}(\eta) \tag{2.43}$$

$$\hat{\mathbf{\Phi}}_{ij}^{\eta}(\xi,\eta) = \phi_i^{(M)}(\xi)\,\phi_j^{(M-1)}(\eta) \tag{2.44}$$

To satisfy the tangential continuity across interfaces between elements, we employ the mapping of basis functions from the reference to the physical domains by (Peterson et al., 1998)

$$\mathbf{\Phi} = \mathbf{J}^{-1}\hat{\mathbf{\Phi}} \tag{2.45}$$

$$\nabla \times \mathbf{\Phi} = \frac{\mathbf{J}^T}{|\mathbf{J}|}\hat{\nabla} \times \hat{\mathbf{\Phi}} \tag{2.46}$$

where $\mathbf{\Phi}$ and $\hat{\mathbf{\Phi}}$ represent the basis functions in the physical and reference elements, respectively, and $\mathbf{J}$ is the Jacobian matrix (Peterson et al., 1998).

The Mth-order curl-conforming basis function for magnetic field intensity is defined as

$$\hat{\mathbf{\Phi}}_{ij}(\xi,\eta) = \phi_i^{(M)}(\xi)\,\phi_j^{(M)}(\eta) \tag{2.47}$$

For this kind of basis function, to satisfy tangential continuity, unknowns on the boundary of the element are shared with neighbor elements.

The Mth-order divergence-conforming basis functions for electric flux density are defined as

$$\hat{\mathbf{\Psi}}_{ij}^{\xi}(\xi,\eta) = \phi_i^{(M)}(\xi)\,\phi_j^{(M-1)}(\eta) \tag{2.48}$$

$$\hat{\mathbf{\Psi}}_{ij}^{\eta}(\xi,\eta) = \phi_i^{(M-1)}(\xi)\,\phi_j^{(M)}(\eta) \tag{2.49}$$

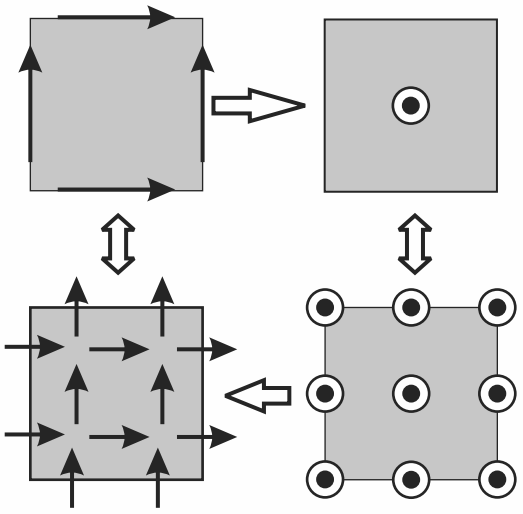

FIGURE 2.1: Schematic De Rham diagram for square spectral elements. Horizontal arrows represent differential operators, and vertical arrows represent Hodge operators.

To satisfy the normal continuity across interfaces between elements, we employ the mapping of basis functions from the reference to the physical domains by (Peterson et al., 1998)

$$\mathbf{\Psi} = \frac{\mathbf{J}^T}{|\mathbf{J}|}\hat{\mathbf{\Psi}} \tag{2.50}$$

$$\nabla \times \mathbf{\Psi} = \mathbf{J}^{-1}\hat{\nabla} \times \hat{\mathbf{\Psi}} \tag{2.51}$$

where $\mathbf{\Psi}$ and $\hat{\mathbf{\Psi}}$ represent the basis functions in the physical and reference elements, respectively.

The Mth-order divergence-conforming basis function for magnetic flux density is defined as

$$\hat{\mathbf{\Psi}}_{ij}(\xi, \eta) = \phi_i^{(M-1)}(\xi)\,\phi_j^{(M-1)}(\eta) \tag{2.52}$$

For this kind of basis function, unknowns are not shared between elements, i.e.

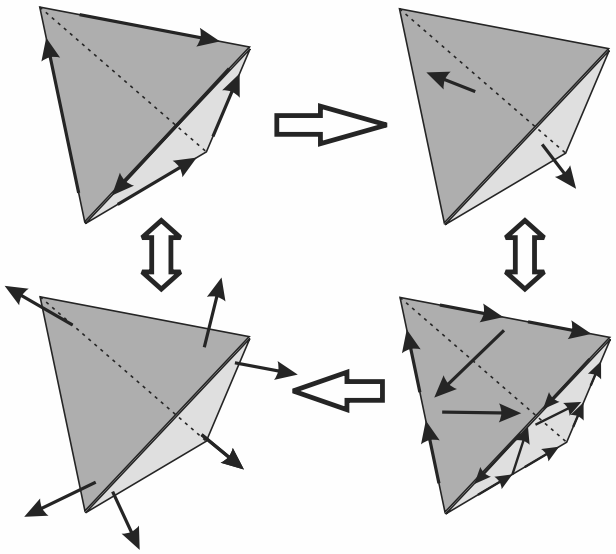

FIGURE 2.2: Schematic De Rham diagram for vector basis functions in section a tetrahedron. Horizontal arrows represent differential operators, and vertical arrows represent Hodge operators.

this functions are discontinuous between elements.

2.5.2 Vector basis functions in a reference tetrahedron

Four families of basis functions are used to represent the electric and magnetic fields, with a schematic De Rham sequence shown in Figure (2.2). Two are curl conforming basis fuctions: Constant-tangential/Linear-normal (Ct/Ln) and Linear-tangential/Quadratic-normal (Lt/Qn); and the other two are divergence conforming: Constant-normal/Linear-tangential (Cn/Lt), and Linear-normal/Quadratic-tangential (Ln/Qt). Formulations for these family of basis functions are:

- Constant-tangential/Linear-normal, one basis function per edge ($\hat{\mathbf{\Phi}}_{ij}^{CtLn}$).

$$\hat{\mathbf{\Phi}}_{ij}^{CtLn} = s_i \nabla s_j - s_j \nabla s_i \tag{2.53}$$

- Linear-tangential/Quadratic-normal, two basis functions per edge ($\hat{\mathbf{\Phi}}_{ij}^{LtQn}$) and two per face ($\hat{\mathbf{\Phi}}_{ijk}^{LtQn}$).

$$\hat{\mathbf{\Phi}}_{ij}^{LtQn} = s_i \nabla s_j \tag{2.54}$$

$$\hat{\mathbf{\Phi}}_{ijk}^{LtQn} = s_i s_k \nabla s_j - s_j s_k \nabla s_i \tag{2.55}$$

- Constant-normal/Linear-tangential, ona basis function per face ($\mathbf{\Psi}_{ijk}^{CnLt}$).

$$\hat{\mathbf{\Psi}}_{ijk}^{CnLt} = 2\left(s_i \vec{v}_{jk} + s_j \vec{v}_{ki} + s_k \vec{v}_{ij}\right) \tag{2.56}$$

- Linear-normal/Quadratic-tangential, three basis functions per face($\hat{\mathbf{\Psi}}_{ij}^{LnQt}$) and three in the volume ($\hat{\mathbf{\Psi}}_{ijkl}^{LnQt}$).

$$\hat{\mathbf{\Psi}}_{ijk}^{LnQt} = s_i \vec{v}_{jk} \tag{2.57}$$

$$\hat{\mathbf{\Psi}}_{ijkl}^{LnQt} = 2 s_l \left(s_i \vec{v}_{jk} + s_j \vec{v}_{ki} + s_k \vec{v}_{ij}\right) \tag{2.58}$$

where s_p is the barycentric coordinate of the p-th vertex, and $\vec{v}_{ij} = \nabla s_i \times \nabla s_j$.

2.5.3 Basis functions in the reference prism element

The low order family of basis functions (see Fig. 2.3a) are divided in two sets, one transverse to the height of the prism, and the other in height direction. The first set can be described in terms of a Constant-tangential/Linear-normal triangular edge basis, $B_{ij}^{(1)}$, and a Nth-order polynomial variation in the height of the prism, with $N+1$ Gauss–Lobatto–Legendre points, i.e., the roots of the derivative of the Gauss–Lobatto–Legendre polynomials (Lee et al., 2006; Lee and Liu, 2007).

$$\mathbf{\Phi}_{\mathbf{1}ik}^{(1,N)}(\xi,\eta,\varsigma) = \mathbf{B}_i^{(1)}(\xi,\eta)\,\phi_k^{(N)}(\varsigma) \tag{2.59}$$

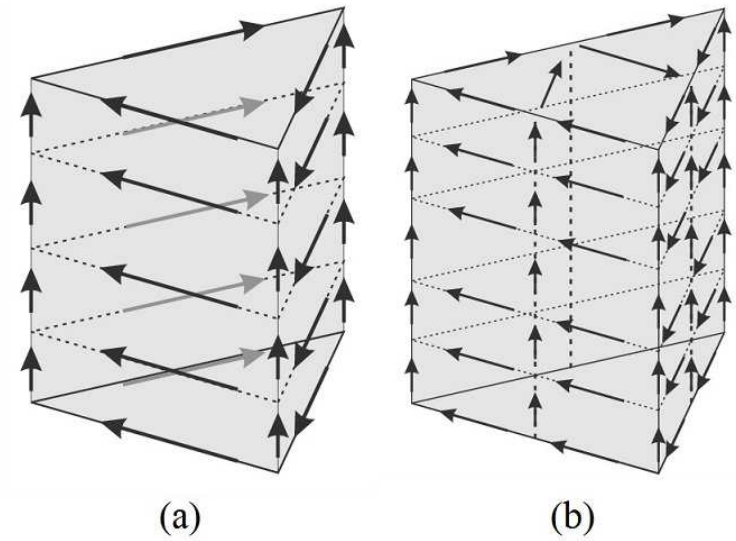

FIGURE 2.3: Spectral prism elements: (a) Ct/Ln and 4th order in height, and (b) Lt/Qn and 5th order in height

with $i = 1, 2, 3; k = 1, 2, \cdots, N+1$ and where,

$$\mathbf{B}_i^{(1)}(\xi, \eta) = (N_{i+1} \boldsymbol{\nabla} N_{i+2} - N_{i+2} \boldsymbol{\nabla} N_{i+1}) \tag{2.60}$$

The second set of low order basis functions are along the height direction, first order nodal basis function in the triangle and $(N-1)$th-order in the polynomial:

$$\boldsymbol{\Phi}_{\mathbf{2}}{}_{ik}^{(1,N)}(\xi, \eta, \varsigma) = \hat{\varsigma} N_i(\xi, \eta) \phi_k^{(N-1)}(\varsigma) \tag{2.61}$$

with $i = 1, 2, 3; k = 1, 2, \cdots, N$

Similarly, a higher order family of basis functions (see Fig. 2.3b) is implemented using Linear-tangential/Quadratic-normal triangle edge basis functions, $B_{ij}^{(2)}$, and second order nodal basis functions for the height direction.

3

Single Domain Analysis

Transient and broadband analysis of electrically large environments requires even more accurate numerical simulators (Liu, 1999; Wang and Teixeira, 2003). In those cases, a highly dispersive numerical method produces a large phase lead or lag, producing completely wrong results. Even worse, in some cases, undesirable spurious solutions are produced if the discretized system is not correctly obtained by appropiate basis functions (Chen and Liu, 2009; Davies et al., 1982; Tobón et al., 2011). Therefore, an appropriate numerical method must have four main features: high accuracy, low numerical dispersion, free of spurious modes, and low computational cost.

Many investigators have studied the numerical dispersion error introduced in the numerical solution of dynamic systems. Most of these works discuss the dispersive behavior of the Finite and Spectral Element Method for scalar and one-dimensional wave equations (Ainsworth and Wajid, 2009; Seriani and Oliveira, 2008; Abboud and Pinsky, 1992; Ihlenburg and Babuška, 2005; Ainsworth, 2004b). Generally, closed-form expressions are found under some specific approximations. Some approaches used by these authors are eigenvalue analysis (De Basabe and Sen, 2007),

the Padé approximations (Ainsworth and Wajid, 2009), and the Rayleigh quotient (Seriani and Oliveira, 2008; Tobón et al., 2011).

The approach presented in this work is similar to the one introduced by Seriani and Oliveira in the analysis of the 2D elastic wave equation, but in this case, it is applied to Maxwell's equations. The main point of this approach is to find an approximated eigenvalue associated to a specifically calculated approximated eigenvector. This vector is defined by the projection of a harmonic plane wave with a corresponding wavenumber and angle of propagation in the discretized field, i.e., a vector of unknowns. The best approximate eigenvalue is calculated by the Rayleigh quotient. Then, changing the wavenumber and angle of propagation a complete surface in the space of wavenumbers can be calculated, for further extraction of errors in wavenumber, phase and group velocities, and to evaluate whether spurious solutions exist.

In summary, this chapter has one main aim: to verify the family of basis functions defined in the previous chapter, which are used to discretize electric and magnetic fields when both fields are in the same system of equations. This analysis will be supported on numerical dispersion, error in eigenvalues and eigenvectors, and transient solutions. Also, a new method to evaluate numerical dispersion based on the phase velocity calculated from the electric and magnetic Hodge operators will be presented for the first time.

3.1 Eigensolutions

First, assuming harmonic variation, $\frac{d}{dt} \rightarrow j\omega$, we can easily transform time domain formulations (2.23), (2.24), (2.30), and (2.31) into the frequency domain. Thus, the eigenproblem can be defined as follow

$$\mathbf{Y}\mathbf{v} = \chi\mathbf{X}\mathbf{v} \tag{3.1}$$

where matrices $\mathbf{X} = \mathbf{M}_{\alpha\alpha}$ and $\mathbf{Y} = -\mathbf{K}_{\alpha\beta}\left[\mathbf{M}_{\beta\beta}\right]\mathbf{K}_{\beta\alpha}$ are defined according with the selected formulation; a vector $\mathbf{v}$ represents eigenvectors, and $\chi = \left(\frac{\omega}{c_0}\right)^2$ represents eigenvalues.

For reasonable numerical results, we expect the eigenvectors to be close to the true electric field patterns, and the wavenumbers (eigenvalues) allowed in the physical system modeled and solved by the numerical method. Consequently, eigensolutions without a physical meaning are spurious ones, and must be removed. In frequency domain, checking the eigenvectors is enough to discard spurious solutions, but in time domain, this method of removing spurious solution is not feasible.

3.2 Dispersion analysis

3.2.1 Modal analysis based on the Rayleigh quotient

To study the numerical dispersion of the discretized Maxwell's equations is convenient to consider a harmonic plane wave solution in the form

$$\mathbf{U}(\mathbf{r}, t; \boldsymbol{\kappa}, \omega) = \mathbf{U}_0 \exp\left(\boldsymbol{\kappa} \cdot \mathbf{r} - i\omega t\right) \tag{3.2}$$

where $\mathbf{U}$ could be electric or magnetic field, $\mathbf{U}_0$ is the amplitude, ω is the angular frequency, $\boldsymbol{\kappa}$ is the wavevector, and $\mathbf{r}$ is the position of observation in the physical domain. The magnitude of the wavevector, or wavenumber κ, is associated with the speed of light, c_0, and ω, with the following relation:

$$|\boldsymbol{\kappa}| = \kappa = \frac{\omega}{c_0} = \frac{2\pi}{\lambda_0} \tag{3.3}$$

where λ_0 is the wavelength in free space.

The plane wave has a direction of propagation defined by $\boldsymbol{\kappa} = (\kappa_x, \kappa_y) = \kappa\,(\cos\theta, \sin\theta)$. Similarly, the Poynting vector, $\mathbf{S} = \mathbf{E} \times \mathbf{H}$, defines the direction of propagation, then

$\mathbf{E} \cdot \boldsymbol{\kappa} = \mathbf{H} \cdot \boldsymbol{\kappa} = 0$. Thus, a normalized plane wave, for electric field, can be defined with any of the two pairs $\{\kappa, \theta\}$, or $\{\kappa_x, \kappa_y\}$, as follow

$$\mathbf{E}_a(\mathbf{r}, t, \kappa, \theta) = \mathbf{E}_0(\theta) \exp(\boldsymbol{\kappa} \cdot \mathbf{r} - i\omega t) \tag{3.4}$$

where

$$\mathbf{E}_0(\theta) = (-\sin\theta, \cos\theta) = \frac{1}{\kappa}(-\kappa_y, \kappa_x)$$

This continuous plane wave solution has a discretized version, $\mathbf{e_a}$, which can be obtained from (2.17) and (3.4),

$$\mathbf{e_a} = \mathbf{M_{ee}^{-1}} \mathbf{e}^* \tag{3.5}$$

where the qth term of the vector $\mathbf{e}^*$ is defined as

$$e_q^* = \int_V \boldsymbol{\Phi}_q^{(M_E)} \cdot \mathbf{E}_0(\theta) \exp(\boldsymbol{\kappa} \cdot \mathbf{r})\, dV \tag{3.6}$$

The solution $\mathbf{e_a}$ is an approximated eigenvector for the eigenproblem (3.1). It is an approximation because the computational domain must be truncated, in this case with a periodic bundary condition, which allows a set of solutions, i.e., a finite number of plane wave solutions, and $\mathbf{e_a}$ is not necessarily part of this set. However, $\mathbf{e_a}$ can be associated with an approximated eigenvalue $\tilde{\chi}$ given by the Rayleigh quotient

$$\tilde{\chi} = \tilde{\kappa}^2 = \frac{\mathbf{e_a}^T \mathbf{Y} \mathbf{e_a}}{\mathbf{e_a}^T \mathbf{X} \mathbf{e_a}} \tag{3.7}$$

where $\mathbf{e_a}^T$ is the transpose of $\mathbf{e_a}$, and $\tilde{\kappa}$ represents the numerical wavenumber associated with $\mathbf{e_a}$ imposed in the numerical system, that means that the difference

between $\tilde{\kappa}(\kappa,\theta)$ and κ is the error associated with numerical dispersion. Ideally, in a numerical method without dispersion $\tilde{\kappa}(\kappa,\theta)$ is equal to κ for any θ.

In order to simplify the results and the discussion, both theoretical and numerical wavenumbers are normalized:

$$\Omega = \frac{\kappa L}{P \min(M_E, M_H)} \tag{3.8}$$

where L is the length of the physical domain, and P is the number of discretized elements in one direction, x or y. As an illustration, consider the ideal numerical dispersion, $\Omega^2_{ideal} = \Omega^2_x + \Omega^2_y$, shown in Figure (3.1); two features are important in these figures, the monotonic behavior and the concentric contourns of a correct numerical dispersion. Thus, non-monotonic behavior is associated with spurious solutions with negative group velocities, and anisotropic behavior. The normalized phase and group velocities are calculated from the normalized numerical dispersion, with the following expresions

$$\lambda_p = \frac{\Omega_n}{\Omega} \tag{3.9}$$

$$\lambda_g = \frac{d\Omega_n}{d\Omega} \tag{3.10}$$

Thus, considering again the ideal case, both normalized velocities must have values equal to one.

3.2.2 Semidiscrete analysis

The semidiscrete analysis (Tobón et al., 2011) is used here to obtain the analytical solution of the numerical dispersion for low order elements. This procedure also assumes a plane wave solution (3.2); then if the electric and magnetic fields are

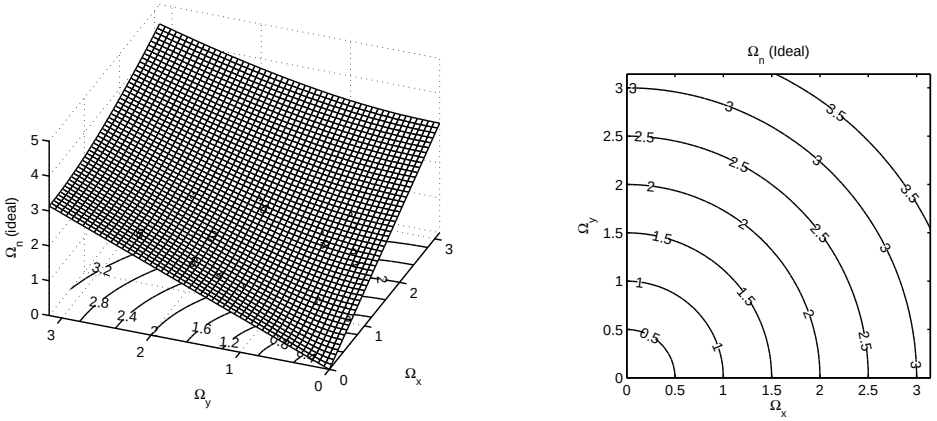

(a) (b)

FIGURE 3.1: Ideal numerical dispersion: (a) surface and (b) contourn

known in a position defined by a vector $\mathbf{r}_p$, the value of the fields can be solved in any position $\mathbf{r}_q = \mathbf{r}_p + \triangle\mathbf{r}$, given the following translation operation

$$\mathbf{U}_q = \mathbf{U}_p \exp\left(-j\boldsymbol{\kappa} \cdot \triangle\mathbf{r}\right) \tag{3.11}$$

Thus, if the same concept is applied to the weak forms of the Maxwell's equations, considering just a few elements, some unknowns are related by translation operators. Solving the determinant of the system to obtain a non-trivial solution, a close-form expressions is obtained.

For clarity we will first present the analysis in detail for the one-dimensional TEM_x case (both electric and magnetic fields are transverse to the x direction) for a source-free homogeneous medium, and subsequently consider the extension to higher dimensions. Under these considerations equations (2.1) and (2.2) take the following forms:

$$\epsilon\frac{\partial E_y}{\partial t} + \frac{\partial H_z}{\partial x} = 0 \tag{3.12}$$

$$\mu \frac{\partial H_z}{\partial t} + \frac{\partial E_y}{\partial x} = 0 \tag{3.13}$$

For this analysis, we seek periodic solutions of (3.12) and (3.13) of the form:

$$\left\{ \begin{array}{c} E_y(x,t) \\ H_z(x,t) \end{array} \right\} = \left\{ \begin{array}{c} E_y(x) \\ H_z(x) \end{array} \right\} e^{j\omega t} \tag{3.14}$$

Equations (3.12) and (3.13) can be rewritten as

$$j\epsilon\omega E_y + \frac{dH_z}{dx} = 0 \tag{3.15}$$

$$j\mu\omega H_z + \frac{dE_y}{dx} = 0 \tag{3.16}$$

Let $\phi_p \equiv \phi_p(x)$, $p = 1, \cdots, n_e$, and $\psi_q \equiv \psi_q(x)$, $q = 1, \cdots, n_h$, be piecewise-polynomial finite element basis functions. Then, for any solution we have the expansions:

$$E_y(x) = \sum_{p=1}^{n_e} E_p \phi_p^{(M)}(x); \qquad H_z(x) = \sum_{q=1}^{n_h} H_q \psi_q^{(N)}(x) \tag{3.17}$$

where Lagrange-type bases are assumed, and E_p and H_p are nodal degrees-of-freedom for the problem with $E_p = E_y(x_p)$, and $H_p = H_z(x_p)$ for specified node p, at point x_p, in a uniform mesh of P elements in the physical domain with length L, and the element size is defined as $d = \frac{L}{P}$.

Using the appropriate basis functions, ϕ_q and ψ_p, as test functions and substituting the expansions (3.17) into (3.15) and (3.16) to determine the semi-discrete weak system:

$$j\omega \sum_{p=1}^{n_e} E_p \int_0^L \epsilon \phi_q^{(M)} \phi_p^{(M)} dx + \sum_{p=1}^{n_h} H_p \int_0^L \phi_q^{(M)} \frac{d\psi_p^{(N)}}{dx} dx = 0 \tag{3.18}$$

$$\sum_{p=1}^{n_e} E_p \int_0^L \psi_q^{(N)} \frac{d\phi_p^{(M)}}{dx} dx + j\omega \sum_{p=1}^{n_h} H_p \int_0^L \mu \psi_q^{(N)} \psi_p^{(N)} dx = 0 \tag{3.19}$$

Now, for the dispersion analysis, the dependent variables in wave vector space are decomposed as follows

$$\left\{ \begin{array}{c} E_q \\ H_q \end{array} \right\} = \left\{ \begin{array}{c} E_p \\ H_p \end{array} \right\} e^{jkx_{qp}} \tag{3.20}$$

As an example, considering a linear common interpolation in a uniform mesh, and first order functions in both E and H, we have

$$\sum_{q=1}^{M} E_q \int_0^L \phi_p^{(1)} \phi_q^{(1)} dx = E_p e^{jkx_{qp}} \frac{d}{3} \left(\cos\left(\Omega_R\right) + 2\right) \tag{3.21}$$

$$\sum_{q=1}^{N} H_q \int_0^L \phi_p^{(1)} \frac{d\psi_q^{(1)}}{dx} dx = H_p e^{jkx_{qp}} j \sin\left(\Omega_R\right) \tag{3.22}$$

Similarly, we can obtain results for all terms. Then, based on those formulations we can obtain the matrix equation

$$\left[\begin{array}{cc} \frac{\omega\epsilon d}{3} \left(\cos\left(\Omega_R\right) + 2\right) & \sin\left(\Omega_R\right) \\ \sin\left(\Omega_R\right) & \frac{\omega\mu d}{3} \left(\cos\left(\Omega_R\right) + 2\right) \end{array} \right] \left[\begin{array}{c} E \\ H \end{array} \right] = \left[\begin{array}{c} 0 \\ 0 \end{array} \right] \tag{3.23}$$

The normalized numerical wavenumber can be obtained from the non-trivial solution of the equation (3.23)

$$\Omega_{n,E1H1}^{1D} = \frac{3\sin\left(\Omega_R\right)}{\cos\left(\Omega_R\right)+2} \tag{3.24}$$

for the linear interpolation basis functions ($M = N = 1$).

The same procedure can be used to obtain the numerical dispersion for the mixed-order basis functions. In particular, if the second-order basis function ($M = 2$) is used for electric field, and the first-order basis function ($M = 1$) is used for magnetic field, the expression for the dispersion relation is:

$$\Omega_{n,E2H1}^{1D} = \sqrt{\frac{5\left(3-\cos\left(\Omega_R\right)\right)\left(1-\cos\left(\Omega_R\right)\right)+\sin^2\left(\Omega_R\right)}{\left(3-\cos\left(\Omega_R\right)\right)\left(2+\cos\left(\Omega_R\right)\right)}} \tag{3.25}$$

Extending this method to two dimensions, we obtained the following expressions:

$$\Omega_{n,E1H1}^{2D} = \sqrt{\frac{27}{2}}\left[\sum_{\alpha,\beta=x,y}\frac{\sin^2\Omega_\alpha\left(1+\cos\Omega_\beta\right)}{\left(2+\cos\Omega_\alpha\right)^2\left(2+\cos\Omega_\beta\right)}\right]^{1/2} \tag{3.26}$$

$$\Omega_{n,E1H2}^{2D} = \sqrt{\frac{25}{3}}\left[\sum_{\alpha,\beta=x,y}\frac{\sin\frac{\Omega_\alpha}{2}\left(4+\cos\frac{\Omega_\beta}{2}\right)\left(\sin\Omega_\alpha+4\sin\frac{\Omega_\alpha}{2}\right)}{\left(2+\cos\Omega_\alpha\right)\left[\left(2+\cos\frac{\Omega_\alpha}{2}\right)\left(2+\cos\frac{\Omega_\beta}{2}\right)+12\right]}\right]^{1/2} \tag{3.27}$$

3.3 Numerical Results

3.3.1 Spurious solutions in a periodic one-dimensional domain

The first case of this chapter is a one-dimensional domain with length $L = 1$ m, and a periodic uniform mesh with $P = 100$ elements. Table 3.1 shows a comparison between the exact wavenumber and numerical wavenumber in (3.1) using E1H1 and E2H1 schemes. There are low frequency spurious solutions (such as Mode 2 in E1H1 scheme and Mode 1 in E2H1 scheme) in both numerical schemes due to the non-divergence-conforming basis functions used in both schemes; such spurious modes are

Table 3.1: Eigenvalues for the 1D-PBC case calculated by the analytical method, the E1H1 scheme, and the E2H1 scheme. High-frequency spurious modes are denoted with parentheses.

Analytical	Mode E1H1	Numerical E1H1	Mode E2H1	Numerical E2H1
···	2	0.00000125	1	0.00000441
6.28318531	4	6.28318476	3	6.28318646
12.56637061	6	12.56635317	5	12.56640743
···	8	(18.80005824)	···	···
18.84955592	10	18.84942316	7	18.84983387
25.13274123	12	25.13217993	9	25.13390293
31.41592654	14	31.41420634	11	31.41943484
···	16	(37.30580267)	···	···

in general of little concern in practice and they are well understood. However, at high frequencies, interspersed spurious eigenvalues are presented in the E1H1 scheme and are shown in parentheses, while the E2H1 scheme is free of high-frequency spurious modes. For the correct eigenvalues in both schemes, similar accuracy in the numerical wavenumber is obtained; thus, it is difficult to know whether a particular solution is a spurious mode in a complex case when no analytical solutions are available. Therefore, it is an important goal for this study to identify which scheme will give non-spurious solutions. Figure 3.2 presents the eight eigenvectors corresponding to the eigenvalues in Table 1 from the E1H1 scheme. We observe the fast spatially varying patterns in both the zero-frequency (1st panel) and high-frequency (4th and 8th panels) spurious modes.

The presence of spurious waves is notorious in time domain as they introduce rapid spatial variations in the field solutions. To demonstrate this, we study a pulse of the first-order Blackman-Harris window function (Liu, 1997) with a characteristic frequency $f_c = 3$ GHz. The first three plots in Figures 3.3(a) - 3.3(c) show how the correct wave (a first-derivative of the Blackman-Harris Window pulse) and the

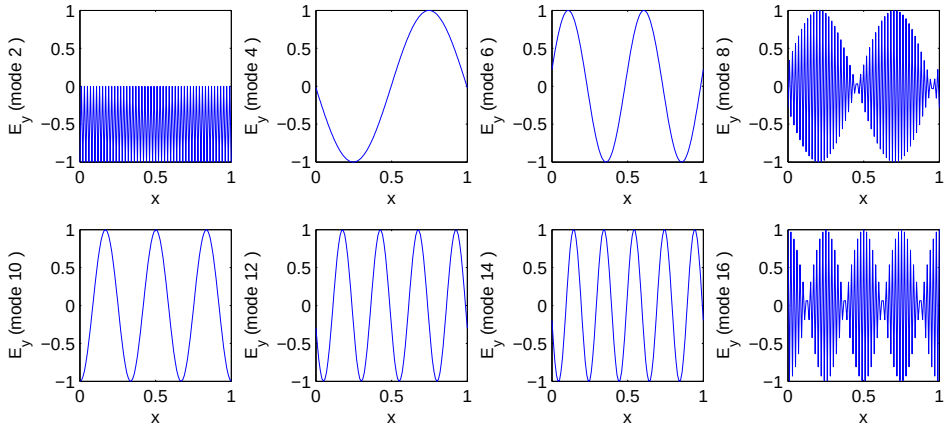

FIGURE 3.2: Eigenvectors corresponding to the eight eigenvalues in Table 1 in the 1D periodic case using the E1H1 scheme. The first panel shows the zero-frequency spurious mode, while the 4th and 8th panels show the high-frequency spurious modes.

spurious waves move along the axis of propagation in this 1D problem. These figures are snapshots at three different times (0.25, 0.50, and 0.75 ns), and show a spurious wave faster than the correct one. This spurious wave is characterized by a rapid variation in space, i.e. a high wavenumber, in agreement with the dispersion analysis. However, it is evident that this spurious wave has a slow variation in the time response, as shown in Figure 3.3(d), which hinders the detection of such non-physical solutions from correct signals taken by receivers located at a single point in space. Therefore, in practice, it is important to use basis functions that are free of spurious solutions, such as the EmHn scheme with $m = n \pm 1$ or in general (but less favorable) with $m \neq n$ with $|m - n| \geq 2$.

3.3.2 Spurious solutions in a three-dimensional PEC cavity

Here, a simple 3D case is further presented to show the presence of spurious solutions when the same order of interpolation in **E** and **H** is used; these basis functions are the edge-based vector basis functions, i.e., the Nedlec edge elements. The case under study is a perfect electric conductor cavity (0.23 m $\times$ 0.11 m $\times$ 0.03 m) with a

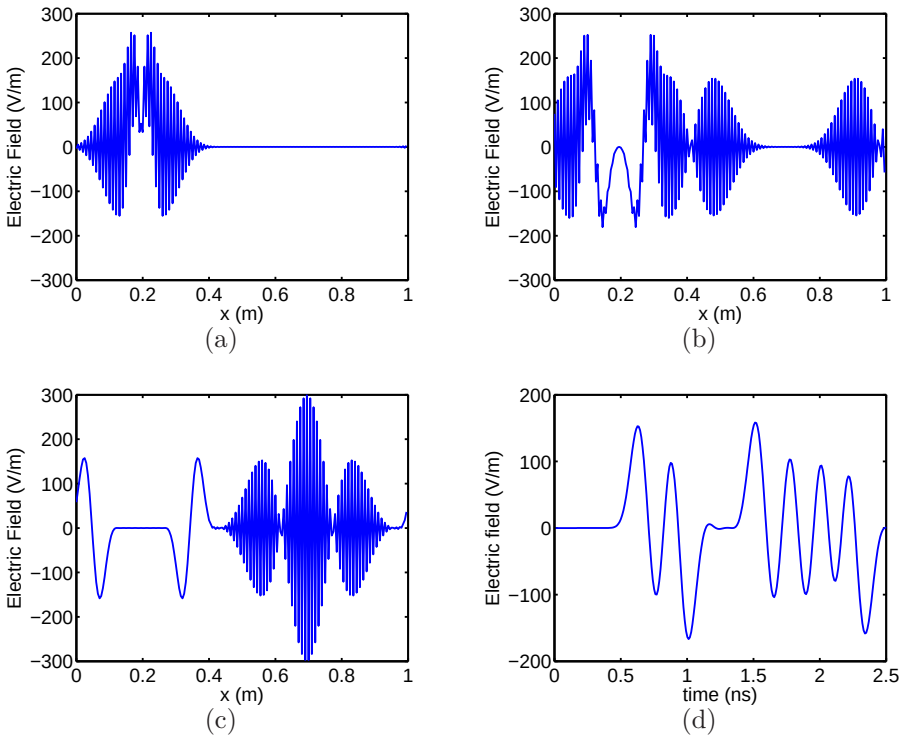

FIGURE 3.3: (a)-(c) Snapshots of real and spurious solutions using second order in both E and H (E2H2 scheme) at 0.25, 0.50, and 0.75 ns, respectively, and (d) time response at $x = 0.8m$, for the 1D periodic problem.

dipole source located at (0.01, 0.01, 0.003) m, with polarization in the direction $(\hat{x} + \hat{y} + \hat{z})/\sqrt{3}$, and a receiver located at (0.20, 0.07, 0.013) m. A first-derivative of the Blackman-Harris Window with characteristic frequency 2.0 GHz was used as the source time function. The mesh (Figure 3.4) is formed by brick elements with size (0.01, 0.01, 0.01) m.

Figure 3.5(a) shows the correct eigenvalues using E1H2, and while in Figure 3.5(b) a large number of spurious eigenvalues are present with the E1H1 scheme. The eigenvectors corresponding to the first four correct eigenvalues are on the top of Figure 3.6, and eigenvectors with closest eigenvalue but from E1H1 solutions on the bottom. We can notice similar behaviors as those observed in one dimension, with fast spatial variations in the spurious solutions. The time domain solution is

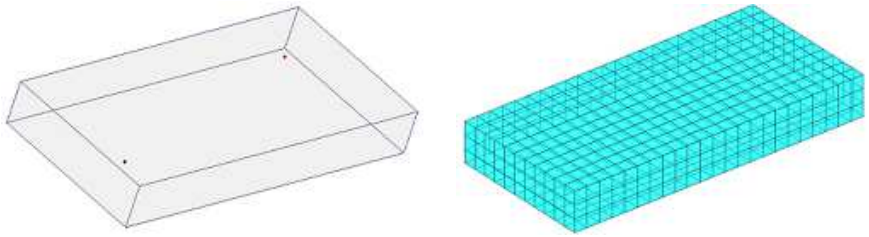

(a) (b)

FIGURE 3.4: A PEC cavity of dimensions 0.23 m x 0.11 m x 0.03 m centered at the origin with a source and receiver. (a) Geometry. (b) Mesh.

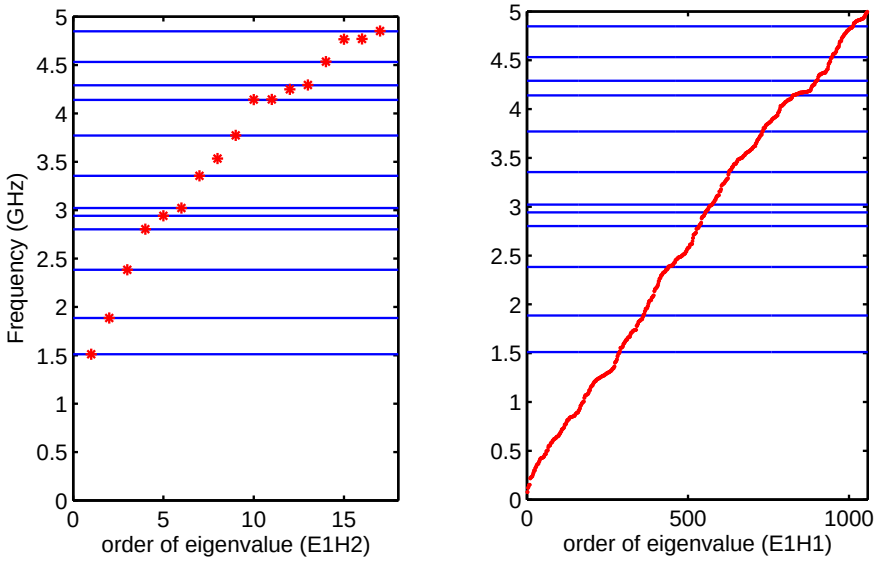

(a) (b)

FIGURE 3.5: Eigenvalues of the 3D problem in Figure 3.4. (a) Correct values using the E1H2 scheme. (b) Non-physical, spurious values using the E1H1 scheme.

presented in Figure 3.7, with a spurious solution in dashed line produced by the E1H1 scheme, but a correct one (verified by commercial software) when the E1H2 scheme is used. The presence of spurious solutions is also evident in the spectrum (dotted line) in Figure 3.7. A good agreement in both time and frequency domains is obtained in the E1H2 scheme.

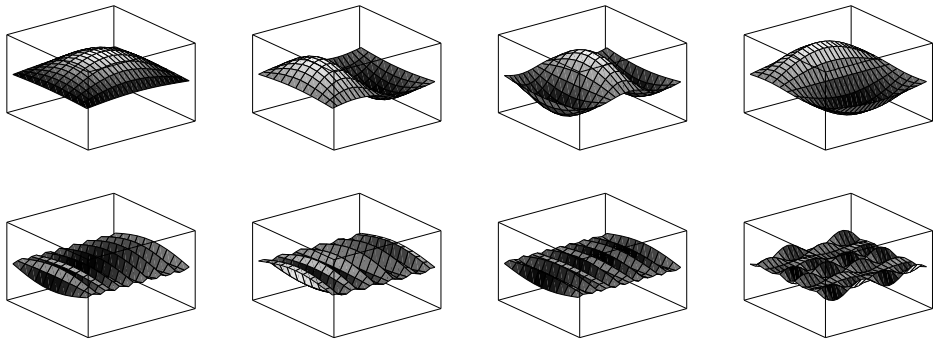

FIGURE 3.6: Eigenvectors of the 3D problem in Figure 3.4 for first four modes on the plane $z = 0.01$. Top: Correct solutions obtained using the E1H2 scheme. Bottom: Spurious solutions with the closest frequencies to those above using the E1H1 scheme.

3.3.3 Numerical dispersion in a periodic one-dimensional domain

Next, it is shown the modal analysis and semidiscrete analysis applied to the E1H1 and E1H2 schemes in a periodic one-dimensional domain; in addition, a reference dispersion curve from Walters and Carey is presented (Walters and Carey, 1983). First, we note an excellent agreement between modal analysis results and the semi-

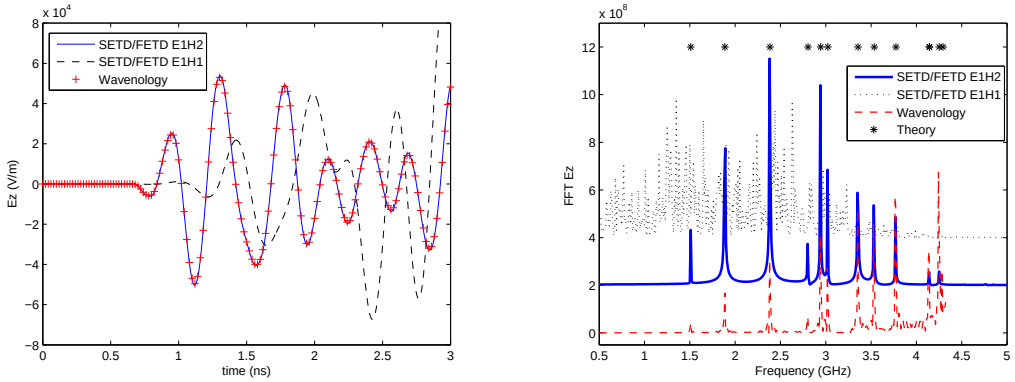

(a) (b)

FIGURE 3.7: E_z signals at the receiver in the 3D problem in Figure 3.4 obtained using the E1H1 and E1H2 schemes and their comparison with results from commercial software Wavenology. (a) Time domain signals up to 3 ns (later signals are truncated for clarity). (b) Spectrum magnitude of the signals, where the E1H1 and E1H2 results are shifted up by 2×10^{-8} and 4×10^{-8}, respectively for clarity. Theoretical values of the resonance frequencies are also marked.

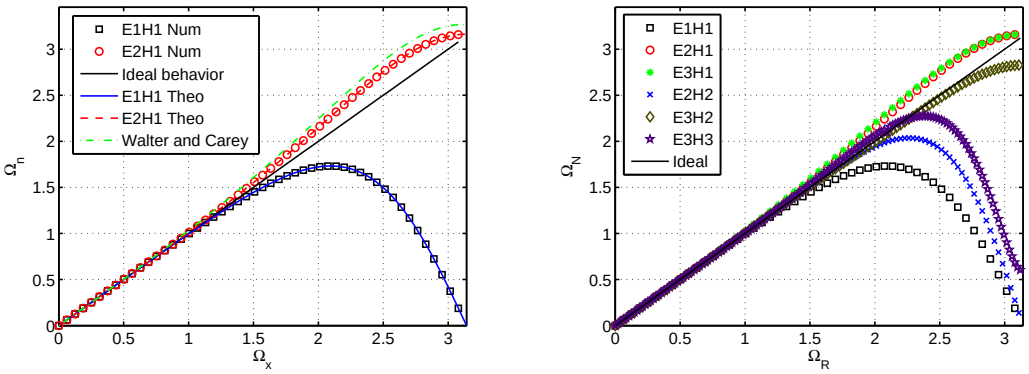

FIGURE 3.8: Dispersion curves for various schemes for the 1D periodic problem. (a) Comparison of the analytical dispersion solution and numerical dispersion solution for E1H1 and E2H1, together with the exact dispersion relation and the result from Walters and Carey (Walters and Carey, 1983). (b) Dispersion curves for higher order schemes.

discrete analysis results for both schemes E1H1 and E1H2 in Figure 3.8(a), and the Walters-Carey expression (Walters and Carey, 1983). Secondly, double solutions are present in the E1H1 scheme, i.e., with one given numerical wavenumber, there exist two different real values of wavenumbers; these solutions correspond to one correct and one spurious solutions, respectively. Furthermore, we can note a monotonic behavior of the E1H2 scheme, i.e., it is a scheme free of spurious solutions. Similarly, results for higher order schemes are presented in Figure 3.8(b); the results present the same conclusion: The spurious modes are present when the same order of interpolation is used in **E** and **H** (i.e., E1H1, E2H2, and E3H3 schemes), while the schemes with different orders of interpolation for **E** and **H** (i.e., E2H1, E3H1, E3H2 schemes) are free of spurious solutions.

3.3.4 Numerical dispersion in a periodic two-dimensional domain

Figure (3.9) shows the normalized numerical dispersion for $M_E = 1$ and $M_H = 1$, and its error respect to the analytical solution (3.26) obtained by the semidiscrete analysis. The error is below 0.05% for all surface, and the maximum values are in

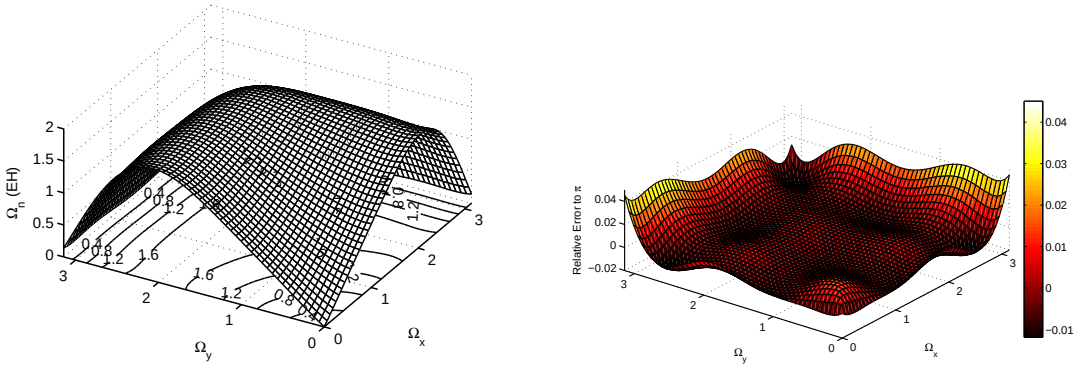

(a) (b)

FIGURE 3.9: (a) The normalized numerical dispersion for $M_E = 1$ and $M_H = 1$, and (b) its error respect to analytical solution

the Nyquist limit($\Omega = \pi$). Similar error is obtained for the normalized numerical dispersion for $M_E = 1$ and $M_H = 2$ (see Figure (3.10)), respect to the analytical expression (3.27). From these Figures, we can also note that if same order ($M_E = M_H = 1$) of interpolation for electric and magnetic fields are used, the numerical dispersion is non-monotonic, i.e., the numerical method produces spurious modes with negative group velocities. On the other hand, if different order of interpolation is used ($M_E = 1$ and $M_H = 2$), the numerical dispersion is monotonic, i.e., the numerical scheme is free of spurious solutions.

Similar conclusion arises from Figure (3.11), where contours of numerical dispersion are plotted. Schemes with same order of interpolation are on the left column, $M_E = M_H = 1, 2$, different order of interpolation on the right column, $M_H = M_E + 1$. We can note the non-monotonic behavior on the left schemes ($M_H = M_E$), and negative slopes for $\Omega \gtrsim 2$. Contours on the right are monotonic with an increment of the anisotropic behavior when higher orders of interpolations are employed.

In Figure (3.12) shows the normalized wavenumber for different angles of propagation. Figures on the left (same order of interpolation) shows a non-monotonic behavior in all angles, and negative slopes for higher values of the wavenumber; these

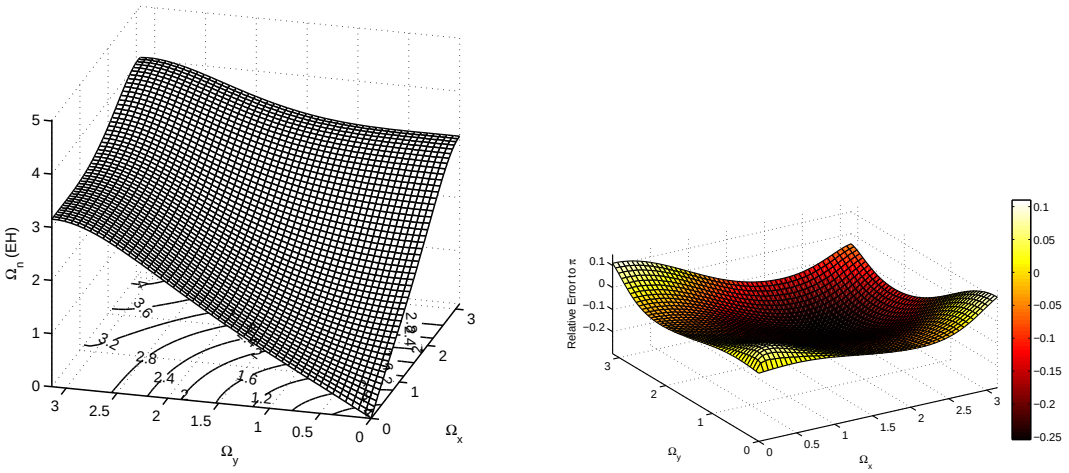

(a) (b)

FIGURE 3.10: (a) Normalized numerical dispersion for $M_E = 1$ and $M_H = 2$, and (b) its error respect to analytical solution

negative slopes increase with the order of interpolation. In contrast, on the right column monotonic dispersion curves are clear for all angles. These curves show different behavior for different angles, for example in 30 the dispersion curve is close to the ideal case for all orders of interpolation, but in 45, for $\Omega \gtrsim 2.5$, the curve is going down with an increment in the order of interpolation.

The phase velocities calculated from the dispersion curves with the expression (3.9) are presented in Figure (3.13). Again, figures on the left have same order of interpolation with $M_E = M_H = 1, 2$, and figures on the right have different order $M_H = M_E + 1$, with $M_E = 1, 2$. Schemes with same order of interpolation present a decreasing phase velocity when the wavenumber increases, that means that plane waves with large wavelength have speed close to the speed of light, but for short wavelength the wave is close to be stationary. These contours also show a "well-behaved" dispersive region (a normalized phase velocity close to one) that increase with the order of interpolation. On the contrary, figures on the right show phase velocities close to one in the entire wavenumber space, showing fast waves in x and

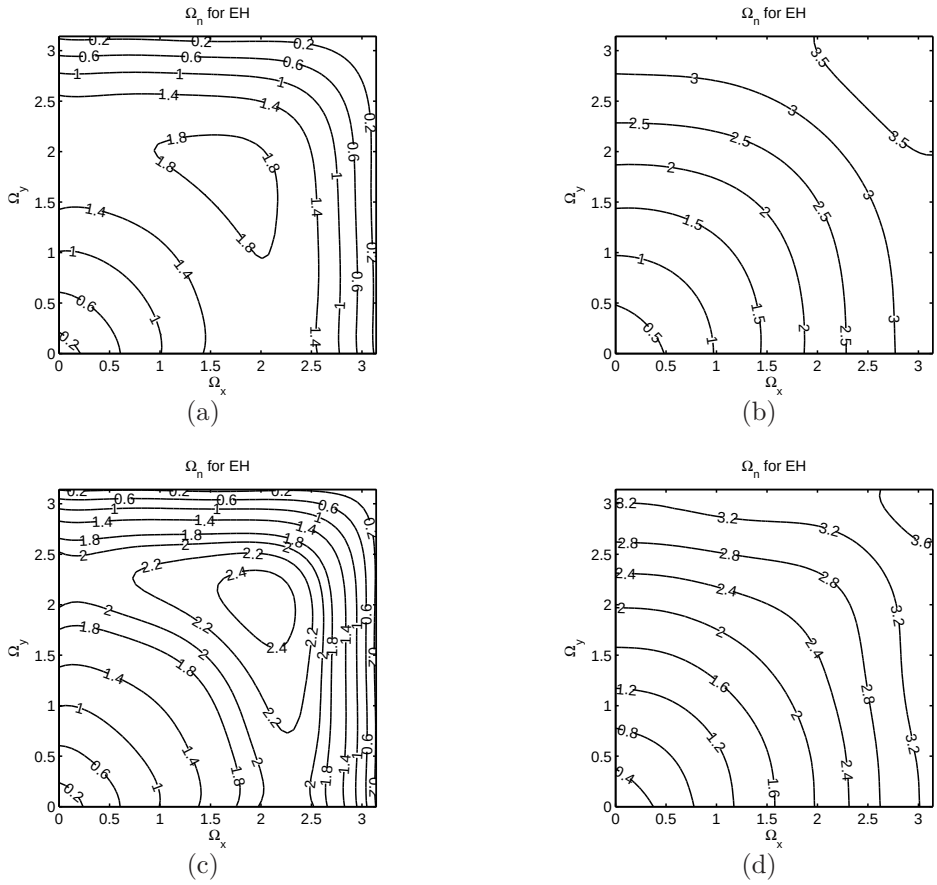

FIGURE 3.11: Contours of the normalized numerical dispersion for: (a) $M_E = M_H = 1$; (b) $M_E = 1$ and $M_H = 2$;(c) $M_E = M_H = 2$; (d) $M_E = 2$ and $M_H = 3$

y directions for very short and very large wavenumbers.

The group velocities are shown in Figure (3.14), where dashed lines mean negative values. Schemes with same order of interpolation have negative group velocities for large wavenumbers (small values of wavelength); this behavior is typical of spurious solutions, which have rapid change in the space but slow variations in time. Schemes with different order of interpolation have all positive group velocities with a reduction close to zero in the Nyquist limit ($\Omega_x = \Omega_y = \pi$). Anisotropic behavior of high order elements must be studied in future investigations.

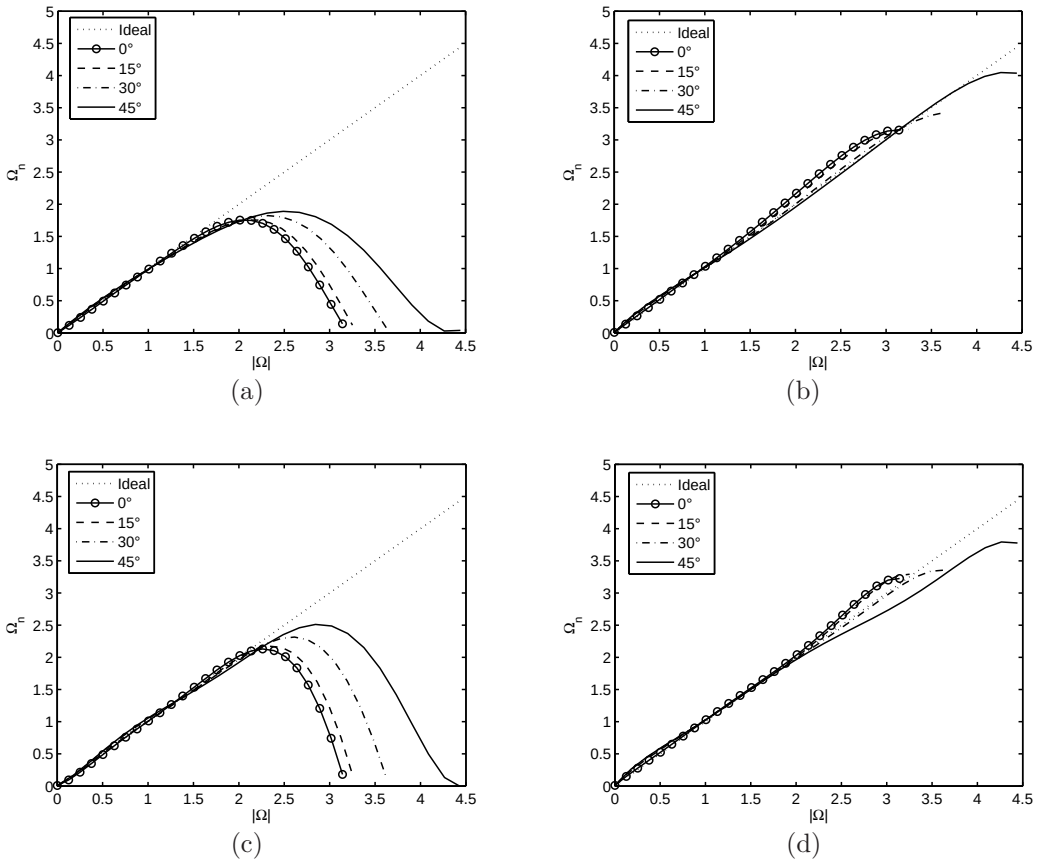

FIGURE 3.12: Plots of the normalized numerical dispersion for different angles (0, 15, 30, and 45): (a) $M_E = M_H = 1$; (b) $M_E = 1$ and $M_H = 2$;(c) $M_E = M_H = 2$; (d) $M_E = 2$ and $M_H = 3$

3.3.5 Numerical dispersion based on the Hodge operator

In this analysis, we consider four vectors similar to (3.2) which represent ideal electric and magnetic plane waves, with $\tilde{\mathbf{v}} = \tilde{\mathbf{e}}, \tilde{\mathbf{h}}, \tilde{\mathbf{d}}, \tilde{\mathbf{b}}$. Then, from ideal field intensities plane waves ($\tilde{\mathbf{e}}$ and $\tilde{\mathbf{h}}$), the Hodge operators (2.39) and (2.40) could be used to calculate the numerical flux densities ($\hat{\mathbf{d}}$ and $\hat{\mathbf{b}}$, respectively), as follows

$$\hat{\mathbf{e}} = \star_{1/\epsilon}\tilde{\mathbf{d}} \text{ and } \hat{\mathbf{h}} = \star_{1/\mu}\tilde{\mathbf{b}} \tag{3.28}$$

This numerical dispersed plane waves are attenuated and dephased respect to the ideal ones, and from them a numerical relative permittivity and permeability can be

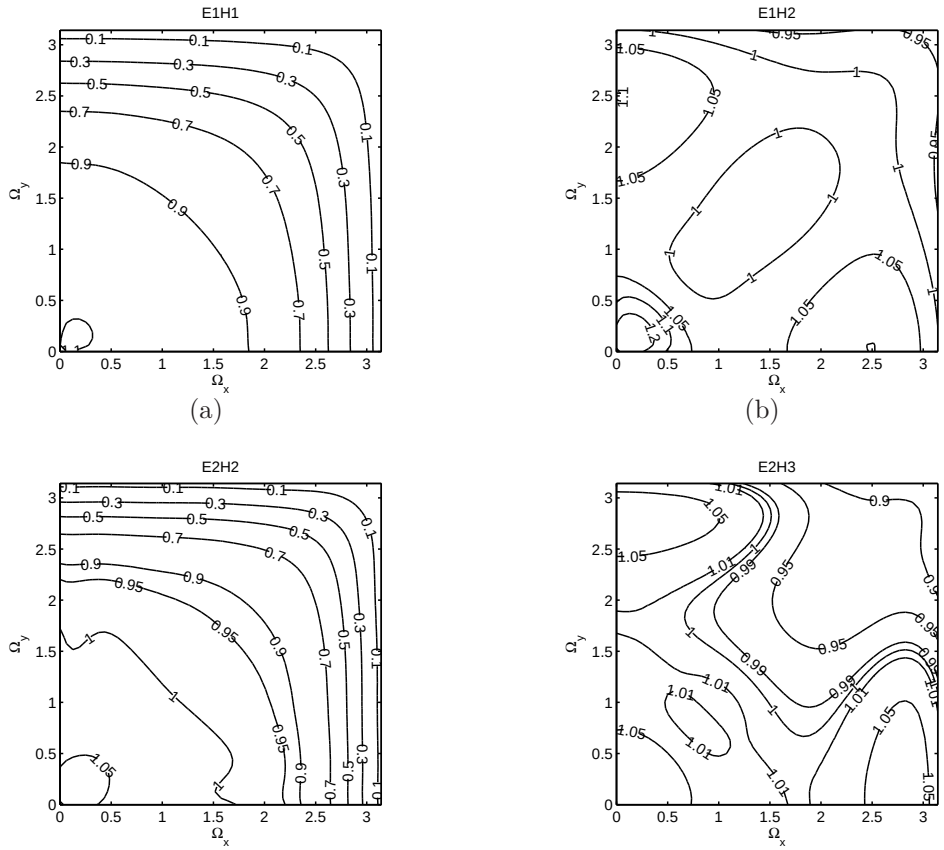

FIGURE 3.13: Plots of the normalized phase velocities for: (a) $M_E = M_H = 1$; (b) $M_E = 1$ and $M_H = 2$;(c) $M_E = M_H = 2$; (d) $M_E = 2$ and $M_H = 3$

extracted:

$$\frac{1}{\epsilon_n} = \frac{\tilde{\mathbf{e}}^* \cdot \hat{\mathbf{e}}}{\tilde{\mathbf{e}}^* \cdot \tilde{\mathbf{e}}} \tag{3.29}$$

$$\frac{1}{\mu_n} = \frac{\tilde{\mathbf{h}}^* \cdot \hat{\mathbf{h}}}{\tilde{\mathbf{h}}^* \cdot \tilde{\mathbf{h}}} \tag{3.30}$$

With these numerical values a new normalized phase velocity is calculated:

$$\lambda_{Hodge} = \sqrt{\frac{1}{\epsilon_n} \cdot \frac{1}{\mu_n}} \tag{3.31}$$

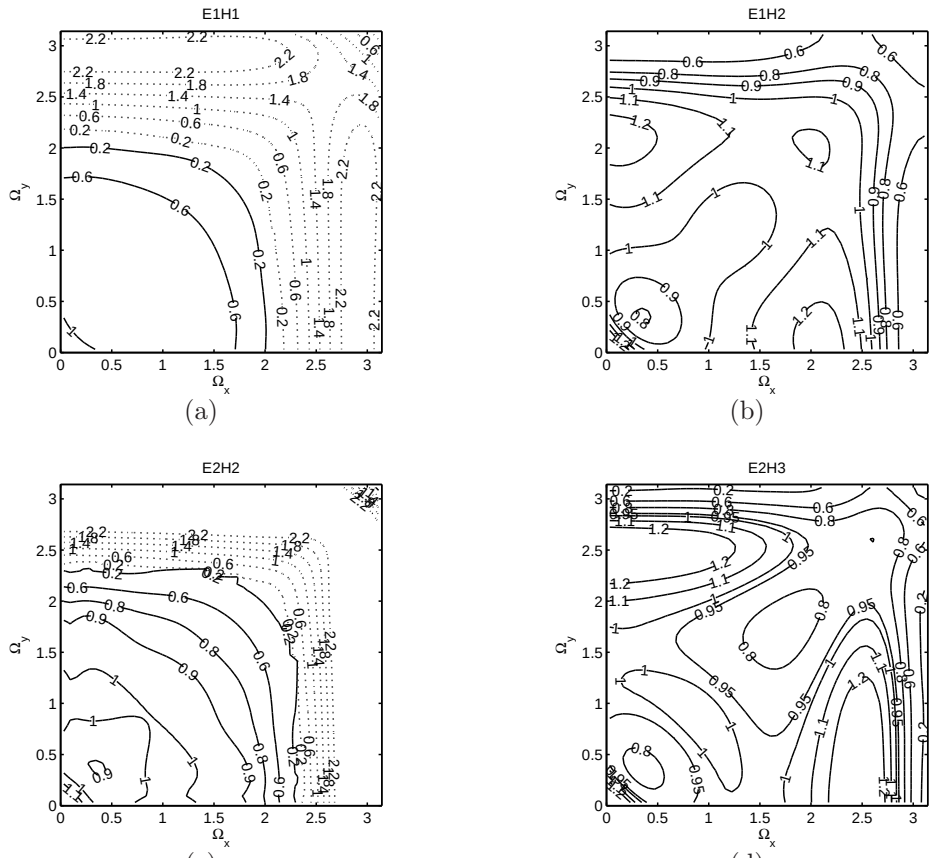

(a) (b) (c) (d)

FIGURE 3.14: Plots of the normalized group velocities (dashed lines mean negative values) for: (a) $M_E = M_H = 1$; (b) $M_E = 1$ and $M_H = 2$;(c) $M_E = M_H = 2$; (d) $M_E = 2$ and $M_H = 3$

Table 3.2: Cases for the Hodge operator analysis

Case	M_E	M_H	M_D	M_B	Figure
1	1	1	1	1	3.15
2	1	2	2	1	3.16
3	2	2	2	2	3.18
4	2	3	3	2	3.19

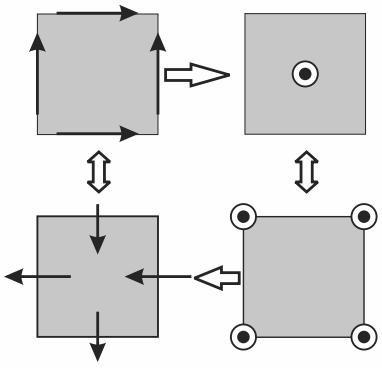

FIGURE 3.15: Schematic De Rham diagram for case 1. Horizontal arrows represent differential operators, and vertical arrows represent Hodge operators.

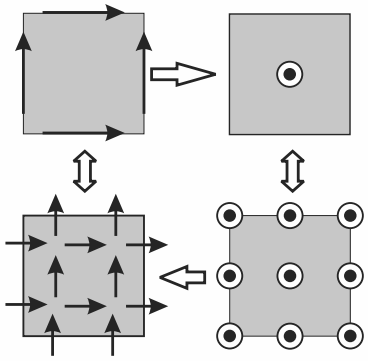

FIGURE 3.16: Schematic De Rham diagram for case 2. Horizontal arrows represent differential operators, and vertical arrows represent Hodge operators.

The schemes analyzed in this section are summarized in Table (3.2). An ideal numerical method must have a numerical phase velocity equal to the speed of light in all directions. Figures (3.17) and (3.20) show normalized phase velocity for EH schemes and dispersive Hodge operators. In particular, cases 1 based on EH formulation and Hodge operators is presented in Figures (3.17a) and (3.17c); in these contours, waves with large wavenumber have very low phase velocity, being zero in the Nyquist limit (i.e., $\Omega=\pi$). In contrast, case 2 shows normalized phase velocities with values close to one in both methods, as we can see in Figures (3.17b) and (3.17d).

Figure (3.20) shows the contours of phase velocity for case 3 and 4, from both methods. Similar to case 1, case 3 has velocity equals zero in the Nyquist limit,

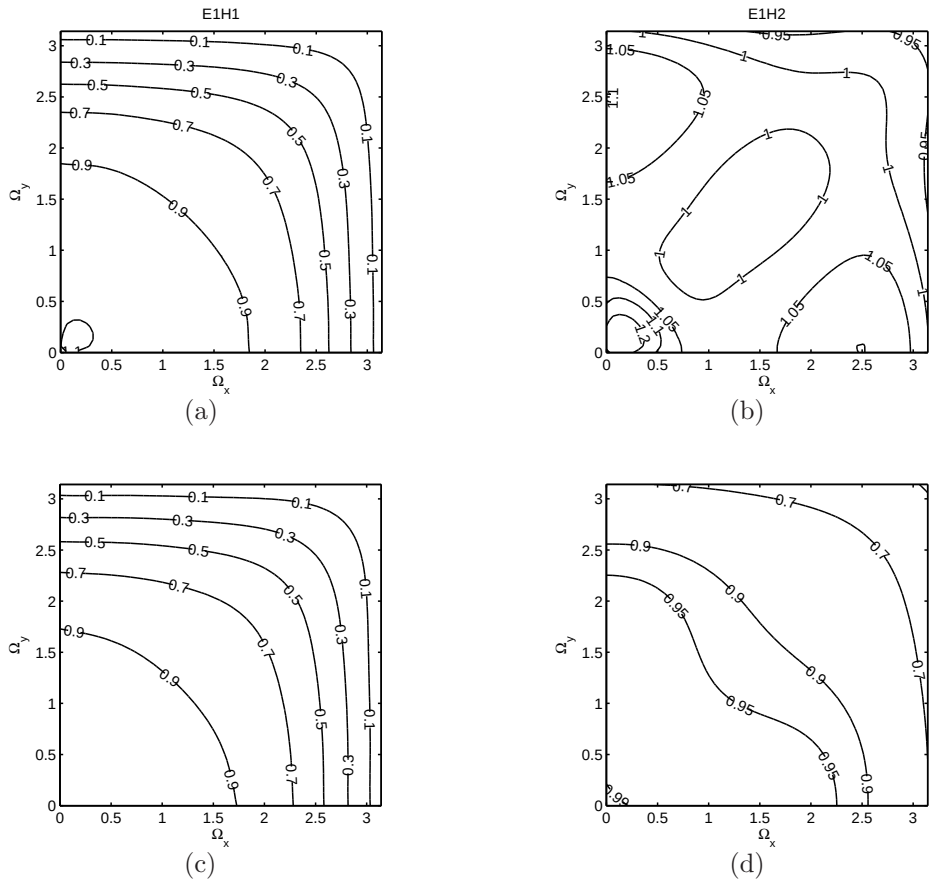

FIGURE 3.17: Contour of normalized phase velocities for: (a) EH formulation in case 1; (b) EH formulation in case 2; (c) Hodge operator in case 1; and (d) Hodge operator in case 2.

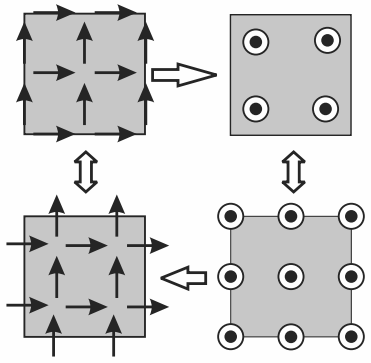

FIGURE 3.18: Schematic De Rham diagram for case 3. Horizontal arrows represent differential operators, and vertical arrows represent Hodge operators.

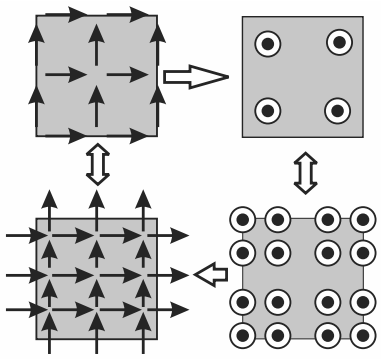

FIGURE 3.19: Schematic De Rham diagram for case 4. Horizontal arrows represent differential operators, and vertical arrows represent Hodge operators.

which is a clear inconvenient behavior for waves with short wavelength. Analogously, case 4 and case 2 have similar behavior. Normalized speeds are close to one in the whole wavenumber space. These results show that both methods used here to obtain numerical dispersion (i.e., modal analysis and the dispersive Hodge operator) give same fundamental results.

3.3.6 Analysis of solutions using tetrahedral elements

In this section, a three dimensional cavity with dimensions 10 mm $\times$ 7.5 mm $\times$ 5 mm is discretized with tetrahedral elements. The family of basis functions used here are described in the previous chapter, and can be found in (2.53) to (2.58); Figure 3.21 shows the De Rham diagram for these basis functions. Eigensolutions are obtained from (3.1), and transient solutions are solved from: (i) EH system of ordinary differential equations (2.23) and (2.24); and (ii) EB system of equations (2.30) and (2.31).

E2B2 (Lt/Qn for E field and Ln/Qt for B) shows the best performance in eigenvalue analysis, with error two orders of magnitude smaller than based on E1H2, E1B1 and Hodge, as we can see in Figures (3.22a) and (3.22b), for the first and second modes, respectively. Furthermore, E2B2 has a higher order of accuracy. Also,

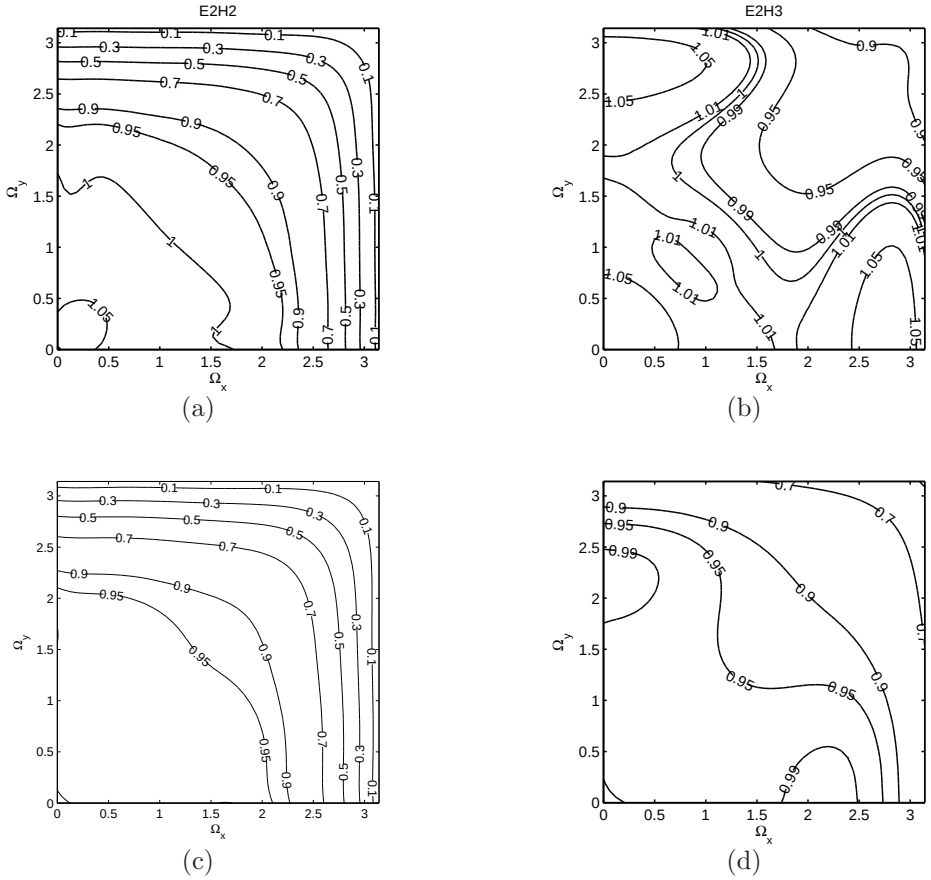

FIGURE 3.20: Contourn of normalized phase velocities for: (a) EH formulation in case 3; (b) EH formulation in case 4; (c) Hodge operator in case 3; and (d) Hodge operator in case 4.

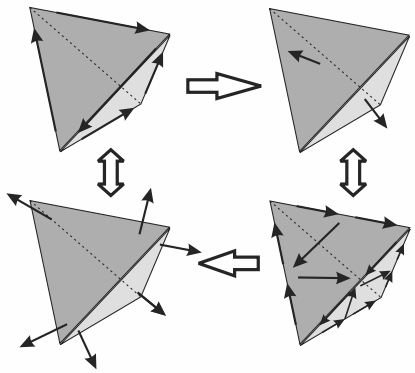

FIGURE 3.21: Schematic De Rham diagram for tetrahedral elements. Horizontal arrows represent differential operators, and vertical arrows represent Hodge operators.

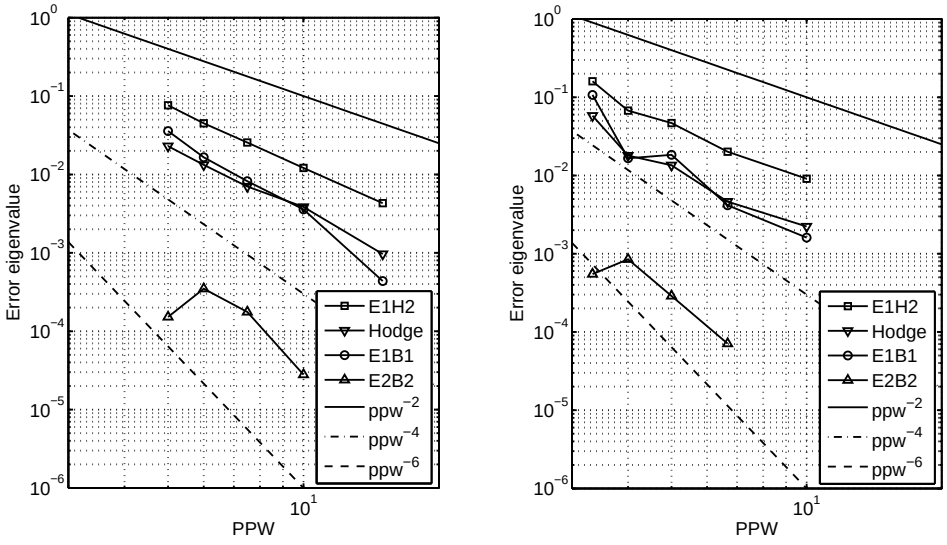

FIGURE 3.22: Error of eigenvalues vs. points per wavelength in cavity discretized with tetrahedra: (a) first mode ($\mathbf{TE}_{110}$), and (b) second mode ($\mathbf{TE}_{101}$).

E1B1 and Hodge operator have similar performance, then these two methods are equivalents. However, formulation E1H2 has the poorest performance in accuracy and order of convergence.

In efficiency, E2B2 has also the best performance respect to E1H2 and E1B1 as Figure (3.23). For the same error, E1H2 requires 10 times more unknowns than E1B1, and similarly, E1B1 requires 10 times more unknowns than E2B2. For a given number of unknowns, E2B2 formulation is one and two orders of magnitude more precise than E1B1 and E1H2 formulations, respectively.

Eigenvector analysis shows similar results as eigenvalue results: E2B2 is the most precise and efficient formulation. Figures (3.24a) and (3.24b) show field error from eigenvector analysis as a function of the mesh density (points per wavelenght) for E1B1 (exactly the same error for E1H1 and Hodge formuations) and E2B2. In these figures we can see that the order of convergence of E2B2 is between 2 and 3, higher than E1B1 convergence rate. Similar results are shown in Figures (3.25a) and (3.25b),

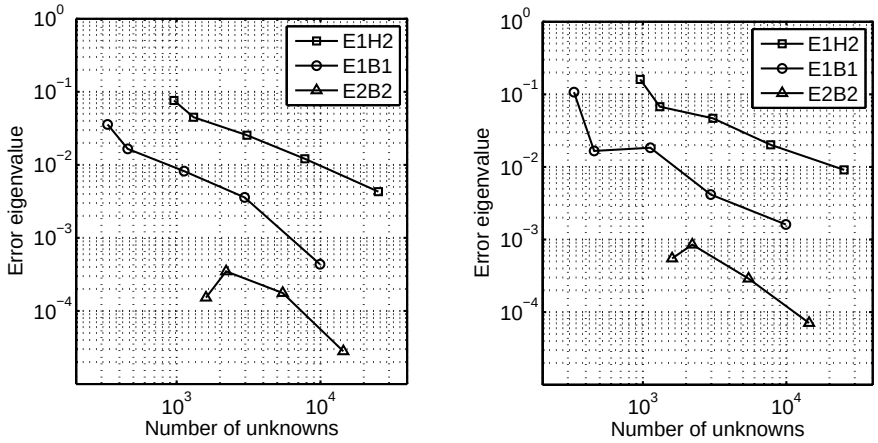

FIGURE 3.23: Error in eigenvalues vs. number of unknowns in cavity discretized with tetrahedra: (a) first mode ($\mathbf{TE}_{110}$), and (b) second mode ($\mathbf{TE}_{101}$).

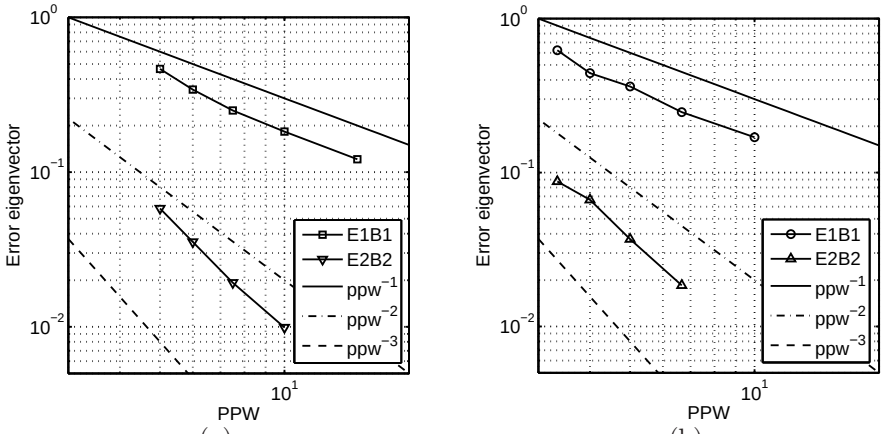

FIGURE 3.24: Error in eigenvectors in cavity discretized with tetrahedra: (a) first mode ($\mathbf{TE}_{110}$), and (b) second mode ($\mathbf{TE}_{101}$).

in these cases respect different number of unknowns. Again, a highly efficient E2B2 is clearly presented. E1B1 and E1H2 require a large number of unknowns to obtain the same E2B2 error in eigenvector (field accuracy).

Finally, a transient solution validates in the time domain the good performance of E2B2 respect to E1H2 and E1B1. The electric fields in x, y and z directions are received in a corner of the cavity; the source is located in the opposite corner of the

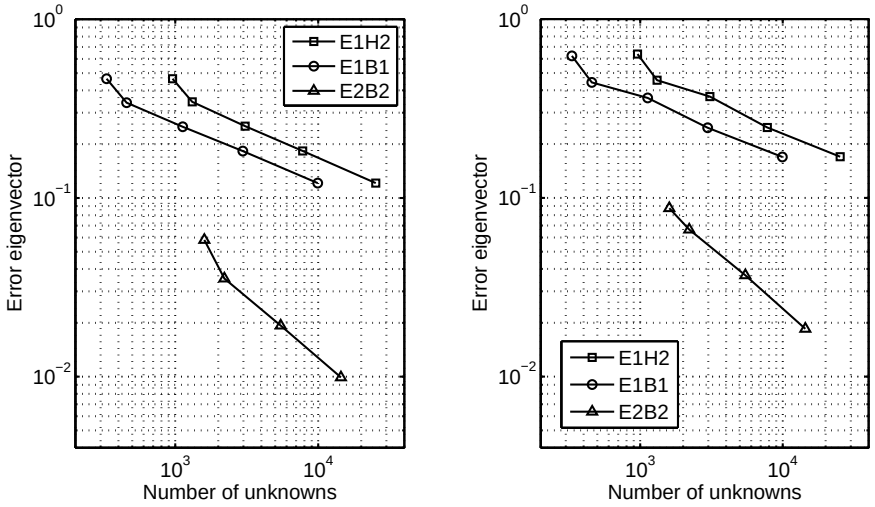

FIGURE 3.25: Error in eigenvectors in cavity discretized with tetrahedra: (a) first mode ($\mathbf{TE}_{110}$), and (b) second mode ($\mathbf{TE}_{101}$).

cavity with a polarization (1,1,1). The first derivative of a Blackman-Harris window with 15 GHz as central frequency is employed as input signal. All cases are solved with four different discretizations, which maximum size equals to $\Delta = 2$, 1.5, 1, and 0.75 mm (PPW = 5, 6.7, 10, and 13.3, respectively). Figure (3.26) illustrates the performance of three formulations. E1H2 has the poorest performance. E1B1 has an accurate result, but it is no better than E2B2 which shows excellent results in numerical dispersion, frequency and field accuracy, and computational efficiency.

3.3.7 Accuracy of the spectral-prism element

In order to understand the accuracy performance of the proposed element, a comparison between exponential and algebraic convergence is presented, i.e. spectral element vs. triangle element, for solving the eigenvalue problem of a rectangular cavity. Two kinds of refinements are used: (i) p-refinement using a single spectral element, and (ii) h-refinement using tetrahedral elements. In the p-refinement case, the order of interpolation changes from 3 to 9, corresponding to a sampling density

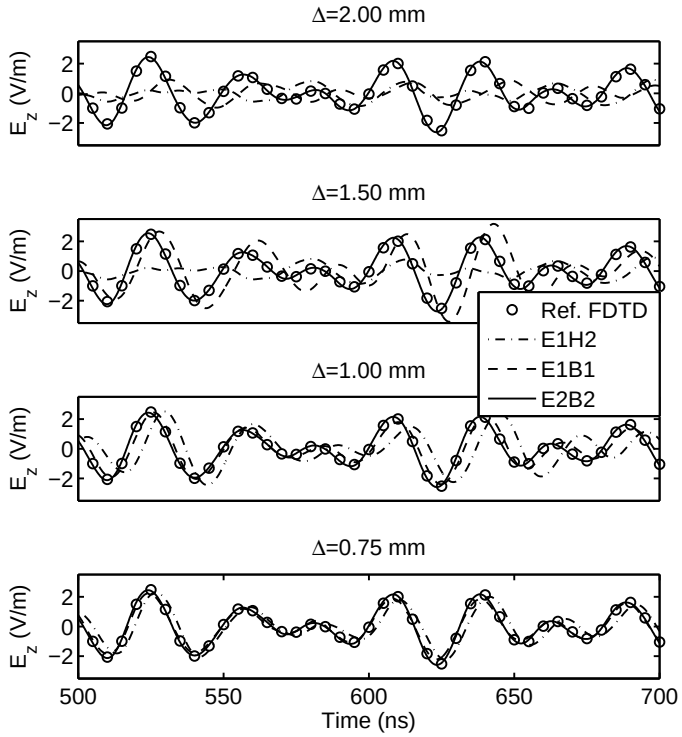

FIGURE 3.26: Transient solution for electric field in cavity.

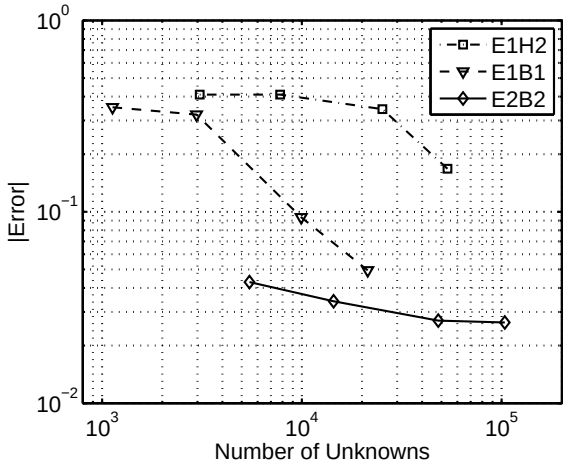

FIGURE 3.27: Mean error vs. number of unknowns

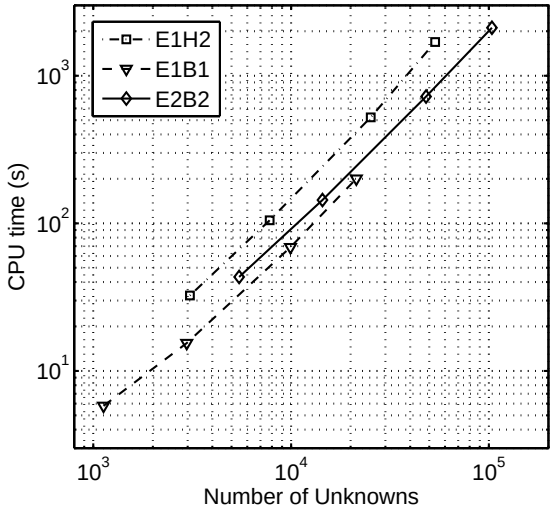

FIGURE 3.28: CPU time vs. number of unknowns

of 6 to 18 points per wavelength for the first mode, respectively. In the h-refinement case, the average size of the tetrahedra changes from 2.5 to 5, corresponding to a sampling density of 8 to 16 points per wavelength for the first mode, respectively.

Figure 3.29 shows the errors of $\mathbf{TE}_{110}$ and $\mathbf{TE}_{210}$ modes for both kinds of elements. Algebraic and exponential convergence are obtained for tetrahedral and

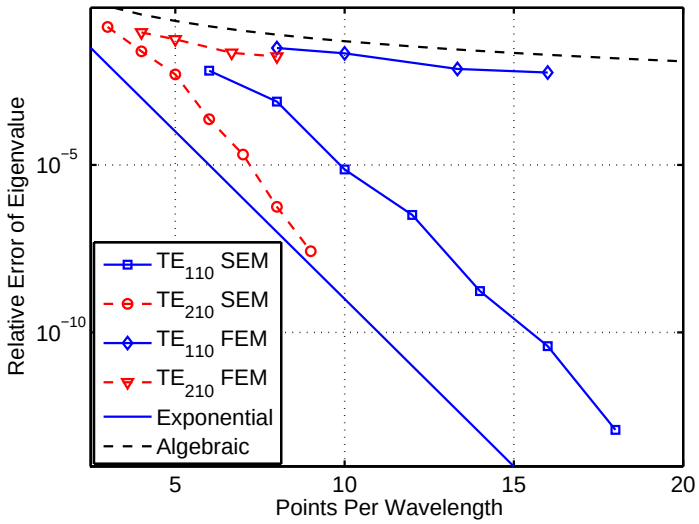

FIGURE 3.29: Exponential and algebraic convergence of SEM and FEM, respectively.

spectral elements, respectively. Similarly, in the spectral-prism elements, the error is dominated by the larger one, usually associated with the triangular face; however, if the size of the triangular element is small enough to describe fine structures, the error of the spectral element is larger. If the triangular error dominates, increasing the order of interpolation in spectral elements does not improve the result, and a refinement of the triangular mesh produces a slower algebraic improvement. On the other hand, if the error from spectral elements dominates, increasing the order of interpolation produces huge (in fact exponential) improvement in the solution until the error reaches the triangular error.

Algebraic accuracy of the spectral-prism element

A coaxial air-filled cavity, with inner radius a, outter radius, b, and heigth d, is used to study the performance of prismatic elements. Analytical solution for this cavity is governed by following expression:

$$f_{\mathrm{m,n,p}} = \frac{1}{2\pi\sqrt{\epsilon\mu}}\sqrt{k_{t,m,n}^2 + \left(\frac{p\pi}{d}\right)^2} \tag{3.32}$$

where ϵ and μ define electric and magnetic properties, respectively; p defines the order in the height direction, and $k_{t,m,n}$ is the transverse wavenumber, which can be obtained by solving the two trascendental equations (3.33) and (3.34), for TM and TE modes, respectively:

$$J_m\left(k_{TM}a\right)Y_m\left(k_{TM}b\right) = J_m\left(k_{TM}b\right)Y_m\left(k_{TM}a\right) \tag{3.33}$$

$$J'_m\left(k_{TE}a\right)Y'_m\left(k_{TE}b\right) = J'_m\left(k_{TE}b\right)Y'_m\left(k_{TE}a\right) \tag{3.34}$$

where J_m and Y_m are Bessel functions of the first and the second kind, respectively, and J'_m and Y'_m are the derivatives of these functions respect to the argument. The

Table 3.3: Solutions of equations (3.33) and (3.34). In bold are the modes used for analysis.

	TM/TE		
m\n	1	2	3
0	**1.0366** / 1.0782	2.0886 / 2.1116	3.1377 / 3.3153
1	1.0782 / **0.2924**	2.1116 / 1.1318	3.3153 / 2.1366
2	1.1932 / **0.5685**	2.1789 / 1.2832	3.1997 / 2.2112
3	1.3599 / **0.8216**	2.2870 / 1.5070	3.2759 / 2.3332
4	1.5579 / 1.0564	2.4303 / 1.7705	3.3801 / 2.5002
5	1.7726 / 1.2806	2.6028 / 2.0450	3.5103 / 2.7086

Table 3.4: First ten modes in coaxial cavity filled with air with dimensions $a = 2mm$, $b = 5mm$, and $d = 20mm$.

Mode	Frequency (GHz)
$\mathbf{TEM}_1$	7.494811
$\mathbf{TEM}_2$	14.989622
$\mathbf{TE}_{1,1,1}$	15.846394
$\mathbf{TE}_{1,1,2}$	20.490442
$\mathbf{TEM}_3$	22.500000
$\mathbf{TE}_{1,1,3}$	26.478448
$\mathbf{TE}_{2,1,1}$	28.160966
$\mathbf{TEM}_4$	29.979246

solutions of these equations defines the number n used in each mode. Table 3.3 shows a set of 15 solutions for magnetic and electric transverse modes of propagation, but just four (bolded) are used in this analysis . In case of TEM modes, $k_{TEM} = 0$.

Table 3.4 shows seven modes for the coaxial cavity, based on the solution of (3.32). Numerical solutions are found by discretization using tetrahedral, hexahedral and prismatic elements. Figure (3.30) shows these three meshes. The tetrahedral and hexahedral elements use Constant-tangential/Linear-normal (Ct/Ln) basis functions for electric field (Peterson et al., 1998), and Linear-tangential/Quadratic-normal (Lt/Qn) for magnetic field (Peterson et al., 1998). This combination of curl-conforming basis functions are free of spurious modes (Chen et al., 2010).

Respect to tetrahedral and hexahedral element, the prismatic element presents

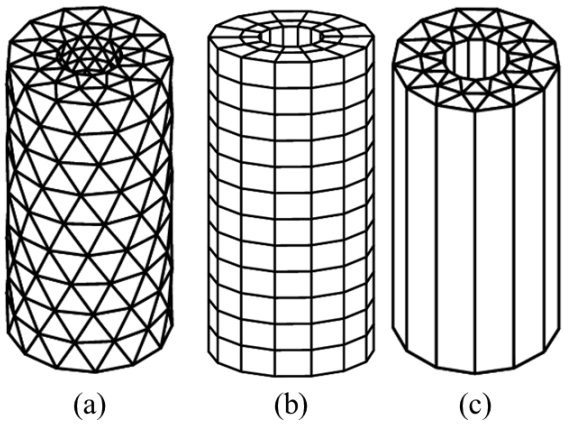

FIGURE 3.30: Discretization of coaxial cavity with: (a) tetrahedra, (b) hexahedra, and (c) prisms.

better accuracy per number of unknowns, as we can see in Figure (3.31). In both cases, algebraic convergence of the $\mathbf{TEM}_4$ and $\mathbf{TE}_{2,1,1}$ modes are obtained.

Spectral accuracy of the spectral-prism element

To verify the spectral accuracy, a very thin coaxial cavity is discretized. The inner and outter radius are 0.95 mm and 1 mm, respectively, and the height is 20 mm. The average size of the triangles is $\delta = 0.05$ mm, then a single layer of 240 very small triangles are used to discretize the base of the cylinder; in contrast, the height of the prism is $H = 20$ mm. Thus, for this case the base to height ratio is 400.

Figure 3.32 shows the error of the first four **TEM** modes. The convergence is exponential until the triangular error is reached, then an increment in the order of interpolation does not improve the accuracy. Another important aspect in this analysis, which is also clear in Figure 3.32, is that the number of modes allowed in the system increases with the order of interpolation, for example, the third and fourth modes appear with order 4 and 7, respectively.

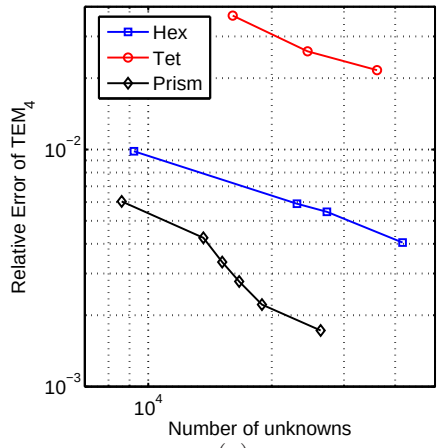

(a)

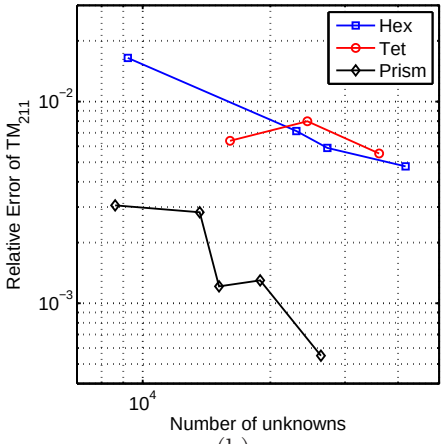

(b)

FIGURE 3.31: Convergence of 3 modes versus number of unknowns for different kinds of element. (a) $\mathbf{TEM}_4$, and (b) $\mathbf{TE}_{2,1,1}$.

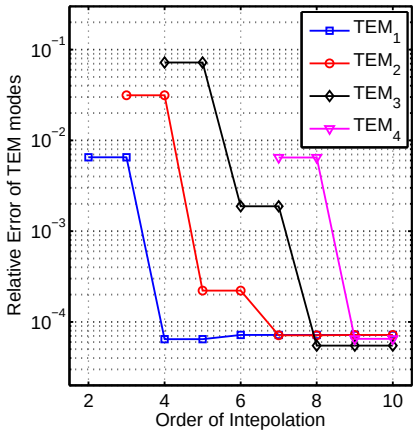

FIGURE 3.32: Convergence of TEM modes in a thin coaxial cavity discretized with spectral-prism elements

4

Domain Decomposition Method

Discontinuous Galerkin time-domain (DGTD) methods (Cockburn et al., 2004; Lu et al., 2004; Xiao and Liu, 2005; Canouet et al., 2005; Buffa and Perugia, 2006; Lee et al., 2009; Chen et al., 2010, 2011; Chen and Liu, 2013) are promising in solving electrically large problems with multiple scales. As DGTD allows the domain decomposition method, three main advantages respect to FDTD and FETD can be detailed: first, flexiblity in geometry modeling, thus each subdomain can be discretized with different kind of elements, and mesh densities; second, large system matrices are split into a set of smaller matrices, allowing the solution of problems too large to be solved by the conventional methods; and third, there are multiple choices for time integration to be used in different subdomains, for example, efficient explicit schemes can be applied to subdomains with coarser meshes, while unconditionally stable implicit schemes can be employed in subdomains with dense meshes. These flexibilities in both spatial and temporal discretization make DGTD efficient in multiscale simulations.

4.1 DGTD Formulations

Assume the computational domain is divided into N subdomains. Denote the i^{th} subdomain as the local subdomain, and j^{th} as an adjacent one. Applying integration by parts to (2.21) and (2.22), we can obtain

$$\begin{aligned}
&\int_V \mathbf{\Theta}_p^{(i)} \cdot (\frac{\partial \mathbf{D}^{(i)}}{\partial t} + \sigma_e \mathbf{E}^{(i)} + \mathbf{J}^{(i)}) dV \\
&\qquad = \int_V \nabla \times \mathbf{\Theta}_p^{(i)} \cdot \mathbf{H}^{(i)} dV \\
&\qquad + \int_S \mathbf{\Theta}_p^{(i)} \cdot (\hat{\mathbf{n}}^{(i)} \times \mathbf{H}^{tot}) dS
\end{aligned} \tag{4.1}$$

$$\begin{aligned}
&\int_V \mathbf{\Upsilon}_p^{(i)} \cdot (\frac{\partial \mathbf{B}^{(i)}}{\partial t} + \sigma_m \mathbf{H}^{(i)} + \mathbf{M}^{(i)}) dV \\
&\qquad = -\int_V \nabla \times \mathbf{\Upsilon}_p^{(i)} \cdot \mathbf{E}^{(i)} dV \\
&\qquad - \int_S \mathbf{\Upsilon}_p^{(i)} \cdot (\hat{\mathbf{n}}^{(i)} \times \mathbf{E}^{tot}) dS
\end{aligned} \tag{4.2}$$

where $\mathbf{\Theta}_p$ and $\mathbf{\Upsilon}_q$ are testing functions selected according to $\mathbf{D}$ and $\mathbf{B}$; $(\cdot)^{(i)}$ represents the vector for the i^{th} subdomain, $\hat{\mathbf{n}}^{(i)}$ is its outward normal vector on the boundary, and $(\cdot)^{tot}$ represents the total field. For the volume integration term, $(\cdot)^{tot} = (\cdot)^{(i)}$ and for the surface integration term, $(\cdot)^{tot}$ is from the contribution of both the i^{th} subdomain and the j^{th} subdomain.

To deal with $\hat{\mathbf{n}}^{(i)} \times \mathbf{E}^{tot}$ and $\hat{\mathbf{n}}^{(i)} \times \mathbf{H}^{tot}$, two different schemes are used: centered flux and Riemann solver (Mohammadian et al., 1991). The former uses the average

of the fields; the latter use the solution of reflection and transmission coefficients of a plane wave incident to an interface.

The formulations of the centered flux are:

$$(\hat{\mathbf{n}}^{(i)} \times \mathbf{E}^{tot}) = \frac{1}{2}(\hat{\mathbf{n}}^{(i)} \times \mathbf{E}^{(i)} + \hat{\mathbf{n}}^{(i)} \times \mathbf{E}^{(j)}) \tag{4.3}$$

$$(\hat{\mathbf{n}}^{(i)} \times \mathbf{H}^{tot}) = \frac{1}{2}(\hat{\mathbf{n}}^{(i)} \times \mathbf{H}^{(i)} + \hat{\mathbf{n}}^{(i)} \times \mathbf{H}^{(j)}) \tag{4.4}$$

The formulations of the Riemann solver are:

$$(\hat{\mathbf{n}}^{(i)} \times \mathbf{E}^{tot}) = \frac{\hat{\mathbf{n}} \times \left(Y^{(i)}\mathbf{E}^{(i)} + Y^{(j)}\mathbf{E}^{(j)}\right)}{Y^{(i)} + Y^{(j)}} - \frac{\hat{\mathbf{n}} \times \hat{\mathbf{n}} \times \left(\mathbf{H}^{(i)} - \mathbf{H}^{(j)}\right)}{Y^{(i)} + Y^{(j)}} \tag{4.5}$$

$$(\hat{\mathbf{n}}^{(i)} \times \mathbf{H}^{tot}) = \frac{\hat{\mathbf{n}} \times \left(Z^{(i)}\mathbf{H}^{(i)} + Z^{(j)}\mathbf{H}^{(j)}\right)}{Z^{(i)} + Z^{(j)}} + \frac{\hat{\mathbf{n}} \times \hat{\mathbf{n}} \times \left(\mathbf{E}^{(i)} - \mathbf{E}^{(j)}\right)}{Z^{(i)} + Z^{(j)}} \tag{4.6}$$

where $Z^{(i)}$ and $Y^{(i)} = 1/Z^{(i)}$ are the impedance and admitance in the i^{th} domain, respectively.

4.1.1 The EH-based scheme

If $\mathbf{E}$ and $\mathbf{H}$ are selected the linear system for the i^{th} subdomain is

$$\mathbf{M}_{ee}^{(i)}\frac{d\mathbf{e}^{(i)}}{dt} = \mathbf{K}_{eh}^{(i)}\mathbf{h}^{(i)} + \mathbf{C}_{ee}^{(i)}\mathbf{e}^{(i)} + \mathbf{j}^{(i)} + \sum_{j=1}^{N}\left(\mathbf{L}_{ee}^{(i,j)}\mathbf{e}^{(j)} + \mathbf{L}_{eh}^{(i,j)}\mathbf{h}^{(j)}\right),\ i = 1,\ldots N \tag{4.7}$$

$$\mathbf{M}_{hh}^{(i)}\frac{d\mathbf{h}^{(i)}}{dt} = \mathbf{K}_{he}^{(i)}\mathbf{e}^{(i)} + \mathbf{C}_{hh}^{(i)}\mathbf{h}^{(i)} + \mathbf{m}^{(i)} + \sum_{j=1}^{N}\left(\mathbf{L}_{he}^{(i,j)}\mathbf{e}^{(j)} + \mathbf{L}_{hh}^{(i,j)}\mathbf{h}^{(j)}\right),\ i = 1,\ldots N \tag{4.8}$$

where $\mathbf{L}_{ee}^{(i,j)}$, $\mathbf{L}_{eh}^{(i,j)}$, $\mathbf{L}_{he}^{(i,j)}$ and $\mathbf{L}_{hh}^{(i,j)}$are communication matrices between subdomain i and j. The formulations for these matrices are

$$(\mathbf{L}_{eh}^{(ij)})_{pq} = \frac{Z^{(j)}}{Z^{(ij)}} \langle \mathbf{\Phi}_p^{E,(i)}, (\hat{\mathbf{n}}^{(i)} \times \mathbf{\Phi}_q^{H,(j)}) \rangle_{S_{ij}} \tag{4.9}$$

$$(\mathbf{L}_{he}^{(ij)})_{pq} = -\frac{Y^{(i)}}{Y^{(ij)}} \langle \mathbf{\Phi}_p^{H,(i)}, (\hat{\mathbf{n}}^{(i)} \times \mathbf{\Phi}_q^{E,(j)}) \rangle_{S_{ij}} \tag{4.10}$$

$$(\mathbf{L}_{ee}^{(ij)})_{pq} = \frac{1}{Z^{(ij)}} \langle (\hat{\mathbf{n}}^{(i)} \times \mathbf{\Phi}_p^{E,(i)}), (\hat{\mathbf{n}}^{(i)} \times \mathbf{\Phi}_q^{E,(j)}) \rangle_{S_{ij}} \tag{4.11}$$

$$(\mathbf{L}_{hh}^{(ij)})_{pq} = -\frac{1}{Y^{(ij)}} \langle (\hat{\mathbf{n}}^{(i)} \times \mathbf{\Phi}_p^{H,(i)}), (\hat{\mathbf{n}}^{(i)} \times \mathbf{\Phi}_q^{H,(j)}) \rangle_{S_{ij}} \tag{4.12}$$

where $Z^{(ij)} = Z^{(i)} + Z^{(j)}$ and $Y^{(ij)} = Y^{(i)} + Y^{(j)}$; and S_{ij} is the interface between the i^{th} and j^{th} subdomains.

4.1.2 The EB-based scheme

Similarly, if $\mathbf{E}$ and $\mathbf{B}$ are selected the linear system for the i^{th} subdomain is

$$\mathbf{M}_{ee}^{(i)} \frac{d\mathbf{e}^{(i)}}{dt} = \mathbf{K}_{eb}^{(i)} \mathbf{b}^{(i)} + \mathbf{C}_{ee}^{(i)} \mathbf{e}^{(i)} + \mathbf{j}^{(i)} + \sum_{j=1}^{N} \mathbf{L}_{eb}^{(ij)} \mathbf{b}^{(j)}, \ i = 1, \ldots N \tag{4.13}$$

$$\mathbf{M}_{bb}^{(i)} \frac{d\mathbf{b}^{(i)}}{dt} = \mathbf{K}_{be}^{(i)} \mathbf{e}^{(i)} + \mathbf{C}_{bb}^{(i)} \mathbf{b}^{(i)} + \mathbf{m}^{(i)} + \sum_{j=1}^{N} \mathbf{L}_{be}^{(ij)} \mathbf{e}^{(j)}, \ i = 1, \ldots N \tag{4.14}$$

where the mass matrices $\mathbf{M}_{ee}{}_{pq}^{(i)}$, $\mathbf{M}_{bb}{}_{pq}^{(i)}$, the damping matrices $\mathbf{C}_{ee}{}_{pq}^{(i)}$, $\mathbf{C}_{bb}{}_{pq}^{(i)}$ and the stiffness matrices $\mathbf{K}_{eb}{}_{pq}^{(i)}$, $\mathbf{K}_{be}{}_{pq}^{(i)}$ are the same as (2.32)-(2.36) and the other elemental matrices are

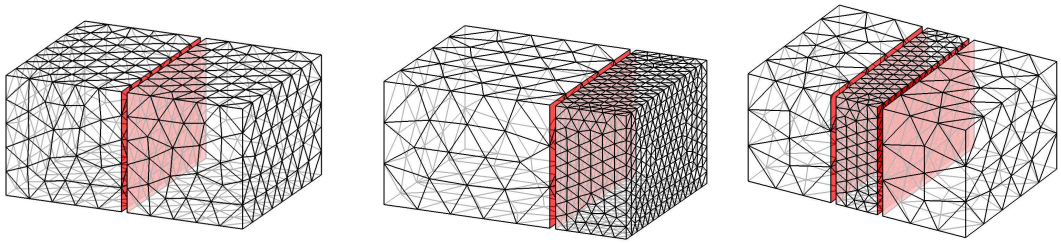

(a) (b) (c)

FIGURE 4.1: PEC cavity with three different multidomain discretizations: (a) Two-domains with the same dimensions and element sizes ($\triangle_i = 1$, $i = 1, 2$); (b) Two-domains with different dimensions and different element sizes ($\triangle_1 = 1.5$ and $\triangle_2 = 0.5$); and (c) Three domains with different dimensions and different element sizes ($\triangle_1 = 1.5$, $\triangle_2 = 0.5$ and $\triangle_3 = 1.5$).

$$(\mathbf{L}_{eb}^{(ij)})_{pq} = \frac{1}{2}\langle \mathbf{\Phi}_p^{E,(i)}, (\hat{\mathbf{n}}^{(i)} \times \frac{\mathbf{\Psi}_q^{B,(j)}}{\mu^{(j)}})\rangle_{S_{ij}} \tag{4.15}$$

$$(\mathbf{L}_{be}^{(ij)})_{pq} = \frac{1}{2}\langle \mathbf{\Psi}_p^{B,(i)}, (\hat{\mathbf{n}}^{(i)} \times \mathbf{\Phi}_q^{E,(j)})\rangle_{S_{ij}} \tag{4.16}$$

where S_{ij} is the interface between the i^{th} and j^{th} subdomains.

4.1.3 Evaluation of DG schemes

Three cases are used for validation. These are shown in Figure (4.1): (a) two domains with same dimensions and element sizes; (b) two domains with different dimensions and element sizes; and (c) three domains with different dimensions and element sizes.

In Figure (4.2) the transient solutions for single and multiple domains show the performance of DGTD under different circunstances: single domain, multiple domains, and different orders of interpolation. Based on these figures, EB scheme (and even more accurate E2B2) fits better to the reference result. Notice that the span of time shown in Figure (4.2) is between 500 and 700 ns, that is enough to show some delay due to numerical dispersion, which is evident in EH scheme. The error in the same time window is presented in Figure (4.3)

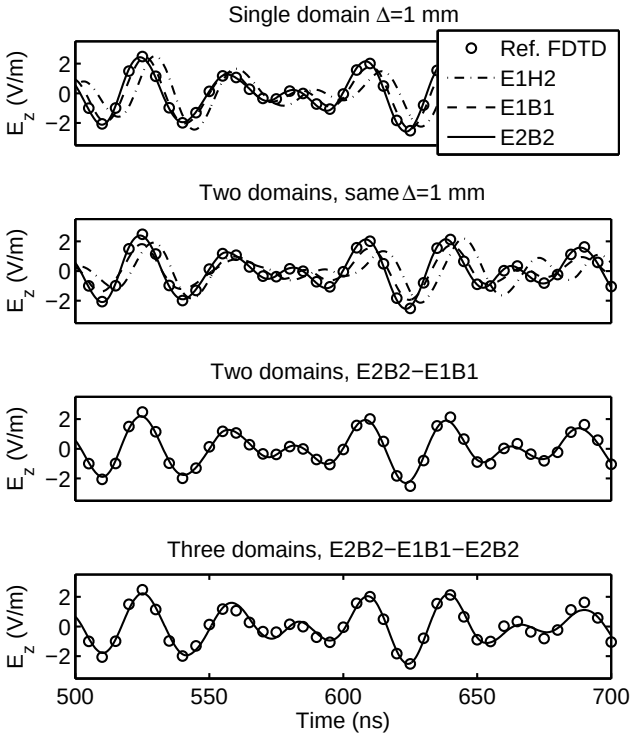

FIGURE 4.2: Transient solution for electric field in cavity in mutidomain cases.

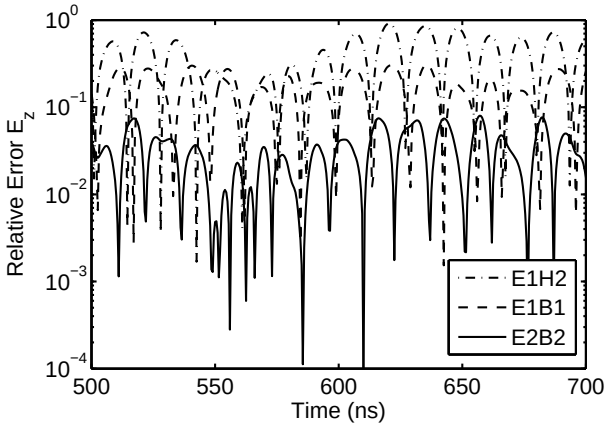

FIGURE 4.3: Error in transient solution for electric field in cavity for two domain case.

Table 4.1: Summary of time stepping schemes

	Accuracy	Stability	CPU time	Memory	Cases
ExRK	High	Conditional	Fast	Low	EH, EB, high order elements
ImExRK	Middle	Conditional	fast	Medium	EH, EB, multiscale structures
CN-GS	Low	Unconditional	Slow	Medium	EH, EB, small structures
CN-BT	High	Unconditional	Fast	High	EH, EB, sequential cases
CN-LDU	High	Unconditional	Fast	Medium	EH, sequential cases

4.2 Time stepping schemes

For concision, let me start rewritting equations (4.7), (4.8), (4.13), and (4.14) in a more compact form

$$\mathbf{M}^{(i)}\frac{d\mathbf{v}^{(i)}}{dt} = \sum_{j=1}^{N}\mathbf{L}^{(i,j)}\mathbf{v}^{(j)} + \mathbf{f}^{(i)},\ i = 1,\dots N \tag{4.17}$$

This equation can be solved using an explicit scheme, then only mass matrices associated with each subdomain need to be inverted during a time step; however, this is not an efficient approach for multiscale simulations with extremely small structures, as the size of the time step, $\triangle t$, is directly related with the size of the smallest elements inside each subdomain. Therefore, a scheme with a $\triangle t$ independent of the discretization, i.e. unconditionally stable, is the best alternative. Also, there are cases with a mix of domains containing coarse meshes, and domains with electrically small structures; in theses cases, a hybrid Implicit-Explicit scheme can be a good strategy to solve a DGTD system under this circunstance. Table 4.1 enumerates four timestepping schemes with some characteristics: accuracy, stability, CPU time cost, memory, and typical cases of application.

4.2.1 Explicit Runge-Kutta (ExRK)

The corresponding time stepping of the ExRK scheme is

$$\mathbf{v}_{n+1}^{(i)} = \mathbf{v}_n^{(i)} + \Delta t \sum_{k=1}^{s} b_k \mathbf{u}_k^{(i)}, \quad i = 1, \cdots, N \tag{4.18}$$

where

$$\begin{aligned} \mathbf{M}^{(i)} \mathbf{u}_k^{(i)} = & \sum_{j=1}^{N} \mathbf{L}^{(ij)} \left(\mathbf{v}_n^{(j)} + \Delta t \sum_{l=1}^{k-1} a_{k,l} \mathbf{u}_l^{(j)} \right) \\ & + \mathbf{f}^{(i)}(t_n + c_k \Delta t), \quad i = 1, \cdots, N \end{aligned} \tag{4.19}$$

The Butcher tableau (Butcher, 2003) of the an s-stage explicit RK scheme is

$$\begin{array}{c|ccccc} 0 & 0 & 0 & \dots & \dots & 0 \\ c_2 & a_{2,1} & 0 & \ddots & \ddots & \vdots \\ c_3 & a_{3,1} & a_{3,2} & 0 & \ddots & \vdots \\ \vdots & \vdots & \vdots & \vdots & \ddots & 0 \\ c_s & a_{s,1} & a_{s,2} & \dots & a_{s,s-1} & 0 \\ \hline & b_1 & b_2 & b_3 & \dots & b_s \end{array} \tag{4.20}$$

4.2.2 Implicit-Explicit Runge-Kutta (ImExRK)

Assuming a discretized multiscale problem contains N_{ex} explicit subdomains and N_{im} implicit subdomains, the time stepping formulation for the i-th subdomain based on IMEX-RK with s stages is

$$\mathbf{v}_{n+1}^{(i)} = \mathbf{v}_n^{(i)} + \Delta t \sum_{k=1}^{s} b_k \mathbf{u}_k^{(i)}, \quad i = 1, \cdots, N_{\text{im}} + N_{\text{ex}} \tag{4.21}$$

where

$$\mathbf{M}^{(i)} \mathbf{u}_k^{(i)} = \sum_{j=N_{\text{im}}+1}^{N_{\text{im}}+N_{\text{ex}}} \mathbf{L}^{(ij)} \left(\mathbf{v}_n^{(j)} + \Delta t \sum_{l=1}^{k-1} a_{k,l}^{\text{ex}} \mathbf{u}_l^{(j)} \right)$$

$$+\sum_{j=1}^{N_{\text{im}}} \mathbf{L}^{(ij)} \left(\mathbf{v}_n^{(j)} + \Delta t \sum_{l=1}^{k} a_{k,l}^{\text{im}} \mathbf{u}_l^{(j)} \right) + \mathbf{f}^{(i)}(t_n + c_k \Delta t) \tag{4.22}$$

for explicit subdomains, and

$$\begin{aligned} \left(\mathbf{M}^{(i)} - \Delta t a_{k,k}^{\text{im}} \mathbf{L}^{(ii)}\right) \mathbf{u}_k^{(i)} &= \mathbf{f}^{(i)}(t_n + c_k \Delta t) \\ &+ \mathbf{L}^{(ii)} \left(\mathbf{v}_n^{(i)} + \Delta t \sum_{l=1}^{k-1} a_{k,l}^{\text{im}} \mathbf{u}_l^{(j)} \right) \\ &+ \sum_{j=N_{\text{im}}+1}^{N_{\text{im}}+N_{\text{ex}}} \mathbf{L}^{(ij)} \left(\mathbf{v}_n^{(j)} + \Delta t \sum_{l=1}^{k-1} a_{k,l}^{\text{ex}} \mathbf{u}_l^{(j)} \right) \end{aligned} \tag{4.23}$$

for implicit subdomains.

The Butcher tableau of the explicit part is

$$\begin{array}{c|ccccc} 0 & 0 & 0 & \dots & \dots & 0 \\ c_2 & a_{2,1}^{\text{ex}} & 0 & \ddots & \ddots & \vdots \\ c_3 & a_{3,1}^{\text{ex}} & a_{3,2}^{\text{ex}} & 0 & \ddots & \vdots \\ \vdots & \vdots & \vdots & \vdots & \ddots & 0 \\ c_s & a_{s,1}^{\text{ex}} & a_{s,2}^{\text{ex}} & \dots & a_{s,s-1}^{\text{ex}} & 0 \\ \hline & b_1 & b_2 & b_3 & \dots & b_s \end{array} \tag{4.24}$$

The Butcher tableau of the implicit part is

$$\begin{array}{c|ccccc} 0 & a_{1,1}^{\text{im}} & 0 & \dots & \dots & 0 \\ c_2 & a_{2,1}^{\text{im}} & a_{2,2}^{\text{im}} & 0 & \ddots & \vdots \\ c_3 & a_{3,1}^{\text{im}} & a_{3,2}^{\text{im}} & a_{3,3}^{\text{im}} & \ddots & \vdots \\ \vdots & \vdots & \vdots & \vdots & \ddots & 0 \\ c_s & a_{s,1}^{\text{im}} & a_{s,2}^{\text{im}} & \dots & a_{s,s-1}^{\text{im}} & a_{s,s}^{\text{im}} \\ \hline & b_1 & b_2 & b_3 & \dots & b_s \end{array} \tag{4.25}$$

4.2.3 Crank-Nicholson (CN) scheme

In CN the discretized system (4.17) is rewritten as

$$\left(\mathbf{M}^{(i)} - \frac{1}{2}\Delta t \sum_{j=1}^{N} \mathbf{L}^{(ij)}\right) \mathbf{v}_{n+1}^{(i)} = \Delta t \mathbf{f}_{n+\frac{1}{2}}^{(i)}$$
$$+ \left(\mathbf{M}^{(i)} + \frac{1}{2}\Delta t \sum_{j=1}^{N} \mathbf{L}^{(ij)}\right) \mathbf{v}_{n}^{(i)}, \quad i = 1, \cdots, N \tag{4.26}$$

In the above equations the coupling matrices $\mathbf{L}^{(ij)}$ appear at the left hand side, which means all subdomains are coupled together and need to be solved simultaneously at each time step. It can be prohibitively expensive to directly solve the CNDG system under this circumstance, and an iterative solver would be a more efficient alternative.

Iterative Gauss-Seidel (GS) method

Take the block Gauss-Seidel iteration as an example: the pseudo code is as follows:

$$\begin{cases} \text{while convergence is not reached} \\ \quad \text{for } i = 1 : N \\ \quad\quad \mathbf{q}^{(i)} = \mathbf{M}^{(i)} \mathbf{v}_n^{(i)} + \mathbf{f}_{n+\frac{1}{2}}^{(i)} \\ \quad\quad \text{for } j = 1 : N \\ \quad\quad\quad \mathbf{q}^{(i)} = \mathbf{q}^{(i)} + \frac{1}{2}\Delta t \mathbf{L}^{(ij)} \mathbf{v}_n^{(j)} \\ \quad\quad \text{end} \\ \quad\quad \text{for } j = 1 : i-1 \text{and } j = i+1 : N \\ \quad\quad\quad \mathbf{q}^{(i)} = \mathbf{q}^{(i)} + \frac{1}{2}\Delta t \mathbf{L}^{(ij)} \mathbf{v}_{n+1}^{(j)} \\ \quad\quad \text{end} \\ \quad\quad \text{solve } \left(\mathbf{M}^{(i)} - \frac{1}{2}\Delta \mathbf{L}^{(ii)}\right) \mathbf{u}_{n+1}^{(i)} = \mathbf{q}^{(i)} \\ \quad \text{end} \\ \text{end} \end{cases} \tag{4.27}$$

Generally in CN-GS the convergence rate of each time steps depends on the number of subdomains.

The Block-Thomas algorithm

When simulating layered structures, the partition of subdomains can be sequentially ordered layer by layer, and this will lead to a tri-diagonal system when an implicit DGTD method is implemented:

$$\begin{bmatrix} \mathbf{B}_1 & \mathbf{C}_1 & \mathbf{0} & \dots & \mathbf{0} \\ \mathbf{A}_2 & \mathbf{B}_2 & \mathbf{C}_2 & \ddots & \vdots \\ \mathbf{0} & \mathbf{A}_3 & \mathbf{B}_3 & \ddots & \mathbf{0} \\ \vdots & \ddots & \ddots & \ddots & \mathbf{C}_{M-1} \\ \mathbf{0} & \dots & \mathbf{0} & \mathbf{A}_M & \mathbf{B}_M \end{bmatrix} \begin{bmatrix} \mathbf{u}_1 \\ \mathbf{u}_2 \\ \vdots \\ \vdots \\ \mathbf{u}_M \end{bmatrix} = \begin{bmatrix} \mathbf{q}_1 \\ \mathbf{q}_2 \\ \vdots \\ \vdots \\ \mathbf{q}_M \end{bmatrix} \tag{4.28}$$

The block Thomas algorithm designed for a block tri-diagonal system can be used here to accelerate the process of solving (4.28). The pseudo code of the block Thomas algorithm is as follows

$$\begin{cases} \text{solve } \ \mathbf{B}_1\mathbf{C}'_1 = \mathbf{C}_1 \\ \text{for } i = 2 : M-1 \\ \quad \mathbf{B}'_i = \mathbf{B}_i - \mathbf{A}_i\mathbf{C}'_{i-1} \\ \quad \text{solve } \ \mathbf{B}'_i\mathbf{C}'_i = \mathbf{C}_i \\ \text{end} \\ \text{solve } \ \mathbf{B}_1\mathbf{q}'_1 = \mathbf{q}_1 \\ \text{for } i = 2 : M \\ \quad \text{solve } \ \mathbf{B}'_i\mathbf{q}'_i = \left(\mathbf{q}_i - \mathbf{A}_i\mathbf{q}'_{i-1}\right) \\ \text{end} \\ \mathbf{u}_M = \mathbf{q}'_M \\ \text{for } i = M-1 : -1 : 1 \\ \quad \mathbf{u}_i = \mathbf{q}'_i - \mathbf{C}'_i\mathbf{u}_{i+1} \\ \text{end} \end{cases} \tag{4.29}$$

In other words, the block Thomas algorithm is an iteration-free time stepping scheme solving the tri-diagonal system in a deterministic number of steps of operation. This method could be faster than the conventional implicit DGTD methods in modeling complex structures with many layers (Chen et al., 2011).

The LDU algorithm

The block-Thomas (BT) algorithm presented in (Chen et al., 2011) was designed to accelerate the process of solving (4.28). This method is based on a block LU decomposition, with forward and backward substitutions. This algorithm is free of iteration, then is very accurate and fast. However, the drawback of the method is the dense matrices those appear in the block matrix U. These matrices are memory expensive resulting in limitation in the size of possible EM problems to solved. We can clarify this point with the following two domains system, where the matrix G^1 is a dense one.

$$\begin{bmatrix} \mathbf{A}^{1,1} & \mathbf{B}^{1,2} \\ \mathbf{B}^{2,1} & \mathrm{A}^{2,2} \end{bmatrix} \begin{bmatrix} \mathbf{u}^1 \\ \mathbf{u}^2 \end{bmatrix} = \begin{bmatrix} \mathcal{A}^1 & \mathbf{0} \\ \mathbf{B}^{2,1} & \mathcal{A}^2 \end{bmatrix} \begin{bmatrix} \mathbf{I} & \mathbf{G}^1 \\ \mathbf{0} & \mathbf{I} \end{bmatrix} \begin{bmatrix} \mathbf{u}^1 \\ \mathbf{u}^2 \end{bmatrix} \tag{4.30}$$

Thus, to solve this issue a LDU decomposition with a reordering of unknowns is implemented. In this way, the linear system is lighter than that used in BT. The follow is the LDU decomposition for two domains:

$$\mathbf{LDU} \begin{bmatrix} \mathbf{u}_V^1 \\ \mathbf{u}_V^2 \\ \mathbf{u}_{S^+}^1 \\ \mathbf{u}_{S^-}^2 \end{bmatrix} = \begin{bmatrix} \mathbf{v}_V^1 \\ \mathbf{v}_V^2 \\ \mathbf{v}_{S^+}^1 \\ \mathbf{v}_{S^-}^2 \end{bmatrix} \tag{4.31}$$

where

$$\mathbf{L} = \begin{bmatrix} \mathrm{I} & 0 & 0 & 0 \\ 0 & \mathrm{I} & 0 & 0 \\ (\mathbf{W}^1)^T & 0 & \mathrm{I} & 0 \\ 0 & (\mathbf{W}^2)^T & 0 & \mathrm{I} \end{bmatrix}$$

$$\mathbf{D} = \begin{bmatrix} \mathbf{A}_V^{1,1} & 0 & 0 & 0 \\ 0 & \mathbf{A}_V^{2,2} & 0 & 0 \\ 0 & 0 & \mathbf{A}_{S^+}^{1,2} & \mathbf{B}^{1,2} \\ 0 & 0 & \mathbf{B}^{2,1} & \mathbf{A}_{S^-}^{2,1} \end{bmatrix}$$

$$\mathbf{U} = \begin{bmatrix} \mathrm{I} & 0 & \mathbf{W}^1 & 0 \\ 0 & \mathrm{I} & 0 & \mathbf{W}^2 \\ 0 & 0 & \mathrm{I} & 0 \\ 0 & 0 & 0 & \mathrm{I} \end{bmatrix}$$

where $\mathbf{W}^i$ is the communication matrix between interface unknowns and volume unknowns of the i^{th} subdomain; $\mathbf{u}_V^i$ is a vector of volume unknowns in the i^{th} subdomain; and, $\mathbf{u}_{S^-}^i$and $\mathbf{u}_{S^+}^i$ are vector of unknowns on the interfaces of the i^{th} subdomain connected to the $(i-1)^{th}$ and $(i+1)^{th}$ neighbor subdomains, respectively. As we can see, the solution of this system include forward and backward subsitutions (for L and U block matrices), but also independent solutions of volume unknowns and a block Thomas for the interface unknowns.

To evaluate the LDU algorithm let us use three cases with multiple domains, all with the same number of unknowns. With these models we can verify the performance of the LDU decomposition respect to the BT method. The three discretized system used in this analysis, shown in Figure (4.4), have two, three and four domains, respectively. Comparison of electric field is presented in Figures (4.5) and (4.6). We can see a perfect agreement between the LDU and BT methods. These results show that the new algorithm does not decrease the accuracy of the solution, respect to BT algorithm.

In Figure (4.7), the memory cost and CPU time for the new algorithm are compared to BT algorithm for different number of subdomains. We can note a reduction of more than four times in memory consumption, which allows the solution of larger EM problems. The reduction in CPU time is not dramatic, but still an important

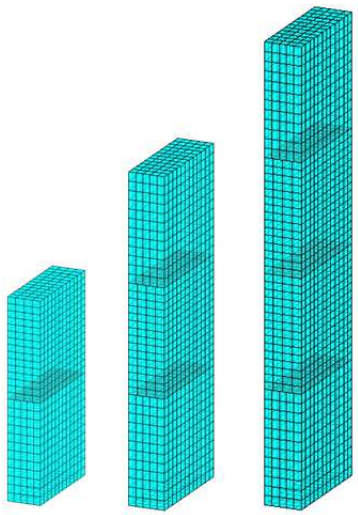

FIGURE 4.4: Cavities with two, three and four domains used for verification.

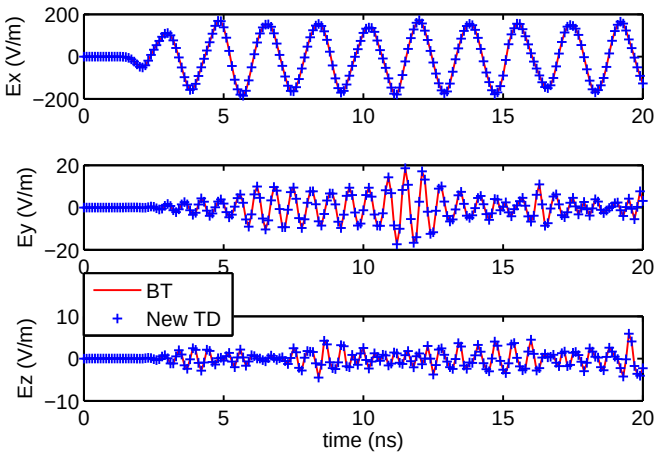

FIGURE 4.5: Electric field in x, y, and z direction, case with two domains

improvement close to 25%.

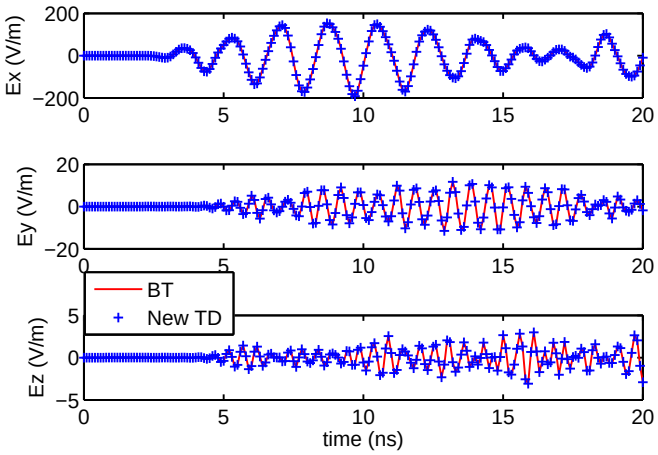

FIGURE 4.6: Electric field in x, y, and z direction, case with three domains

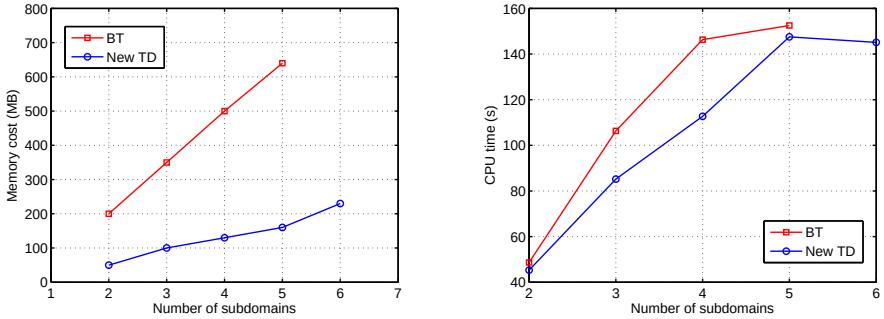

(a) (b)

FIGURE 4.7: Improvements in memory cost and CPU time for the proposed method.

5

Cases of Application

5.1 EH scheme

5.1.1 Multilayer Microwave Filter

In high frequency, the design of small devices based on electrically small PEC structures in multilayer configuration inside a chip is a complex task and a full wave analysis with an EM simulator is required. This kind of devices can be composed by N layers as shown in Figure 5.1, each one with a different geometry; thus, they represent a very suitable geometry to evaluate the method proposed in this work. Then, as a case of application, a band pass microwave multilayer filter is presented, with accurate results and improvement in computational costs.

Model

In Figure 5.2, vertical dashed lines represent electric connection between layers through PEC columns. Plates in layers 1, 2 and 3 conform two capacitors; plates in layers 1 and 3 conform with the shield two input capacitors connected to ground; finally, one inductor (dashed circle in Figure 5.2) connects the plate with the shield. The dimensions of the chip are 8 mm by 5.4 mm by 0.9 mm. The PEC plates in

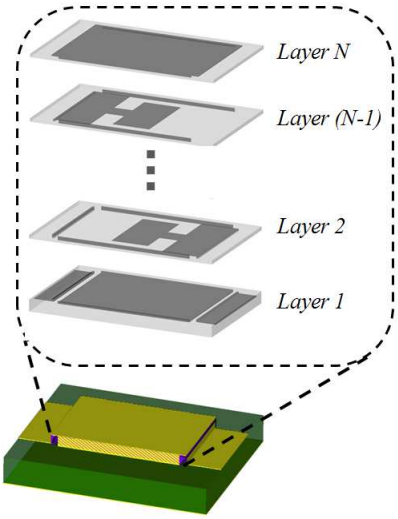

FIGURE 5.1: Typical chip on a board composed by N layers

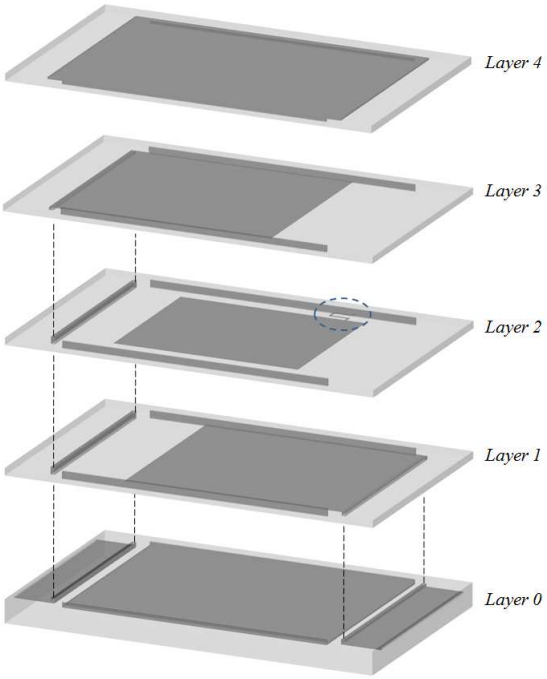

FIGURE 5.2: Layers inside the microwave filter chip. Vertical dashed lines shows a PEC connection between subdomains, and the dashed circle shows the small inductor in layer 2.

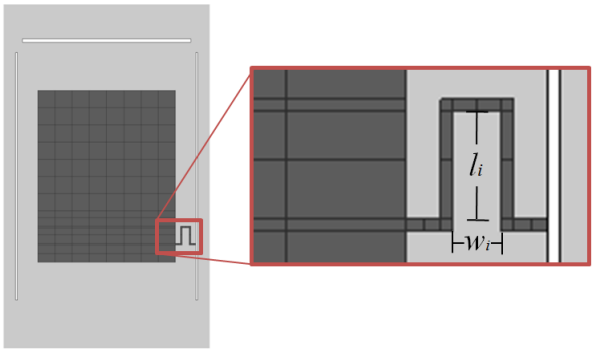

FIGURE 5.3: Detail of inductor in layer 2

layers 1 and 3 have dimensions 6 mm by 4.9 mm, and the plate in layer 2 has dimensions 4 mm by 5 mm. The thickness of internal plates is 6 μm and of the shield is 50 μm. The geometry of the "u" shape inductor is shown in Figure 5.3 with l_i=0.45 mm and w_i=0.2 mm. A "hard" dielectric used to fill the chip is an isotropic GaAs with relative permittivity of 12.8. The chip is connected to two 50 Ω microstrip lines with length of 21 mm, width of 4.9 mm and thickness of 0.05 mm; a "soft" dielectric used as a substrate is Duriod 4880 with relative permittivity of 2.2. Finally, lumped ports are connected at each end of the lines to capture incident and reflected signals. The whole structure is located inside a PEC cavity with dimensions 60 mm by 14 mm by 4 mm.

Numerical Results

The measurement of voltages was performed with the highest working frequency as 3 GHz. The source is located in port 1, and a first derivative of a Blackman-Harris windows with a characteristic frequency of 1 GHz is used. Under this consideration, the smallest wavelenght is found in 3 GHz inside the chip, with $\lambda_{min} \approx 28$ mm, which is 4658 times the smallest dimension of the structure; thus, this structure is a multiscale problem with electrically small structures, a very appropriate one for the method proposed in this paper. Figure 5.4(a) and 5.4(b) show the voltage in ports 1 and 2, respectively, with a very good agreement between DG-FETD and the

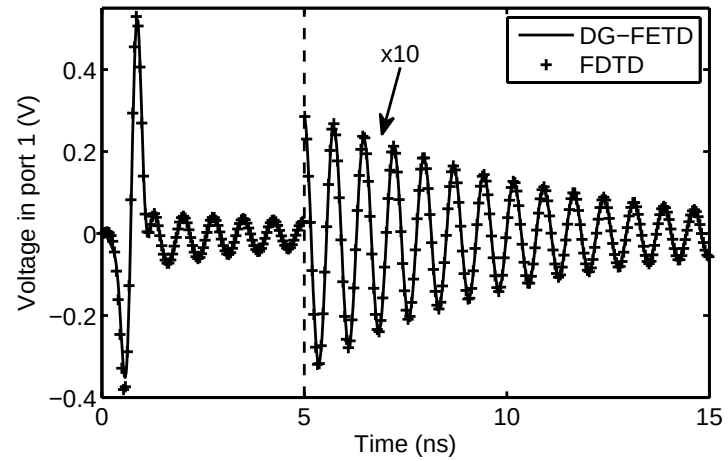

(a)

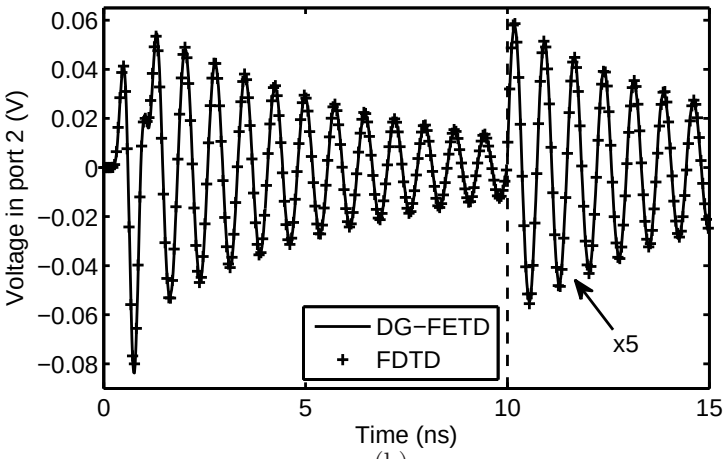

(b)

FIGURE 5.4: Voltage in port 1 (a), and port 2 (b).

well known FDTD method, in all range of time. In frequency domain, a comparison between CST and FDTD shows a good agreement in both scattered parameters, as Figures 5.5(a) and 5.5(b) illustrate. Comparisons in computational costs are summarized in table 5.1, with an improvement in all features, for instance: a reduction at least one order of magnitude in number of unknowns respect to both methods, FDTD and CST; time step size is 3 order larger because implicit CN-GS method is used; and CPU time is 15 and 25 times smaller than used in FDTD and CST respectively. Finally, as an example of the advantage of the method, it is presented

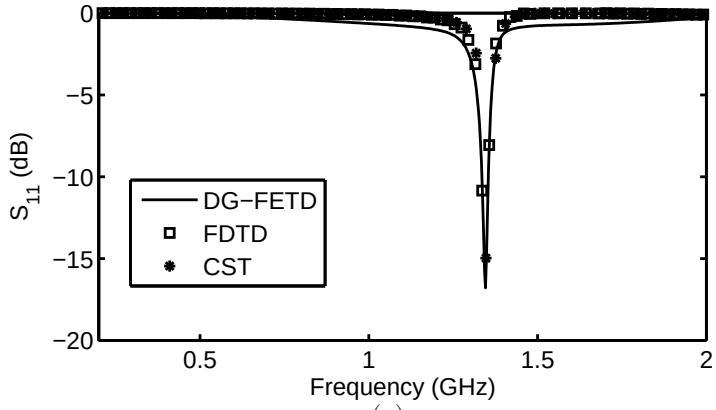

(a)

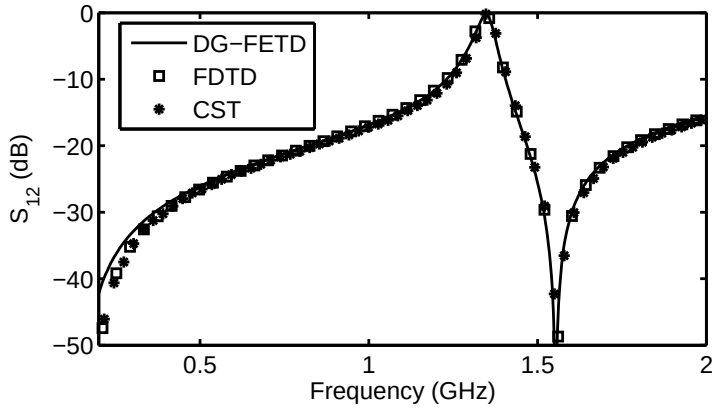

(b)

FIGURE 5.5: Scattered parameters: (a) S11, and (b) S12.

a variation in the response of the filter as a function of small changes in the length of the inductor shows a high sensibility to this parameters, as illustrated in Figure 5.6 shows. This analysis (three different configurations) can be developed in less than one and a half hours, respect to almost 6 hours required by FDTD or more than one day by CST, just for one simulation.

5.1.2 Multilayer package-to-chip system

In this case spectral-prism elements are used to discretize each subdomain and block Thomas algorithm is used to accelerate the implicit Crank-Nicholson time stepping method. The model is splitted into six subdomains are used to decompose a layered

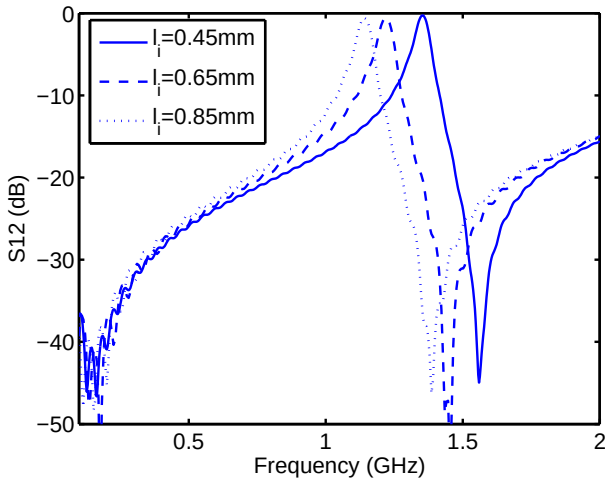

FIGURE 5.6: Variation of center frequency with changes in the length of the inductor.

Table 5.1: Computational costs in microwave filter

	FDTD	CST	DG-FETD
Number of unknowns	3763200	13303453	221211
Memory (MB)	120	609	250
$\triangle t$	18.6 fs	55.5 fs	20 ps
CPU time (h)	5.9	10.2	0.4

structure with two different electrical scales. The basic structure of each layer is shown in Figure 5.7. The bottom layer contains six different package interconnects, two of them are used as ports 1 and 4 in the following results. Transient voltages are shown in Figure 5.8, with very good agreement with the FDTD results; and scattered parameters are presented in Figure 5.9 compared to FDTD and HFSS results. Computational costs are presented in Table 5.2. The DG-FETD method costs less CPU time, and has a higher memory consumption with respect to other methods.

5.1.3 LDU algorithm for highly multiscale problems

The next case is designed to verify and evaluate the performance of the LDU algorithm to solve cases with large multiscale factor. The structure is shown in Figure

Table 5.2: Computational costs in Package-to-Chip case

Method	Memory (MB)	CPU time (s)
Explicit FDTD	1.4	2160
HFSS	66	686
Prism DG-FETD	80	360

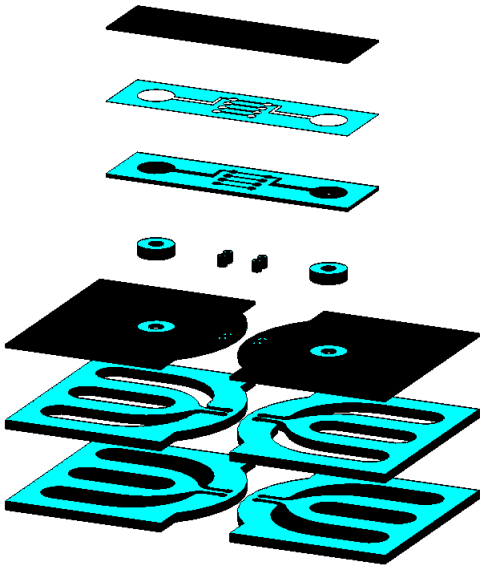

FIGURE 5.7: Basic dimensions in the multiscale and multilayer case, from package interconnects (mm) to chip interconnects (μm) .

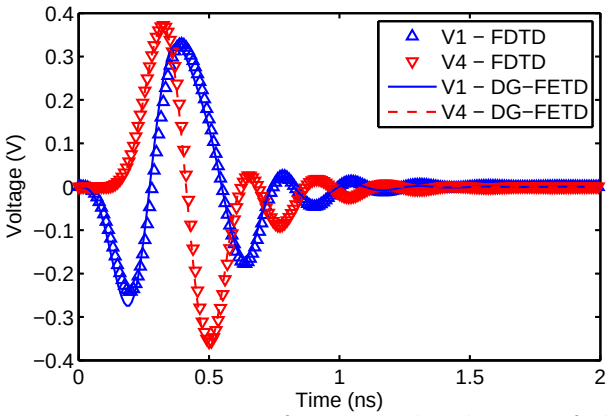

FIGURE 5.8: Transient response of scattered voltages of the multiscale case

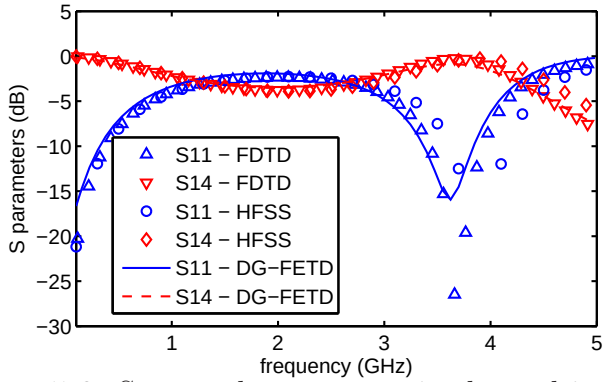

FIGURE 5.9: Scattered parameters in the multiscale case.

5.10, in which the i^{th} layer is scaled one tenth respect to the $(i-1)^{th}$ layer, in this way the scale of the problem is reduced dramatically with the number of layers without changes in either shapes or meshes. The last layer has a subdomain used to evaluate chips with very small structures; in this case, simple conductors with width of 0.15 μm are used. The dimension of the larger layer is 1 cm, the multiscale factor is close to 67 thousand. Finally, eight lumped ports are deployed in each conductor of the bottom layer, with impedance of 50 Ω. The lumped port 1 is selected as active, where a first derivative of BHW pulse is generated with a central frequency of 8.5 GHz.

Transient solution and comparison to FDTD solutions are presented in Figure 5.11, with good agreement. Similarly, Figure 5.12 shows the S-parameters S_{11}, S_{21}, S_{51}, and S_{61}, with very good results. It is obvious that there is good connection betwen ports 1 and 5, and mutual coupling between ports 2 and 6. The results show some disagreements in high frequencies, they could be associated with not enough density of discretization in the FDTD method.

Finally, some computational costs are shown in Table 5.3. The spatial discretization based on DG-FT allows a reduction of number of unknowns in 1/25 times. The CN implicit scheme allows larger timestep respect to the explicit scheme, even with

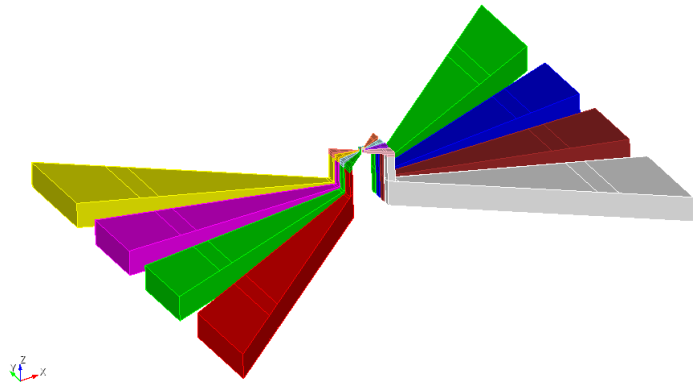

(a)

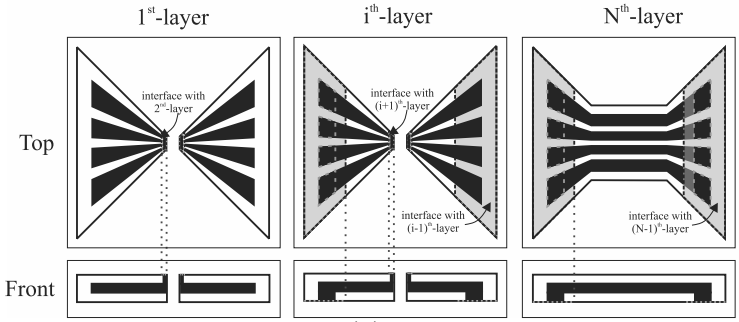

(b)

FIGURE 5.10: General multiscale package-to-chip structure. (a) 3D view, and (b) top view of the 1st, the ith and the Nth layers.

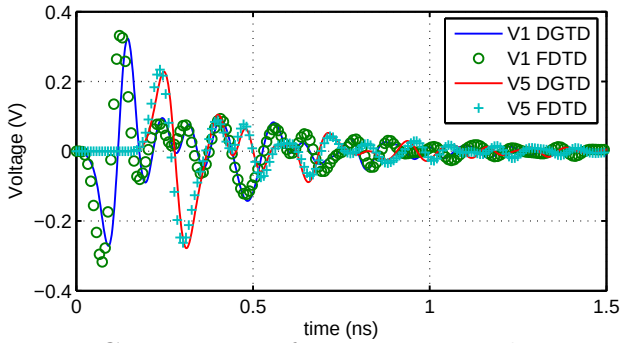

FIGURE 5.11: Comparison of transient signals in ports 1 and 5.

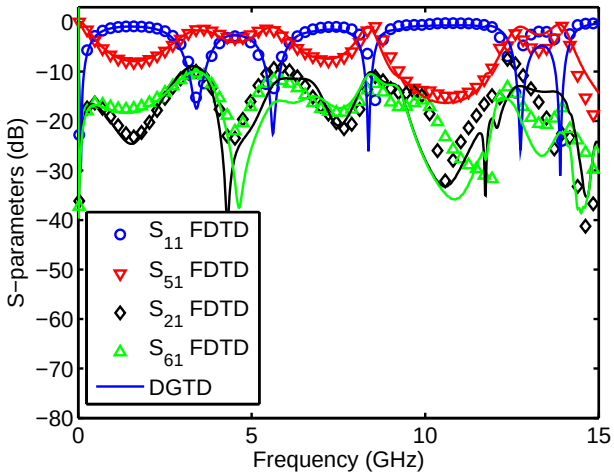

FIGURE 5.12: Comparison of S-parameters.

very fine structures; in this case, there is a difference of almost 6 thousand times between both methods. Finally, an impresive reduction in 110 times of CPU time shows the power of this method.

Table 5.3: Computational costs in highly multiscale problem

	Explicit FDTD	**Implicit DGTD**	**Gain**
Number of unknowns	3.5 millions	138514	25
$\triangle t$	0.36 fs	2 ps	5700
Number of steps for 8 ns	22.8 millions	4000	5700
CPU time per time step (s)	0.0117	0.6	0.02
Total CPU time (s)	265712	2400	110
Memory (MB)	56	1340	0.04

5.2 EB scheme

Three cases are used to verify the behavior of the EB scheme in realistic applications. The first case is a short 50 Ω microstrip line, shown in Figure 5.13(a) which is a typical case used to varify the performance of interfaces in multidomain systems because there are not large reflections if the lumped ports are correctly implemented and matched to the line. Same geometry, but with a substrate splitted into two as shown in Figure 5.13(a), is used to verify the performance of interfaces with different

materials in each side. The second case is a long and narrow transmission line with a thin substrate; this case requires a numerical method with very low numerical dispersion. The third and last case is a complex structure, part of real integrate circuit from Intel, co., that requires a very efficient and accurate method.

5.2.1 Short 50 Ohms microstrip line

The geometry of this case is shown in Figure 5.13(a). The length of this line is 7.5 mm, the width 0.4192 mm, the tickness of the substrate is 0.2 mm. The relative permittivity of the substrate is 3.4. The microstrip line is inside a cavity with dimensions 8.5 mm x 2.0 mm x 0.75 mm filled with air. Also, two 50 Ω ports are used to excite the line with a BHW pulse (with central frequency of 20 GHz), and to extract the scattered voltages. It is important to clarify that two subdomains are used to discretize this system, as illustrated in Figure 5.13(c). The transient results are in Figure 5.14(a), and the absolute error in Figure 5.14(b). We can note a good agreement for all ports and orders of interpolation, with better result for E2B2 case.

Figure 5.13(b) shows the geometry for the microstrip case with two different substrates. The discontinuity is located exactly in the same position as the interface, thus the performance of the method is valiated in this situation. One substrate has $\epsilon_r = 10$, and $\mu_r = 3$; the other one has $\epsilon_r = 2$, and $\mu_r = 15$. Very good agreement with the reference results was obtained in the scattered voltage in the two ports, as we can see in Figure 5.15 which shows the good performance of the interface solver for subdomains with different electric and magnetic properties.

5.2.2 Long microstrip line

The next case is a long (L in Figure 5.16), but also narrow (W in Figure 5.16) microstrip. Long means that L is close to 3 times the wavelength of the highest frequency, and narrow means taht W is 125 times smaller than the same wavelength.

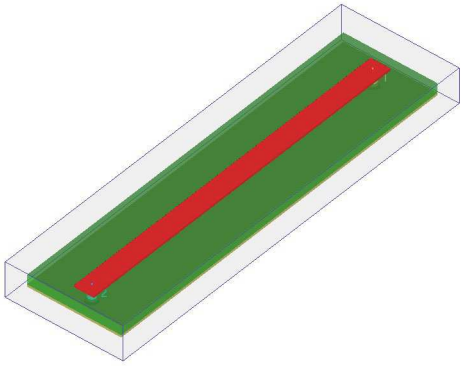

(a)

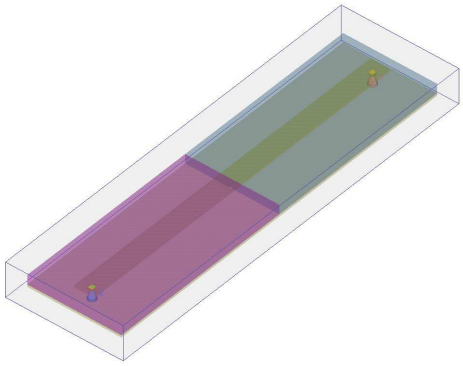

(b)

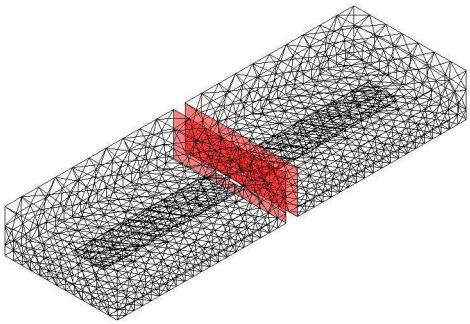

(c)

FIGURE 5.13: Geometry of 50 Ω microstrip lines with: (a) homogeneous substrate, and (b) heterogeneous substrate

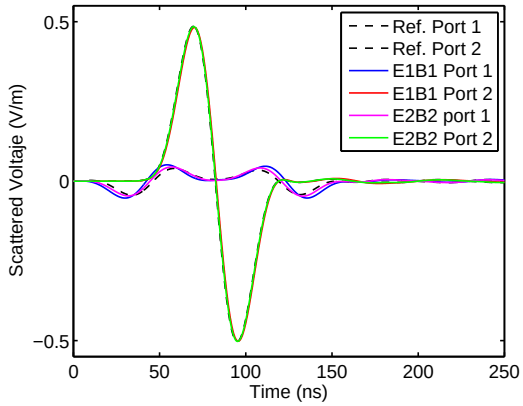

(a)

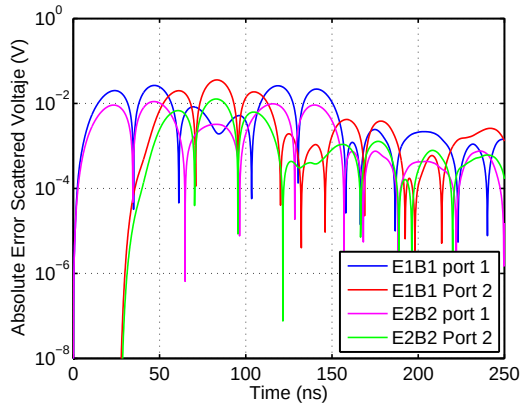

(b)

FIGURE 5.14: (a) Scattered voltage in 50 Ω microstrip line, and (b) absolute error respect to FDTD reference

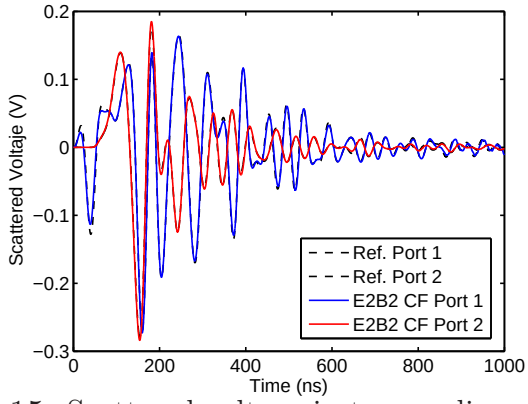

FIGURE 5.15: Scattered voltage in two media microstrip line

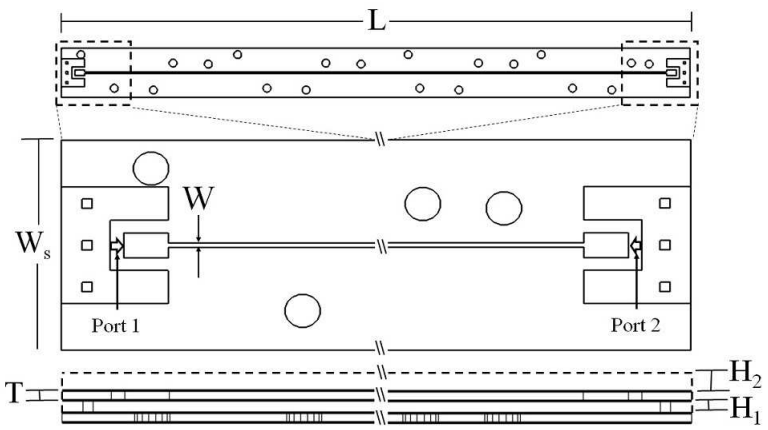

FIGURE 5.16: Geometry of microstrip line case. Some dimensions are L=17 mm, W=0.06 mm, T=0.05 mm

The substrate has a thickness of similar dimension. Then, the multiscale factor in this case is around 500, which is not huge; however, the important point in this case is that requires a numerical method with very low dispersive behavior even with poor quality meshes, i.e. tetrahedrons with bad shape.

In order to capture all the details of the ground while keeping low number of DoF in each subdomain, the structures is divided 10 subdomains as shown in Figure 5.17(a). The FDTD grid in Figure 5.17(b) shows dense parts those are needed to discretize correctly the structure, with a waste of unknowns. The comparison between results of these two methods are shown in Figure 5.18. These results are accurate, with small difference in amplitude. These difference are clear in the scattered parameters in Figure 5.19.

The computational costs are shown in Table 5.4. The required time to solve this case is 10 times smaller for DGTD, mainly because an implicit CN-BT time stepping method is used, then a larger time step can be selected (2000 times larger).

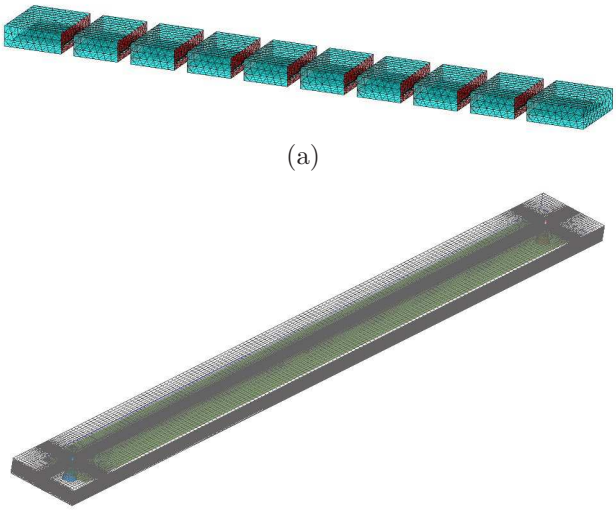

(a)

(b)

FIGURE 5.17: (a) Long microstrip line discretized by 10 subdomains, and (b) the FDTD grid for same case

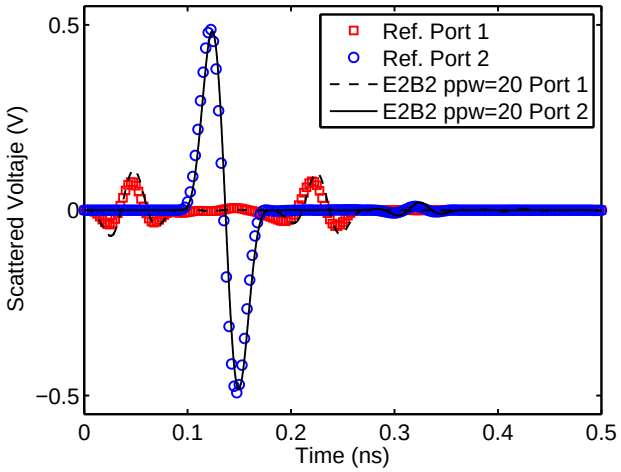

FIGURE 5.18: Scattered voltages in microstrip line case

Table 5.4: Computational costs in long microstrip line case

	FDTD	DGTD	gain
Unknowns	6.9 MDoF	1 MDoF	6.9
Memory	284 MB	1.7 GB	0.17
$\triangle t$	0.5 fs	1 ps	2000
CPU time	10 h 21 m	1 h 2 m	10

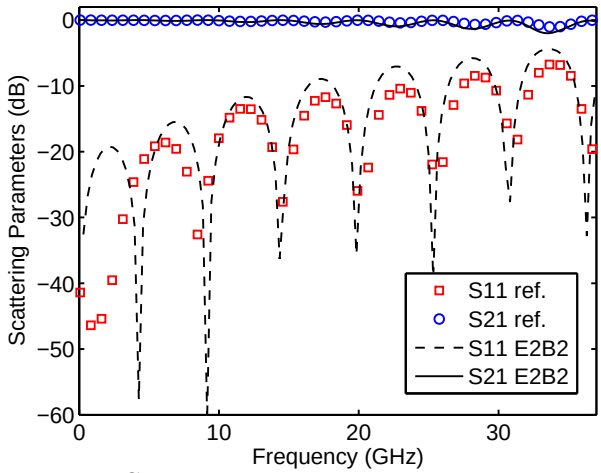

FIGURE 5.19: Scattering parameters in microstrip line case

5.2.3 Integrate circuit

The last case in this work is a 3-dimensional integrate circuit provided by Intel, co. The structure is presented in Figure 5.20, where the locations of the four ports are detailed. This structure is divided into 23 subdomains (Figure 5.21), each one with approximate 70 thousand unknowns, for a total of 1.6 millions DoF. This high number of unknowns required an implicit time integration method with low cost in memory, then a CN-GS method was used. Same case was solved using FDTD method and good agreement in the results were obtained, as we can see the voltages in Figure 5.22 in all four ports and the scattered parameters in Figure 5.23. Table 5.5 illustrate the difference between the performances of these two methods. The number of unknowns is approximate 1 millions larger in FDTD, which is a great advantage of domain decomposition. The reduction in memory cost is 2.5 times. The time step is smaller but not very much, because CN-GS is an iterative method that converges faster with small time steps. Finally, FDTD solver spent more than 10 days solving this case, DGTD just one day.

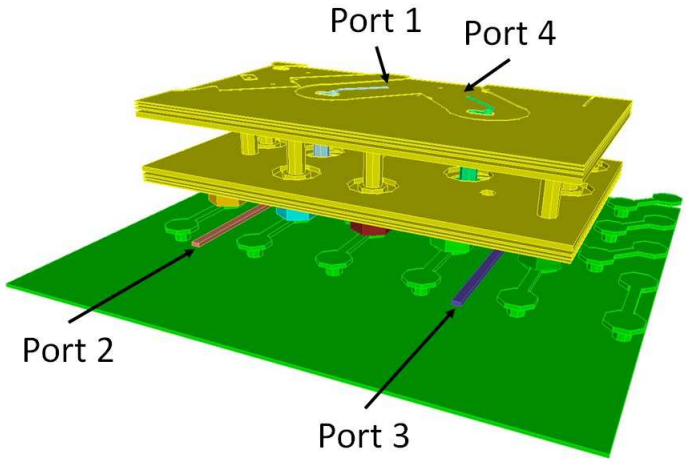

(a)

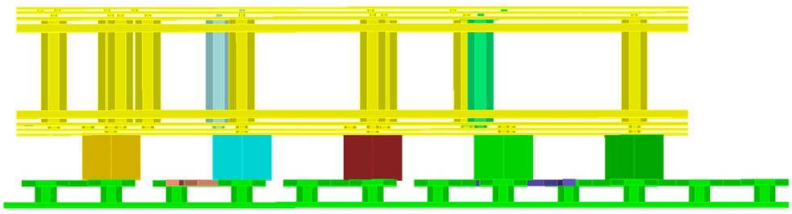

(b)

FIGURE 5.20: Geometry of integrate circuit case (Courtesy of Intel, co.): (a) Ports detail, and (b) Front view

Table 5.5: Computational costs in 3D IC case

	FDTD	DGTD	gain
Unknowns	1.1 TDoF	1.6 MDoF	1e6
Memory	24 GB	9.5 GB	2.5
$\triangle t$	11 fs	25 fs	2.3
CPU time	10 d 13 h 4m	1 d 18 h 8 m	6

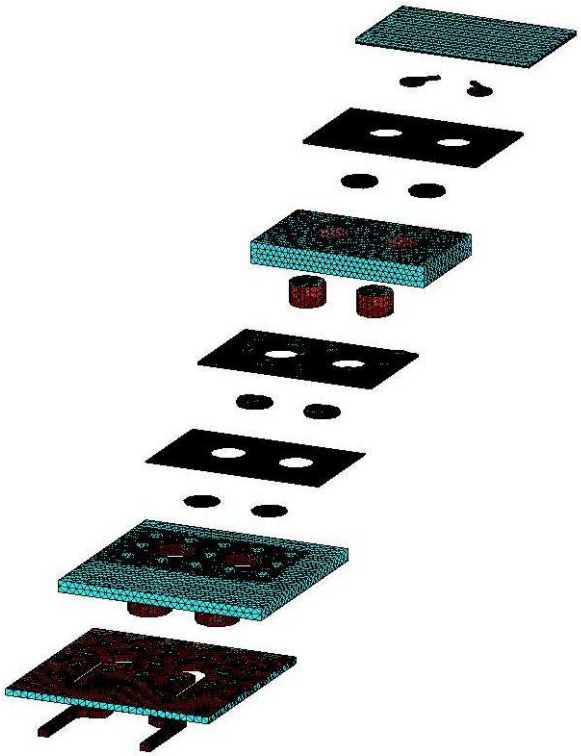

FIGURE 5.21: 3D Integrate circuit discretized into 23 subdomains

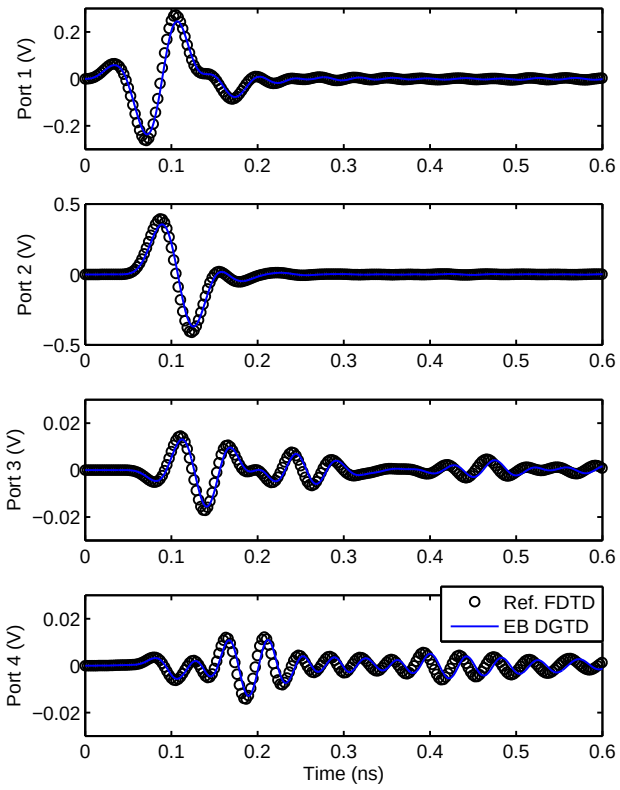

FIGURE 5.22: Scattered voltage in integrate circuit case.

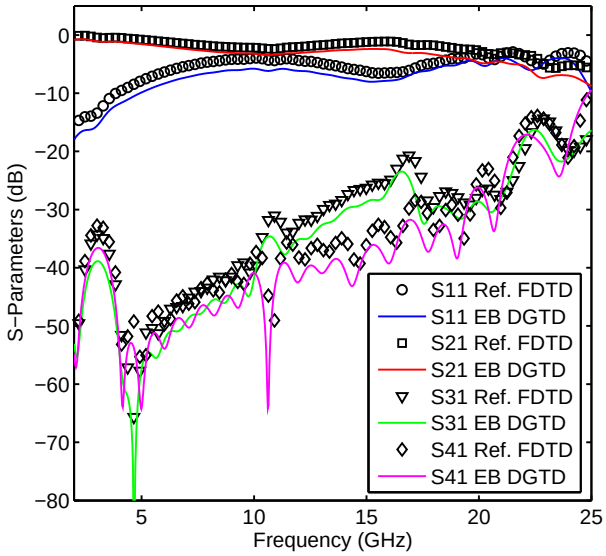

FIGURE 5.23: Scattered parameters in integrate circuit case.

6

Conclusions and future works

6.1 Conclusions

In this work we have reviewed the concepts, the formulations, and the implementation of discontinuous Galerkin time domain method for multiscale electromagnetic simulations. Several different DGTD schemes are discussed in a general DG framework.

From the 1D periodic boundary case and the 3D PEC cavity case, we observed spurious solutions when the same order of interpolation are used in **E** and **H**. These solutions can be noted in eigenvalues and eigenvectors, as the non-physical modes have high values of wavenumber and thus rapid spatial variations. This behavior is presented in the time domain solution as a wave with rapid spatial variations with a high group velocity; however, it is difficult to detect such spurious solutions at a single receiver because of their smooth variations with time. In the three-dimensional case, the spectra obtained using the same-order basis functions show a large number of non-physical peaks from low to high frequencies. All these issues are solved if non-spurious elements, i.e., different order basis functions, are used in **E** and **H**.

To explain and to solve these issues, a unified framework based on the theory of differential forms and the finite element method is used to analyze high-order basis functions employed to discretize the first order Maxwell's equations. Several numerical schemes are analyzed based on: family of basis functions, De Rham sequences, and order of intepolations. Based on this study, field intensities ($\mathbf{E}$ and $\mathbf{H}$) are associated to 1-forms and curl-conforming basis functions; flux densities ($\mathbf{D}$ and $\mathbf{B}$) are associated to 2-forms and divergence-conforming basis functions. Correctness and efficiency are studied using this framework, and numerical dispersion is employed for verification.

From modal analysis based on the Rayleigh quotient is obtained numerical dispersion of several schemes. Additionally, a new method based on dispersive Hodge operators is presented to evaluate normalized numerical phase velocity. From both methods the same fundamental conclusion is obtained: correct discretization of fields belonging to different p-form (e.g., $\mathbf{E}$ and $\mathbf{B}$) uses basis functions with same order of interpolation; however, different order of interpolation must be used if two fields belong to the same p-form (e.g., $\mathbf{E}$ and $\mathbf{H}$).

From eigensolutions and transient response using tetrahedral elements, E2B2 scheme shows the best performance. This scheme has better results in frequency modes and field distribution, i.e. eigenvalues and eigenvectors, than E1H2, E1B1 and Hodge schemes, with errors orders of magnitude smaller. Furthermore. E2B2 is also the most efficient scheme, with less number of unknowns for a defined error. These results are validated in the trasient response.

Spectral-Prism Element implemented in DG-TD shows good performance in number of unknowns, memory and CPU time, in simulation of layers structures with multiple electrical scales, such as inteconnection cases of package structures interacting with on-chip interconnects. The number of unknowns is reduced by domain decomposition method with non-conforming meshes. High order interpolation along

z direction is another method employed to reduce number of unknowns and increase the accuracy of the method.

DGTD works accurately and efficiently for highly multiscale cases, when an appropiated method is implement to solve the time integration. Particularly for multiscale cases. Explicit, implicit and hybrid time integration methods were implemented. The selection of a particular method depends on the electrical scale of the problem and the multiscale factor.

A proposed LDU-DGTD method reduces memory costs and CPU time respect to the block-Thomas method. For this reason, the LDU-DGTD method can solve larger cases than traditional single domain methods and the block-Thomas method. Also, the LDU-DGTD method shows important gains in computational costs respect to explicit FDTD, showing the power of this method.

Finally, this work presented the advances for implementing DGTD for multiscale electromagnetic systems based on E and B fields. From eigensolutions and transient response, E2B2 scheme shows the best performance. This scheme has better results in frequency modes and field distribution, i.e. eigenvalues and eigenvectors, than E1H2, E1B1 and Hodge schemes, with errors orders of magnitude smaller. Furthermore, E2B2 is also the most efficient scheme, with less number of unknowns for a defined error. These results are validated in the trasient response.

6.2 Future Work

Several important aspects have not been covered in detail and are still in active research. These include DGTD methods for:

- Dispersive, anisotropic and nonlinear media
- Hybrid DGTD/SPICE (lumped circuit ports)
- Acceleration via parallel computing, and multilevel parallelization

- Adaptive $h-$ and $p-$ refinement using hierarchical basis functions
- Singular basis functions for describing quasi-static fields around electrically small structures
- Elimination of spurious zero-eigenvalues
- Local timestepping for balanced multiscale cases.
- Improvement of implicit TS iterative solver for non-sequential domain cases

Bibliography

Abboud, N. and Pinsky, P. (1992), "Finite element dispersion analysis for the three-dimensional second-order scalar wave equation," *Int J Numer Meth Eng*, 35, 1183–1218.

Ainsworth, M. (2004a), "Dispersive and dissipative behaviour of high order discontinuous Galerkin finite element methods," *J. Comput. Phys.*, 198, 106–130.

Ainsworth, M. (2004b), "Dispersive properties of high-order Nédélec/edge element approximation of the time-harmonic Maxwells equations," *Philos. Trans. R. Soc. London, Ser. A*, 362, 471–491.

Ainsworth, M. and Wajid, H. (2009), "Dispersive and dissipative behavior of the spectral element method," *Siam J Numer Anal*, 47, 3910–3937.

Bermudez, A. and Pedreira, D. (1992), "Mathematical analysis of a finite element method without spurious solutions for computation of dielectric waveguides," *Numerische Mathematik*, 61, 39–57.

Bernstein, K., Andry, P., Cann, J., Emma, P., Greenberg, D., Haensch, W., Ignatowski, M., Koester, S., Magerlein, J., Puri, R., et al. (2007), "Interconnects in the third dimension: design challenges for 3D ICs," in *Proceedings of the 44th annual Design Automation Conference*, pp. 562–567, ACM.

Buffa, A. and Perugia, I. (2006), "Discontinuous Galerkin approximation of the Maxwell eigenproblem," *SIAM Journal on Numerical Analysis*, 44, 2198–2226.

Butcher, J. C. (2003), *Numerical methods for ordinary differential equations*, vol. 2, Wiley Online Library.

Canouet, N., Fezoui, L., and Piperno, S. (2005), "Discontinuous Galerkin time-domain solution of Maxwell's equations on locally-refined nonconforming Cartesian grids," *COMPEL: The International Journal for Computation and Mathematics in Electrical and Electronic Engineering*, 24, 1381–1401.

Castillo, P., Koning, J., Rieben, R., and White, D. (2004), "A discrete differential forms framework for computational electromagnetism," *Computer Modeling in Engineering and Sciences*, 5, 331–345.

Chen, J. and Liu, Q. (2009), "A non-spurious vector spectral element method for Maxwell's equations," *Progress In Electromagnetics Research*, 96, 205–215.

Chen, J. and Liu, Q. H. (2013), "Discontinuous Galerkin time-domain methods for multiscale electromagnetic simulations: A review," *Invited review paper, Proc. IEEE*, 101, 242–253.

Chen, J., Liu, Q., Chai, M., and Mix, J. (2010), "A nonspurious 3-D vector discontinuous Galerkin finite-element time-domain method," *Microwave and Wireless Components Letters, IEEE*, 20, 1–3.

Chen, J., Tobón, L. E., Chai, M., Mix, J. A., and Liu, Q. H. (2011), "Efficient Implicit-Explicit Time Stepping Scheme With Domain Decomposition for Multiscale Modeling of Layered Structures," *Components, Packaging and Manufacturing Technology, IEEE Transactions on*, pp. 1–1.

Ciarlet, P. (1978), *The finite element method for elliptic problems*, North-Holland.

Cockburn, B., Li, F., and Shu, C. (2004), "Locally divergence-free discontinuous Galerkin methods for the Maxwell equations," *J. Comput. Phys.*, 194, 588–610.

Cohen, G. and Gaunaurd, G. (2002), "Higher-order numerical methods for transient wave equations. Scientific Computation," *Applied Mechanics Reviews*, 55, 85.

Davies, J., Fernandez, F., and Philippou, G. (1982), "Finite element analysis of all modes in cavities with circular symmetry," *IEEE Transactions on Microwave Theory Techniques*, 30, 1975–1980.

De Basabe, J. and Sen, M. (2007), "Grid dispersion and stability criteria of some common finite-element methods for acoustic and elastic wave equations," *Geophysics*, 72, T81–T95.

Ghosh, D., De, A., Taylor, M., Sarkar, T., Wicks, M., and Mokole, E. (2006), "Transmission and reception by ultra-wideband (UWB) antennas," *IEEE Antennas Propagat. Mag.*, 48, 67–99.

He, B. and Teixeira, F. (2006a), "Geometric finite element discretization of Maxwell equations in primal and dual spaces," *Physics Letters A*, 349, 1–14.

He, B. and Teixeira, F. (2006b), "Sparse and explicit FETD via approximate inverse Hodge (mass) matrix," *Microwave and Wireless Components Letters, IEEE*, 16, 348–350.

He, B. and Teixeira, F. (2007), "Differential forms, Galerkin duality, and sparse inverse approximations in finite element solutions of Maxwell equations," *IEEE Transactions on Antennas and Propagation*, 55, 1359–1368.

Hesthaven, J. and Warburton, T. (2007), *Nodal discontinuous Galerkin methods: algorithms, analysis, and applications*, Springer Verlag.

Hiptmair, R. (2001), "Discrete Hodge operators," *Numerische Mathematik*, 90, 265–289.

Ihlenburg, F. and Babuška, I. (2005), "Dispersion analysis and error estimation of Galerkin finite element methods for the Helmholtz equation," *Int J Numer Meth Eng*, 38, 3745–3774.

Jin, J. (2002), "The finite element method in electromagnetics," .

Kotiuga, P. (1989), "Helicity functionals and metric invariance in three dimensions," *Magnetics, IEEE Transactions on*, 25, 2813–2815.

Lee, J. H. and Liu, Q. H. (2007), "A 3-D spectral-element time-domain method for electromagnetic simulation," *IEEE Transactions on Microwave Theory and Techniques*, 55, 983–991.

Lee, J. H., Xiao, T., and Liu, Q. H. (2006), "A 3-D spectral-element method using mixed-order curl conforming vector basis functions for electromagnetic fields," *Microwave Theory and Techniques, IEEE Transactions on*, 54, 437–444.

Lee, J. H., Chen, J., and Liu, Q. H. (2009), "A 3-D discontinuous spectral-element time-domain method for Maxwell's equations," *Antennas and Propagation, IEEE Transactions on*, 57, 2666–2674.

Liu, Q. (1997), "The PSTD algorithm: A time-domain method requiring only two cells per wavelength," *Microwave and Optical Technology Letters*, 15, 158–165.

Liu, Q. H. (1999), "Large-scale simulations of electromagnetic and acoustic measurements using the pseudospectral time-domain (PSTD) algorithm," *IEEE Trans. Geosci. Remote Sensing*, 37, 917–926.

Lu, T., Zhang, P., and Cai, W. (2004), "Discontinuous Galerkin methods for dispersive and lossy Maxwell's equations and PML boundary conditions," *Journal of Computational Physics*, 200, 549–580.

Melvin, T., Staniforth, A., and Thuburn, J. (2012), "Dispersion analysis of the spectral element method," *Q J Roy Meteor Soc*.

Mohammadian, A., Shankar, V., and Hall, W. (1991), "Computation of electromagnetic scattering and radiation using a time-domain finite-volume discretization procedure," *Computer Physics Communications*, 68, 175–196.

Monk, P. (2003), *Finite element methods for Maxwell's equations*, Oxford University Press, USA.

Peterson, A., Ray, L., Mittra, R., Volakis, J., Chatterjee, A., and Kempel, L. (1998), *Computational methods for electromagnetics*, vol. 40.

Ramm, P., Klumpp, A., Weber, J., Lietaer, N., Taklo, M., De Raedt, W., Fritzsch, T., and Couderc, P. (2010), "3D Integration technology: Status and application development," in *ESSCIRC, 2010 Proceedings of the*, pp. 9–16, IEEE.

Schuhmann, R. and Weiland, T. (1998), "Stability of the FDTD algorithm on nonorthogonal grids related to the spatial interpolation scheme," *Magnetics, IEEE Transactions on*, 34, 2751–2754.

Seriani, G. and Oliveira, S. (2008), "Dispersion analysis of spectral element methods for elastic wave propagation," *Wave Motion*, 45, 729 – 744.

Solín, P., Segeth, K., and Dolezel, I. (2004), "Higher-order finite element methods," .

Sperling, E. (2013), "Accelerating Moores Law," .

Stanescu, D., Kopriva, D., and Hussaini, M. (2000), "Dispersion analysis for discontinuous spectral element methods," *J Sci Comput*, 15, 149–171.

Stevenson, R. (2013), "Changing the Transistor Channel," .

Sung, R., Chiang, K., Lee, D., and Ma, M. (2011), "High-speed electrical design study for 3D-IC packaging technology," in *Microsystems, Packaging, Assembly and Circuits Technology Conference (IMPACT), 2011 6th International*, pp. 144–146, IEEE.

Taflove, A. and Brodwin, M. E. (1975), "Numerical solution of steady-state electromagnetic scattering problems using the time-dependent Maxwell's equations," *Microwave Theory and Techniques, IEEE Transactions on*, 23, 623–630.

Tarhasaari, T., Kettunen, L., and Bossavit, A. (1999), "Some realizations of a discrete Hodge operator: A reinterpretation of finite element techniques [for EM field analysis]," *Magnetics, IEEE Transactions on*, 35, 1494–1497.

Teixeira, F. and Chew, W. (1999), "Lattice electromagnetic theory from a topological viewpoint," *Journal of mathematical physics*, 40, 169–187.

Tobón, L., Chen, J., and Liu, Q. (2011), "Spurious solutions in mixed finite element method for Maxwell's equations: Dispersion analysis and new basis functions," *Journal of Computational Physics*, 230, 7300–7310.

Tobon, L. E., Chen, J., and Liu, Q. H. (2011), "Multilayer microwave filter design using a locally implicit discontinuous Galerkin finite-element time-domain (DG-FETD) method," in *Antennas and Propagation (APSURSI), 2011 IEEE International Symposium on*, pp. 2972–2975, IEEE.

Tonti, E. (2002), "Finite formulation of electromagnetic field," *Magnetics, IEEE Transactions on*, 38, 333–336.

Tu, K. (2011), "Reliability challenges in 3D IC packaging technology," *Microelectronics Reliability*, 51, 517–523.

Walters, R. A. and Carey, G. F. (1983), "Analysis of spurious oscillation modes for the shallow water and Navier-Stokes equations," *Computers & Fluids*, 11, 51–68.

Wang, S. and Teixeira, F. (2003), "Dispersion-relation-preserving FDTD algorithms for large-scale three-dimensional problems," *IEEE Trans. Antennas Propagat.*, 51, 1818–1828.

Wedge, S., Wasserman, E., and Neilson, D. (2005), "Transient simulations at RF frequencies," *Microwave J.*, 48, 116–128.

White, D., Koning, J., and Rieben, R. (2006), "Development and application of compatible discretizations of Maxwell's equations," *Compatible Spatial Discretizations*, pp. 209–234.

Winkler, J., Davies, B., et al. (1984), "Elimination of spurious modes in finite element analysis," *Journal of Computational Physics*, 56, 1–14.

Xiao, T. and Liu, Q. H. (2005), "Three-dimensional unstructured-grid discontinuous Galerkin method for Maxwell's equations with well-posed perfectly matched layer," *Microwave and optical technology letters*, 46, 459–463.

Biography

Luis Eduardo Tobón was born in Armenia, a wonderful city surrounded by coffee crops in the heart of Colombia, South America. He received the B.S. degree in electronic engineering and the M.Sc. degree in materials science from the Universidad del Quindio, Colombia, in 2003 and 2007, respectively. In 2013, He received the PhD degree in Electrical and Computer Engineering from Duke University, NC, US.

Luis Eduardo was recognized in 2008 with with a Fulbright-Colciencias Scholarship. In 2010, he was acknowledged as an emeritus graduate, by the school of engineering, Universidad del Quindo. He also received in 2011 the Best Paper Award from the IEEE Transactions on Components, Packaging and Manufacturing Technology, Electrical Performance of Integrated Systems Category.

From his research, Dr. Tobón has participated in different conferences, and published several papers in the topics of computational electromagnetics and microwave devices. Some selected papers are:

Chen, J; Tobón, L.E.; Chai, M; Mix, J.A.; Liu, Q. H. Efficient ImplicitExplicit Time Stepping Scheme With Domain Decomposition for Multiscale Modeling of Layered Structures IEEE Transactions on Components, Packaging and Manufacturing Technology. Vol. 1 No. 9, pp 1438 1446. Sept. 2011. Best paper award.

Tobón, L.E.; Jiefu Chen; Liu, Q.H.; Multilayer microwave filter design using a locally implicit discontinuous Galerkin finite-element time-domain (DG-FETD) method IEEE International Symposium on Antennas and Propagation (APSURSI),

2011. 3-8 July 2011, pp. 2972 2975

Tobón, L.; Chen, J.; Liu, Q. H. Spurious solutions in mixed finite element method for Maxwell's equations: Dispersion analysis and new basis functions Journal of Computational Physics, Volume 230, Issue 19, p. 7300-7310. 2011.

Since 2007, Luis Eduardo has been working as a Research Assistant Professor with the Department of Computer Science and Engineering, Pontificia Universidad Javeriana-Cali, Colombia. His current research interests include computational electromagnetics applied to multiscale problems, geophysical subsurface sensing, electronics packaging, microwaves and electronic devices, and wireless communication and propagation.